UNIVERSITÀ DI PARMA

UNIVERSITA' DEGLI STUDI DI PARMA

DOTTORATO DI RICERCA IN

"SCIENZA E TECNOLOGIA DEI MATERIALI"

CICLO XXXIII

$CsPbBr_3$ FOR SOLAR FUELS PRODUCTION

Coordinatore:

Chiar.mo Prof. Enrico Dalcanale

Tutore:

Dott.ssa Alessandra Sanson

Dottoranda: Linda Bergamini

Anni Accademici 2017/2018 – 2019/2020

"Success consists of going from failure to failure without loss of enthusiasm"

Winston Churchill

Summary

Aim of the thesis

Fossil fuels depletion and climate changes induced by their use, are of major concern in the modern society. The production of solar fuels and chemicals using renewable energy (in particular solar energy) to reduce CO_2, represents an important option to decrease the greenhouse gases emissions producing at the same time valuable chemicals.

The work was focused on the synthesis and characterization of $CsPbBr_3$, a compound belonging to the class of all-inorganic halide perovskites (ABX_3, A=monovalent cation, B=bivalent cation and X=halogen), considered as photoelectrode in a photoelectrochemical cell (PEC) for the production of solar fuels and chemicals reducing CO_2. The activities were focused on achieving a single phase system considering different synthetic routes (co-precipitation, oleate and MW-assisted) to assess the influence of the method on its final properties. The powders were firstly deeply analysed structurally and morphologically and then on the electrochemical point of view to establish their potential application in a PEC. For this purpose, the material needs in fact to show particular properties such as the ability to harvest the light in the visible range of the electromagnetic spectra, a high charge mobility and good charge transfer. The most promising $CsPbBr_3$ produced were then deposited on a conductive substrate in order to build a photoelectrode. Thin films were deposited using techniques able to tune the film properties leading to homogeneous films without defects that could interact with the charge mobility and charge transfer. Drop by drop method was considered for the first trials, while spin coating and ink-jet printing for the subsequent part of the work. Different inks were produced to be used with the different techniques and the most suitable combination of process parameters was set. Another important aspect that was tackle in the thesis was the instability of the $CsPbBr_3$ in water. Even if the CO_2 reduction can be obtained also in organic environment, the aqueous media is preferable for the lower cost, higher safety and above all, lower environmental impact. $CsPbBr_3$ is however poorly stable in water. To improve this property different approaches were considered in the thesis: i) protect the powder with organic moieties; ii) produce hybrid systems with graphene oxide or black phosphorous iii) protect the film after deposition with graphite or platinum. The last two options were found to be suitable to protect the powder assuring at the same time good photoelectrochemical properties. The film after

a thorough characterization (either microstructural and electrochemical) were used to build a complete photoelectrochemical cell. The $CsPbBr_3$-based photoelectrode was used as working electrode at the cathodic side, with Pt as counter electrode and Ag/AgCl electrode as reference electrode. The cell was operated in different conditions of time and voltage applied under the irradiation of a solar simulator to identify the best reaction parameters. The reaction products were analysed by chromatography (either liquid and gas) to assess the photoreduction capability of the systems.

The results indicated that $CsPbBr_3$ is able to effectively reduce CO_2 dissolved in water leading to the formation of oxalic acid and hydrogen.

Chapter 1

Introduction

1.1. Energetic crisis

The energy crisis arisen in the last half century, is connected to the limited natural resources used to power the actual industrial society, and their limited availability that became clearer as the demand steadily increase with time. The electricity consumed just in the last year was equal to 22536 TWh[1,2].

The International Energy Agency (IEA), estimates the continue increase of the energy demand in the future, if the energy policy continue to be the current one[3]. Nowadays fossil fuels supply almost the 85 % of the energy, with the consequent emission of pollutants in the atmosphere. The concentration of the CO_2 was 278 ppm at the start of the industrial revolution, while today, with the fossil fuels drivers of the industrialized world, is 410 ppm[4]. Other greenhouse gases (GHGs) such as CH_4, N_2O or CFC appeared with significant concentration in the atmosphere as a consequence of the industrial revolution. While burning fossil fuels lead to the formation of other toxic species such as SO_x, NO_x, particulate matter or heavy metals.

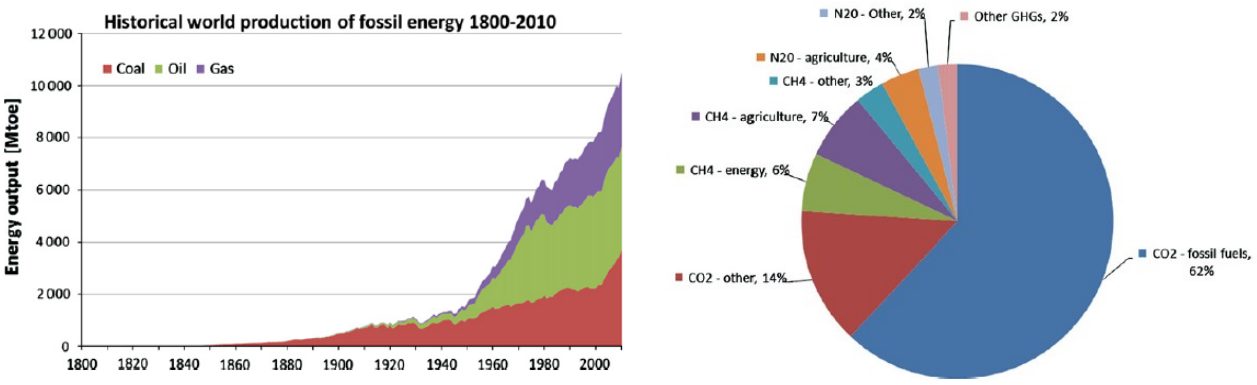

Fig 1.1: Production of fossil fuels from 1800 to 2000 and GHGs species release in atmosphere[5].

The CO_2 and GHGs concentration in the atmosphere had a steeply increase in the 1950's when the technological development of the post war began. In the successive period, for the first time, the global warming problem was connected with the anthropogenic emission of GHGs. As a consequence, the governments decided to institute a new organization which, from that time on, would have managed all the information about the climate change. This organization, called Intergovernmental Panel on Climate

Change (IPCC), since 1988 provides regular assessments of the scientific basis of climate change, its impacts and future risks, and options for adaptation and mitigation. The reports contain assumption and prediction for fossil fuels production and consumption, and climate models are developed transforming the projected emission into climate change. However, the scenario changes continuously during the years, as it considers several variables such as the economic development, therefore the models have to be reviewed constantly.

The major part of the CO_2 comes from the use of fossil energy that other than the impact on the global warming, will not be able to satisfy the high demand due to the continuous growth of economies. The fossil fuels formation requires millions of years while their extraction and use are actually very rapid, therefore they are limited and finite. In addition, the industrialization of Asian emerging economies signed the beginning of an increasing in the prices of the trend for fossil fuels. In particular between 2000 and 2008 there was an exponential growth of the price as reported in Fig 1.2.

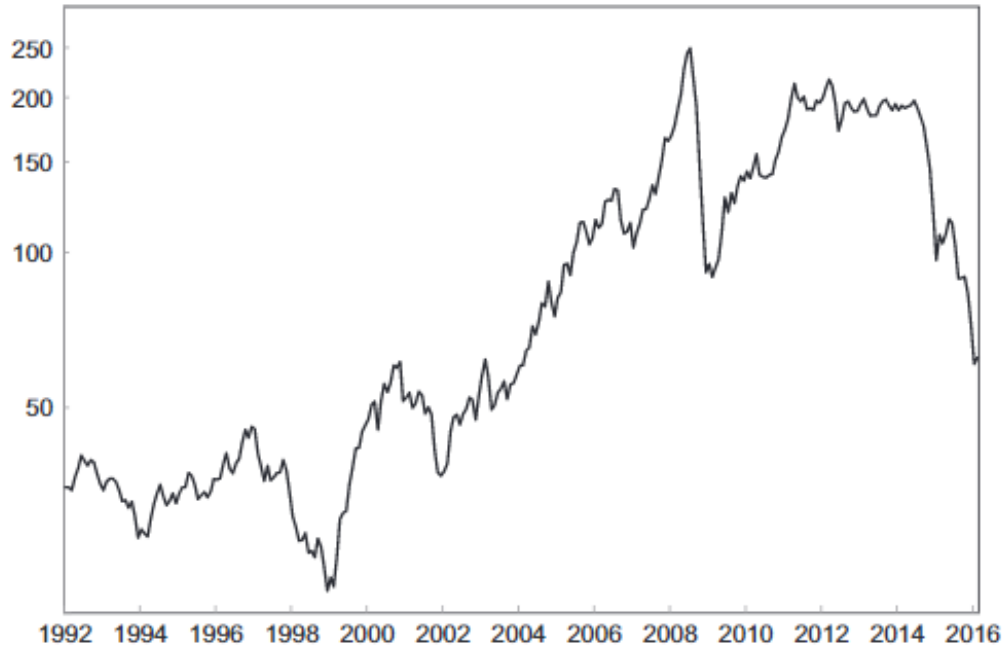

Fig 1.2: Trend of fossil fuels prices from 1992 to 2016.

In 2008 the price collapsed due to the financial crisis, for growing again from 2009 to 2014. After this date, the decrease of the oil and coal price was due to the increase in the exportation and the decrease of the demand[6]. Nowadays the consensus about the

reduction of fossil fuels for limiting the global temperature rise under the 2 °C assessed during the Paris agreement and ratified afterwards are affecting the price and the main producers and exporters of oil and fossil fuels. The rollercoaster of the price has affected until now the penetration of the renewables, that are nonetheless the only possible option to mitigate the climate changes.

The damages induced by the use of fossil fuels on the environmental are several starting from the impact on the oceanic thermodynamic with the fresh water sources depleting at significant rate to natural disaster and weather events such as drying of the lands and forests, flooding or hurricanes just to name few of them. Passing from fossil fuels generation and consumption to greener options is the general solution to the major part of the aforementioned issues. However, there are some critical aspects about the replacement of the fossil sources with renewable ones: first of all, the changes need to face political and economical and the choice of the renewable energy should be strictly connected to the region considered.

1.2. Renewable energies

Renewable sources are considered the ones clean, with low environmental impact, which produced small secondary wastes and that are replenished as the same rate as they are consumed. The renewable energies are: biomass, geothermal, pumped hydro, solar and wind energies[7]. The use of green energy that allows also to balance the use of fossil fuels saving them for other uses (such as production of materials and chemicals) reducing at the same time the pollution and the greenhouse gases emissions. The investment in renewable energies, moreover, could improve the quality of life creating new employments and reducing problems of water supply and local energy. The disadvantage of main renewable energies such as the solar energy or the wind is their intermittence, the energy produced in fact is not continuous, and it is necessary a storage system in order to guarantee the energy for all the time.

1.2.1. Biomass

Biomass energy is obtained converting organic materials such as agriculture and forestry residues or solid wastes into heat, fuels and electricity. It is necessary to differentiate between the traditional and modern use of biomass. Traditionally, biomasses have been used for cooking and heating: the sustainability was not taken into account, on the contrary it brings to GHGs emissions and to an inappropriate use of the soil. In the modern concept of biomass, the energy is used to produce electricity, steam and biofuels. Many routes exist to exploit biomass for these purpose, the biomass is widely used in the Nordic countries, to produce heat with automated systems, and exists a catalytic process for the gas cleaning that assure high efficiency (70 %) and limited emission in the atmosphere. The production of electricity is achieved through combustion, gasification or digestion of the biomass.

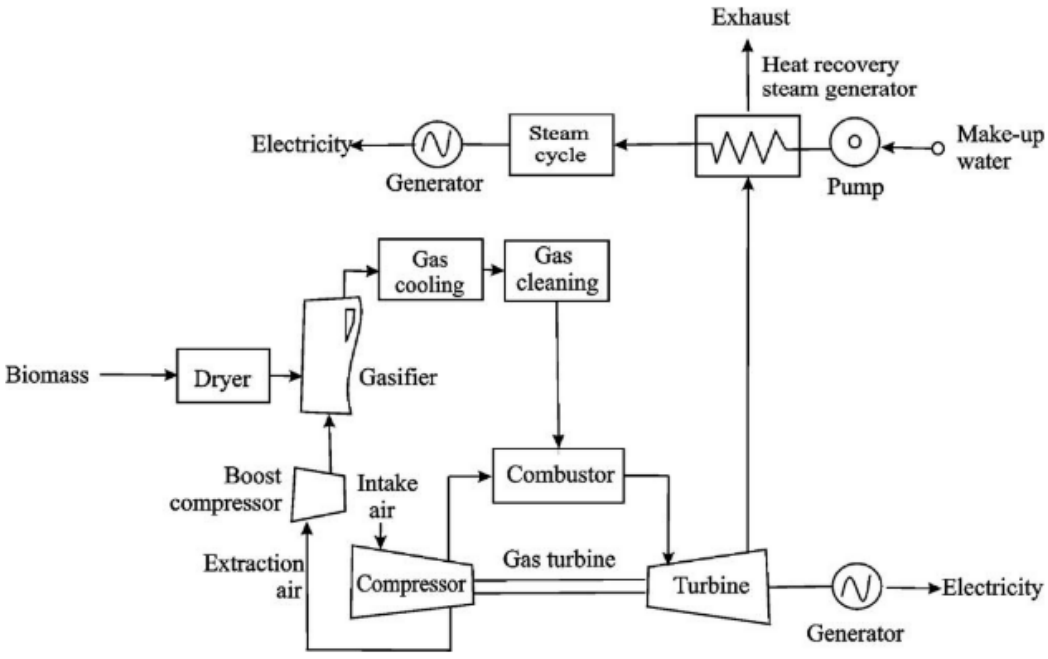

Fig 1.3: Gasification plants of a biomass.

The combustion is often in combination with the natural gas and coal to replace part of primary fossil fuel while in the gasification the biomass is transformed into fuels which are used in a gas turbine after a cleaning process. Finally the anaerobic digestion of

biomass produces the biogas which contains mainly CH_4 (40-70 %) and CO_2 that can be directly used in domestic applications or transported using the common gas grid[8].

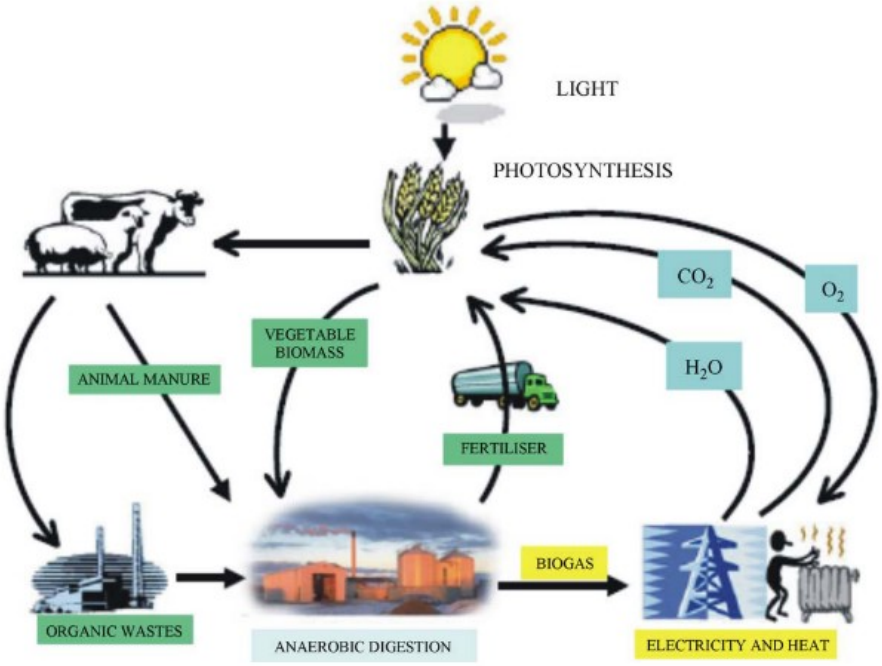

Fig 1.4: Process for the biogas production by an anaerobic digestor.

The biomass can lead also to liquid bio-oils that can be easily converted into biodiesel. Although the use of biomass can be considered a carbon-neutral process, it poses some issues in terms of use of soils and water and impact on the landscape.

1.2.2. Wind energy

With this technology, the electricity is produced by wind turbines which convert the motion of the wind into rotational energy. The energy generated is channelled into power generators (Fig 1.5) to produce the electricity that enters the grid becoming available to the consumers.

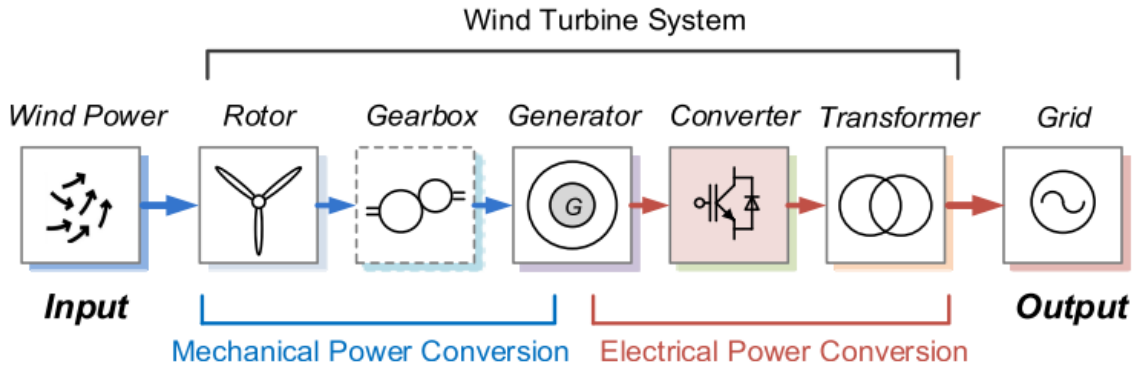

Fig 1.5: Power conversion steps in a wind turbine system[9].

In Fig 1.5 the different components of a generic wind turbine system are shown. In summary the system is composed by the mechanical part (turbine rotor and gearbox) and the electrical one. The turbine design is related to the generator and could have different configuration depending on the speed control system and the aerodynamics[9]. The last years development have seen an increase of the wind turbine dimensions and of the power rating, and the development of different type of wind turbine systems confirming the three-blade structure as the best configuration[10,11,12].

One of the main issue is related to the bird mortality due to the wind turbine: birds are attracted by the lights of the wind farms increasing the probability of their impact with the blades[13]. Other important negative effects of this technology are the noise pollution and the visual impact. The wind farms or even only one wind turbine are commonly placed far from residential areas for the noise (either aerodynamic and mechanical) derived from the turbines motion[14]. The visual impact is evaluated through the distance from home and the degree of influence, taking into consideration the colour contrast with the landscape or the flashing shadows[15]. In addition, some ecological influences are reported such as the disco effect or shadow flickers: these phenomena are caused by the blade motion and by the reflection of the sunlight on the blades that could disturb the residential area near the turbines. The installation of the turbine finally can be responsible for soil erosion and deforestations with significant impact on the ecological aspect that requires specific attention.

1.2.3. Geothermal energy

Geothermal energy comes from the heat present in the sub-surface of the earth. Thanks to the high temperature of our planet, the IR radiations are available at the earth surface as hot springs or volcanoes. Other sources such as magma and melted rocks, requires drilling, which are expensive, and they could cause the emission of small amounts of methane or carbon dioxide presents under the crust. The geothermal plant works as a steam engine: the water is heated up to the vapour formation that is then used in a gas turbine: the expansion of the gas inside the latter induces its mechanical movement that is then converted into electricity[16]. The first geothermal plant was installed in Italy in 1904 at Lardarello, and the energy produced used for therapeutic bath, water heating and for agriculture. In these cases, the hydrothermal fluids are directly used as heat source and pumped through a heat exchanger heating air and/or liquid. Different configurations of geothermal plants are available: the older ones are the dry steam and flashed steam systems, the newer one are based on the binary cycle[17]. The dry steam system exploits the steam which is cleaned from the solid part and is injected directly in the turbines; the flashed steam systems use the high temperature fluids present under the earth crust and through the flash transform the liquids in steam. The binary cycle systems finally are divided in two types: the ones that use the low enthalpy resources and another that processed the moderated enthalpy resources. Most of the system are now using a binary working fluid (generally, but not only, water) which is vapoured with the heat coming from the geothermal source and is then superheated expanding itself in the turbine[18]. The geothermal energy, even if an interesting renewable source is not ubiquitous and it is affected by some technical and environmental issues.

1.2.4. Solar energy

The sun is an inexhaustible source of free energy having the potential to fulfil the energy demand of the planet, the solar energy in form of light and other radiation types was estimated to be $384.6*10^{24}$ Watts. However, the solar energy is still not enough to supply the request as we are not yet able to exploit its full potential even if it would be

the best option to reduce the carbon emission in the atmosphere, as it is ubiquitous and therefore in principle usable, even if with different potentials, all over the world[19].

The solar energy availability depends on various factors all related to the geographic area of interest (latitude, diurnal variation, climate)[20].

Solar energies technologies present opportunities and limitations, on one hand their use potentially allows the energy independence for all, and it is fundamental for the enhancement of the socio-economic conditions especially of the developing countries, on the other hand there is still some technological issues to overcome. The efficiency in single p-n junction is theoretically limited to around 33% (Shokley-Quaser limit) while the installation of photovoltaic system undergoes limitations due to environmental or architectonic issues. The main limitations of the solar energy technologies are related to the high initial cost of the plants, the low efficiencies of the solar panels in domestic use (≈ 20%), higher efficiency solar panels are available but at higher prices. One important limitation of the solar energy (as well as of the wind one) is its intermittency. The energy produced during the day (especially in the high irradiation periods) is commonly exceeding the demand and therefore should be stored in order to become available when needed (e.g. during the night). In order to do so, electrochemical storage devices like batteries are generally considered. These are heavy and large, and commonly include precious metals and rare materials that are difficult to recycle and expensive.

The positive aspects are nevertheless significant: solar energy is in fact, considered one of the major players in the transition towards a renewable energy system. Its adoption can deeply reduce the impact on global warming limiting the greenhouse gases emissions. Furthermore, the technologies based on solar power are labour-intensive, and as a consequence, can create new jobs opportunities.

The solar energy technologies could be divided in passive and active ones. The first ones, are related to the technologies which accumulate and use thermal energy and light without transform it in others energies forms; on the other hand, the active solar energies are the ones which harvest solar radiations and convert them in electricity or heat. Photovoltaics and thermal technologies are the most known. Thermal energy[8] coming from the sun, could be used for direct and indirect applications. For example, the direct heating is interesting in solar cooking[21] that avoid the use of firewood; in water heating of domestic size, where it is able to satisfy the needs of a medium family[22], or in

solar drying systems[23] used to dry fruits and vegetables in clean and hygienic way. These solutions reduce the CO_2 emission in atmosphere replacing other technologies based on fossil fuels. The indirect use of the solar thermal power consists in its conversion in electricity[24]. This conversion through solar collectors is generally used in remote areas where the electricity is not available. Solar thermal energy is applicable also to the industrial field and not only for domestic purpose. The heating of industrial plants requires however the use of solar concentrators, where high-magnification mirrors are used to collect the solar radiation, that is then transformed in heat[25].

The electricity generation is achieved through the solar energy thanks to the photovoltaic (PV) system. The PV cells are based on a semiconductor material and on the PV effect: photons with energy equal or higher than the band gap value of the semiconductor, excite the electrons from its valance to the conduction band. The energy absorbed from the electrons is given by the equation:

$$E = h\upsilon = \frac{hc}{\lambda} \qquad (1.1)$$

where E is the photons energy, ν is the frequency related to the photons and λ the respective wavelength, h is the Planck's constant and c is the speed of light.

Silicon is the main material used as semiconductor in photovoltaic cell for its peculiar electronic characteristics that perfectly match the solar spectrum even if the non-direct semiconductive behaviour limits the absorption leading to thick cells. Moreover, the thermal losses from the high energy photons and the losses related to the photons not absorbed, are the main causes of the not so high Power Conversion Efficiency (PCE). The use of multi-junction solar cells represents a solution to improve the PCE to value up to ≈ 45%. Multi-junction or tandem solar cells consist in the electrical connection of different materials (CdTe or CIGS) with different band-gap limiting the thermal and transmission losses. Other interesting configurations of solar cells are the organic-inorganic solar cells and the solid state organic solar cells. The solid state organic solar cells use completely organic molecules or polymers for both the donor and acceptor, and in the last years have attracted renewed interest for their improvement in the PCE. In the organic-inorganic configuration on the other hand, an organic dye is coupled with an inorganic

semiconductor such as TiO_2, ZnO or ZrO_2, and in the presence of a redox electrolyte. A recent evolution of these system are the so-called perovskites (lead halide perovskites) that with high charge mobility and good absorption of visible light have now reached the conversion efficiency of the most mature silicon technology even if with some stability issues yet to be solved.

The solar energy could also be used as vehicle to produce chemical bonds through chemical reactions[26]. This application is particularly interesting for producing solar fuels from carbon-based waste such as CO_2 and water, providing, at the same time, a way of storing solar energy in form of chemical bonds. One of the most interesting energy vectors that can be produced in this way is hydrogen, from the splitting of water mediated by the solar energy. This is considered the major candidate able to replace fossil fuels for a green energy system. Carbon dioxide can be considered to convert the solar energy in C-based products transforming in this way the major responsible of the greenhouse effect in an important and useful raw material. The direct production of solar fuels (oxidation of water and the contemporary reduction of CO_2) needs the intervention of a catalytic materials. The materials chosen should be cheap, safe and earth abundant, to have the chance to scale up the device and achieve the significant replacement of fossil fuels; in addition they should be able to harvest light and photogenerate electron-hole couple in order to complete efficiently the redox process at the basis of the conversion mechanism.

1.3. CO_2 as raw material for solar fuels and chemicals reduction

In an ideal scenario, the amount of carbon dioxide present on the earth should be used and consumed to keep the balance in the environment. The intense use of fossil fuels caused the increase in the emission of greenhouse gases such as CO_2[27] responsible for temperature increase and the actual climate change issue.

Carbon dioxide can however represent a useful raw material if its reduction is coupled with the water oxidation semi-reaction:

$$2H_2O \rightarrow O_2 + 4H^+ + 4e^-$$

that generates the protons and the electrons necessary.

The reduction of carbon dioxide is complicated as a consequence of the great stability of the C=O bond and for the high oxidation state (+4) of the carbon atom. The use of an external bias and a catalyst are therefore necessary to carried out the reaction. The last one is particularly important as it increases the reaction rate as well as it drives the selectivity towards the final products of the reaction. In order to drive the reaction towards the desired products, it is important to understand the mechanisms involved in the CO_2 reduction. The catalytic process consists fundamentally in three steps: the adsorption of CO_2 on the catalyst surface, the electrons/protons transfer and the reaction on the catalytic surface. In literature[28,29] many researchers claim the formation of $CO_2^{\circ-}$ as intermediate derived from the CO_2 adsorbed on the catalyst surface, but the transformation is strenuous and highly energetic and the thermodynamic potential request for the transformation is -1.90 V vs NHE at pH = 0. The selectivity towards the formation of CO, hydrocarbons (CH_4; C_2H_4; C_2H_6), alcohols (CH_3OH or CH_3CH_2OH) or acids ($HCOOH/HCOO^-$) depends on the nature of the catalyst, however in the real scenario is usual to find a mixture of the products at the end of the reaction because of the unfavorable thermodynamic of the mechanism. The formation of the intermediate $CO_2^{\cdot -}$ and the charge transfer needed for the molecule reduction require high potentials that are often given by an external load. This could come from different sources: the reduction of the carbon dioxide could be performed for example by electrocatalysis or photocatalysis where the electricity comes from the sun.

In general, the CO_2 reduction is performed in presence of water: in these conditions the CO_2 conversion is in competition with the Hydrogen Evolution Reaction (HER). In the three steps mechanism abovementioned, the two competitive reactions share the first two steps but non the last one: the surface reaction. The HER is favorite in acidic condition for the presence of protons, while the CO_2 reduction occur easily in a basic environment for its spontaneous transformation in bicarbonate and carbonate species (HCO_3^- and CO_3^-) in such conditions. The thermodynamic potentials of the different transformations of the CO_2 and of the HER are listed in Table 1.1.

Table 1.1 Thermodynamic potentials of main CO_2 conversion reaction

Reaction	*E^0(V vs NHE, pH 7)*
$2H_2O + 2e^- \rightarrow 2OH^- + H_2$	-0.41

$CO_2 + 8H^+ + 8e^- \rightarrow CH_4 + 2H_2O$	-0.24
$CO_2 + 2H^+ + 2e^- \rightarrow CO + H_2O$	-0.51
$CO_2 + 6H^+ + 6e^- \rightarrow CH_3OH + H_2O$	-0.39
$CO_2 + 2H^+ + 2e^- \rightarrow HCOOH$	-0.58
$2CO_2 + 14H^+ + 14e^- \rightarrow C_2H_6 + 4H_2O$	-0.27
$2CO_2 + 12H^+ + 12e^- \rightarrow C_2H_5OH + 3H_2O$	-0.33
$2CO_2 + 2H^+ + 2e^- \rightarrow H_2C_2O_4$	-0.87

The nature of the final products is also influenced by the way in which the CO_2 molecule is coordinated to the catalyst surface: by oxygens, by carbon or *via* both atoms. The choice depends on the acidity of the active centers. If the catalyst presents Lewis acid centers on its surface, CO_2 prefers the oxygen coordination donating electrons. On the contrary, the CO_2 could gain electrons from the Lewis basic centers of the catalyst (e.g. oxides); finally both oxygen and carbon atoms could interact with the catalyst surface behaving as electron donor and acceptor at the same moment (mixed coordination)[30]. The increase of the surface catalyst defects, basic centers or of the surface area, are only some of the strategies adopted for enhancing the absorption of CO_2 molecule on the catalyst surface. Other important factors for the pathway and mechanism of the reduction reaction are pH, the presence of hydrophobic or hydrophilic groups on the catalyst surface, the presence of a co-catalyst or the action of an external bias.

The solubility of the carbon dioxide depends on the acidity of the electrolyte; in aqueous solutions the solubility of CO_2 is significantly low and in form of carbonate or bicarbonate that induce a buffer effect depending on the concentration of the different species present in the solution. Each species follows different ways to absorb on the catalytic surface and hence it will follow different reaction pathways forming different final products. The surface of the catalyst could be functionalized to enhance its hydrophilicity or hydrophobicity changing the availability of the hydroxide groups on the surface, and therefore control the selectivity towards specific products. The production of CH_4 and CH_3OH from methyl radicals is highly competitive: the functionalization with F^- groups increases the selectivity towards CH_3OH, while the OH^- functionalization lead to higher reactivity[31,32]. The use of a co-catalyst either decreases the activation energy barrier to facilitate the kinetic of the reaction and improves the selectivity towards the

products. As previously mentioned, the selectivity depends on the different ways of binding of the intermediate and on the potential of the co-catalyst used. An external bias applied could easily determine the nature of the products generated for example suppressing the HER and promoting the CO_2 reduction. More negative is the potential applied and more complex molecule are formed (see Table 1.1).

The main studies of the last years are focused on piloting the adsorption and activation of the CO_2 molecule on the photocatalyst and on drive the product selectivity favoring different reaction pathways (Scheme 1). Lu *et al.*[33] demonstrated that the electron transfer step to form the $CO_2^{\bullet-}$ intermediate (that is then followed by the protonation step that leads to COOH*), is the rate determining step (RDS) in the CO_2 reduction to CO when noble metals are used as catalyst; Ma *et al.*[34] on the other hand, claim that on Ag surface the formation of the $CO_2^{\bullet-}$ intermediate is quite difficult and both the steps (electron transfer and protonation) could be the RDS. A particular case is the Cu as catalyst: with copper there is first the $CO_2^{\bullet-}$ formation and successively the reduction proceed with the formation of CO or $COOH^-$ depending on the subsequent rate determining steps and on the electrolyte[35]; from the CO intermediate the reduction proceeds to alcohols and hydrocarbons applying more negative potentials.

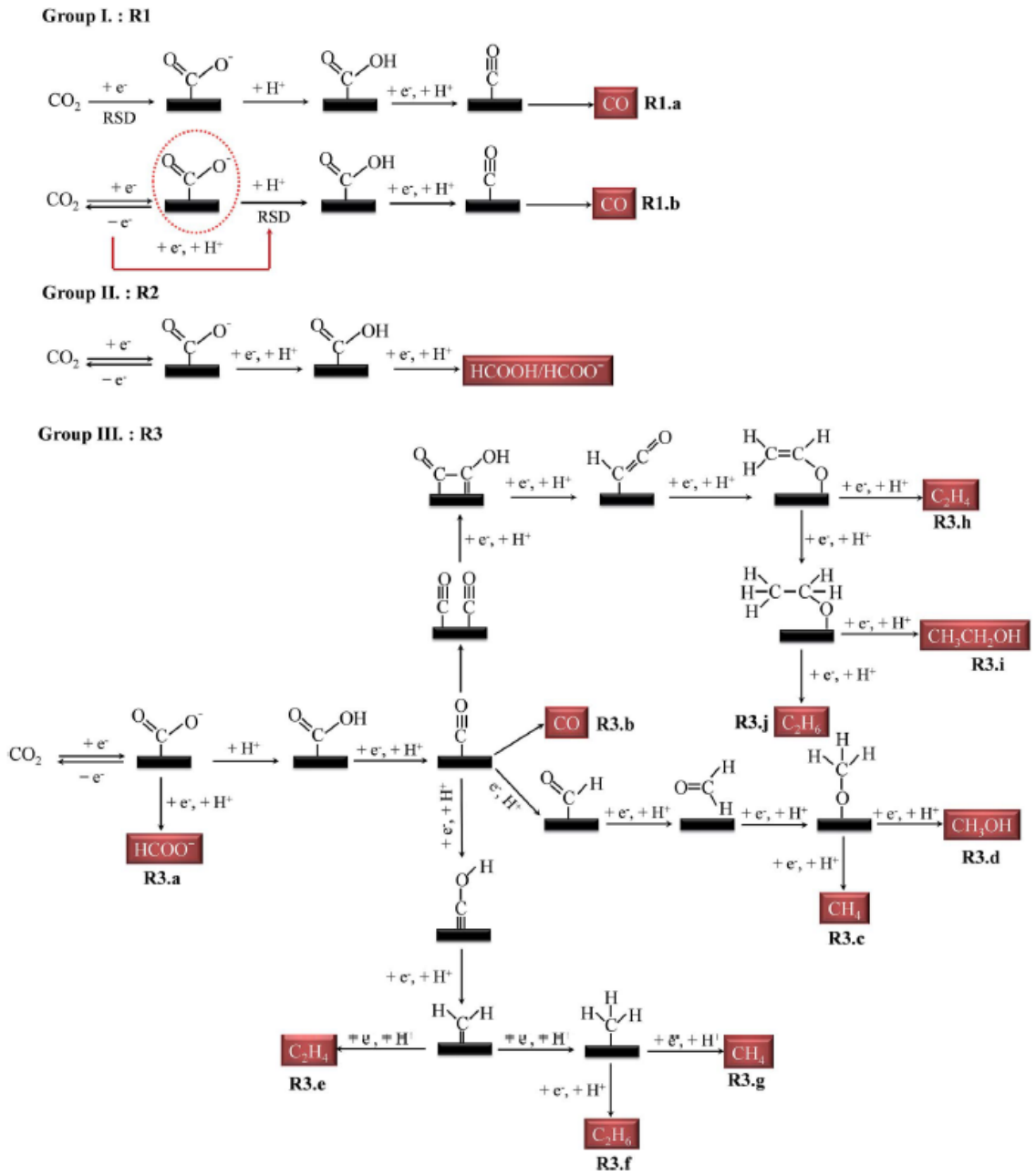

Fig 1.6: Different CO_2 absorption mechanisms on the catalyst surface and relatives products (R1, R2 and R3)[36].

To induce the formation of specific products of the carbon dioxide reduction it is important to know the efficiency of the corresponding reaction.

The efficiency of a generic reaction is defined as the quantity of the molecules produced per hour per amount of catalyst.

$$R = \frac{[Products]}{Time * [Catalyst]} \qquad (1.2)$$

In order to assess the efficiency of CO_2 reduction it is important to analyze each single parameter of the equation. First of all, the reaction is composed of different steps which could produce more than one single product. The competing production of H_2 in particular, decreases the efficiency of the reduction affecting the numerator of the equation (1.2). In reaction mediated by light (photoreduction) in addition, the formation of the products is not linear with the irradiation time, but often a plateau is reached after a specific time, as the light scattering brings to a difficult penetration of the latter on the catalyst surface. The same trend is observed for the catalyst concentration, the products formation increases with the catalyst concentration up to a precise value after which a plateau is often observed. Even if the reaction is triggered by the light, carbon residues on the catalyst surface can undergo reduction, and therefore some molecules are detected also before illumination. Moreover, the catalyst is often a composite system where each single element performs a specific role in the CO_2 reduction (e.g. light absorption or charge transport): in equation (1.2), all these elements should be considered for the calculation of efficiency. Finally, also the dimensions and the design of the reactor could affect the efficiency, leading to a difficult comparison of results coming from different laboratories.

The Turn Over Number (TON), Turn Over Frequency (TOF)[37], the proton-coupled electron transfer (PCET) and the overpotential are other parameters used to evaluate the efficiency of a catalyst. The overpotential (η) is defined as the difference between the standard reduction potential for a reaction without the catalyst and the one of the catalyzed reaction. The proton-coupled electron transfer (PCET), is a common phenomenon in nature that decreases the activation energy in the catalytic enzyme transformation, and is therefore a parameter useful also to define the CO_2 reduction: as in the case of CO_2 on the surface of a catalyst, modulating the acidity and the position of the acidic or basic cofactors of an enzymatic catalytic centers, it is possible to access to the critical transition state and therefore to decrease the activation energy of the enzyme transformation. As said previously, the first step in the CO_2 reduction is the production of the radical anion $CO_2^{\bullet-}$, that is thermodynamically challenging; the PCET process helps in decreasing the thermodynamic barrier of the reaction making it more accessible.

The catalyst efficiency is also defined in terms of its duration, i.e the specific number of reaction cycles after which it will become inactive. This property is defined the Turnover Number (TON). Another way of defining it is considering the molecules of products formed per unit time and per mole of catalyst before deactivation. In homogeneous catalysis, this is called Turnover Frequency (TOF). The value of TOF is not well defined however in case of heterogeneous catalysis; sometimes is used to express a rate constant (K_{obs}) even if the rate constant depends also on the catalyst concentration; other times is defined considering also the number of reactants consumed.

1.3.1. Electrocatalysis

The electrocatalysis is a chemical process that brings together the principles of catalysis with the ones typical of electrochemistry. The electrochemical reactions are carried out in two separate half-cells, where the oxidation and reduction separately take place, at the surface of the electrodes through electrons exchange. The electrons are forced by an applied voltage to reduce the right species instead of recombining with the holes. The force movement of the electrons creates an imbalance in the charge neutrality in the half-cells that is balanced by the use of a selective membrane and an electrolyte, able to conduct ions and allowing them passage from and to the two compartments[38,39] .

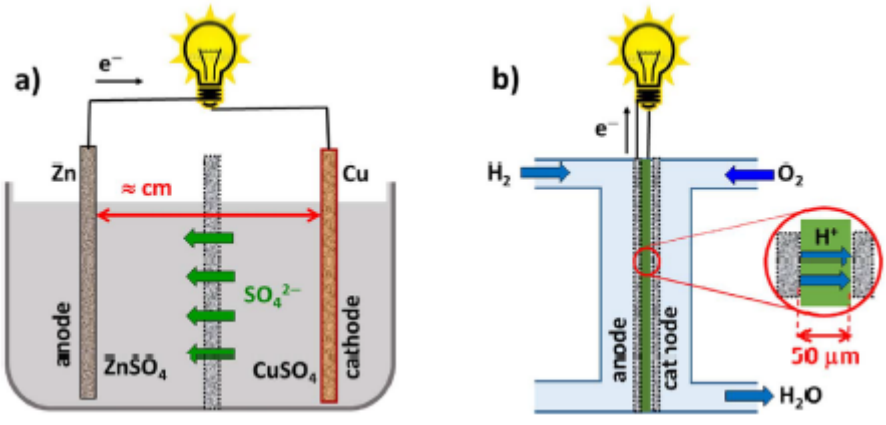

Fig 1.7: Different configuration of electrocatalytic cells, a) two-compartments cell and b) monolithic cell.

Figure 1.7 shows the two different possible configurations used for electrolysis: the two compartment and the monolithic cell. In the former the two electrodes are immersed in an electrolyte solution and separated by a membrane able to transport ions; in the latter the electrodes are directly in contact with the separation membrane.

The studies on the formation of new chemicals from CO_2 and water with these processes are mainly focused on new materials and designs able to accelerate the redox reactions involved acting on the interfacial charge transfer to facilitate the cleavage or the formation of new chemical bonds.

1.3.1.1. Electrocatalyst materials for CO_2 reduction

Several different materials have been tested for the electroreduction of CO_2; they can be classified in metal-organic complexes, metals, inorganic compounds and carbon-based metal free compounds[40,41].

The *metal-organic complexes* can be divided in two categories: the metal-macrocyclics and the metal-bipyridine complexes, where the most common transition metals used are Ni, Ag and Co. These electrocatalysts show high selectivity but they are produced through complicated synthesis routes and are characterized by low reduction activities and some toxic effects[42].

Metals are generally noble metals or their alloys and are classified depending on their selectivity. Sn and Pb in water-based electrolyte solution, form $HCOO^-$. Au, Ag, Pd, Zn and Bi bind on their surface the *COOH intermediate producing CO as final product. Cu on the other hand can react with *CO producing alcohols or intermediates such as *COH and *CHO. Metal alloys increase the kinetics of the electrocatalytic reaction and its selectivity, binding specific active intermediates, and as commonly formed with non-noble metals decrease the costs of the catalyst[43]. Examples of metal alloys are Au-Cu selective for CO; Ni-Ga alloys for production of methanol, ethylene and ethane; In-Cu and Cu-Sn for the CO formation and W-Au alloys that lead to methanol.

Inorganic compounds comprise metal oxides, metal chalcogenides and metal carbides. The firsts metal oxides used were RuO_2 and PbO which are selective respectively for HCOOH, CH_4, CH_3OH and HCOOH in $KHCO_3$ aqueous electrolyte; these two catalysts have

high issues of toxicity and high costs, and were replaced by other oxides such as SnO_x/CNT and Co_3O_4 for the production of HCOOH, or NiO for the syngas generation (CO and H_2). TiO_2 nanostructured film in acetonitrile electrolyte was found to be effective for the production of methanol binding CO_2 through the $*COO^-$ intermediates. Metal chalcogenides are based on transition metals such as Fe-Co and W. Ni-Fe_4S_4 and Co-Fe_4S_4 are used for the generation of methane and carbon monoxide, while DFT calculation showed that in MoS_2, $MoSe_2$ and Ni-MoS_2 *COOH and *CHO interact with S or Se atoms while *CO prefers the metal edge. Metal carbides like Mo_2C have advantages such as low costs, and better affinity with O (oxiphilic) rather than with C (carbophobic).

Carbon nanotubes (CNTs), graphene, carbon fibers as well as porous carbon are all *carbon-based metal-free compound*[44] have been poorly considered for the CO_2 reduction nevertheless it was found the doping with nitrogen enhance their performance. For CNTs for example, the doping with pyridinic N increases the conductivity and decreases the overpotential necessary for the reduction, as a consequence of the good binding compatibility of the nitrogen atom with the CO_2 intermediates.

1.3.2. Solar energy and CO_2 reduction

The CO_2 reduction can be conveniently operated using the energy that comes from the renewable solar energy. The photochemical conversion into chemicals species consists in the storage of the solar energy in the form of new chemical bonds; the conversion is particularly attractive for the high specific energy stored into the chemicals generated (55 MJ kg^{-1} for methane in comparison with <1 MJ kg^{-1} of present batteries)[45]. The process takes inspiration from the photosynthesis. In this process, the green plants harvest the solar energy and use it to convert water and CO_2 in alkyl chains and chemicals. The photosynthetic scheme has antenna systems[46] with two photo-excitation centers (Photosystem I and Photosystem II) which harvest in efficient way the sunlight, and reactor centers which are responsible of the electron transfer from donors to acceptors. Even if the complete process can be resumed in the reaction:

$$6\ CO_2 + 6\ H_2O + h\nu \rightarrow C_6H_{12}O_6 + 6\ O_2$$

the real mechanism is far more complex, comprehensive of two different reactions: the light reaction and the dark one also called Calvin cycle; as a whole the reaction is endothermic with $\Delta H = +470$ KJ mol^{-1} and $\Delta G = +2870$ KJ mol^{-1}.

The light reaction involves the photosystem I (PSI) and the photosystem II (PSII), where the photons coming from the sun are absorbed by the pigments presents in the leaves, and their energy allow the excitation of the electrons which cause the oxidation of the water molecules on the PSII and the formation of the nicotinamide adenine dinucleotide phosphate (NADPH) on PSI.

$$2\ H_2O + h\nu \rightarrow O_2 + 4\ H^+ + 4\ e^-$$

$$2\ NADP^+ + 2\ H^+ + 4\ e^- + 4\ h\nu \rightarrow 2\ NADPH$$

While these processes occur, the protons formed coupled with the electrons transfer (PCET), generate a change in the pH of the aqueous media, forcing the synthesis of the ATP.

In the dark reaction or Calvin cycle[47], the atmospheric carbon dioxide (CO_2) is fixated thanks to the ATP and NADPH synthesized during the light reaction. The cycle, reported in Fig 1.8b, involve 11 enzymes which catalyzed 13 different reactions that allow the synthesis of glucose. The Calvin cycle have to be repeated for 6 times in order to obtain one molecule of glucose.

$$6\ CO_2 + 12\ NADPH + 18\ ATP + 12\ H^+ \rightarrow C_6H_{12}O_6 + 12\ NADP^+ + 18\ ADP + 18\ p_i + 6\ H_2O$$

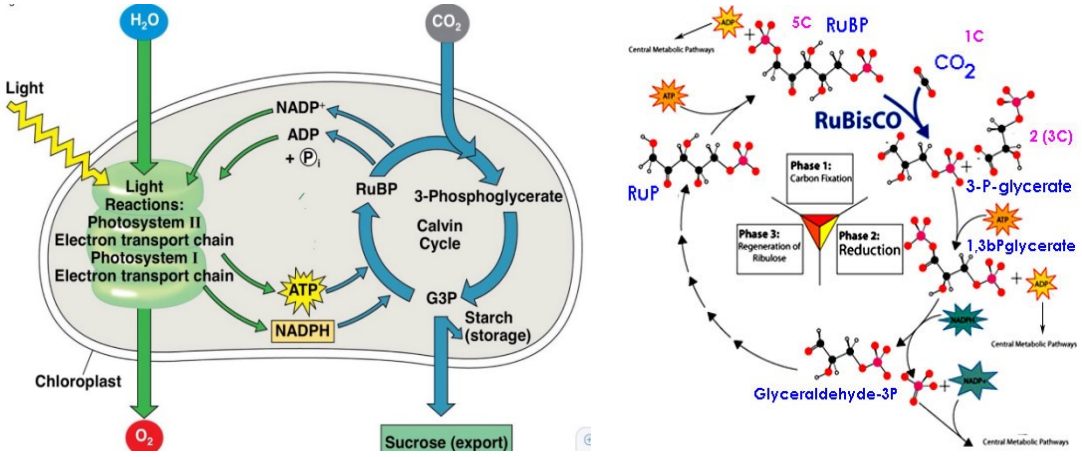

Fig 1.8: a) schematic process of photosynthesis and b) Calvin cycle.

The replication of the photosynthesis in laboratory is also known as artificial photosynthesis[48,49], using a device called artificial leaf where a similar mechanism is exploited for the water splitting and the CO_2 reduction. The artificial photosynthesis showed different problems from the practical point of view, first of all the energy demand for the conversion; while in natural photosynthesis the energy is provided by an efficient coupling of different subsystems, artificially this it is very difficult to manage. Moreover, in the natural system, the active centers are constantly regenerated thanks to a photo-protective mechanism, the rate of the delivery of energy on the reaction centers and the duration of the lifetime of the charge-separated are regulated and other protection are involved when the plants are exposed at an excess of light to avoid damages. Studies on the artificial leaf are growing: although the natural process is characterized by only 1% of quantum yield efficiency, enhancing the light harvesting and trying to reach selective reaction pathways, could bring to new targets[50]. As in the natural, also in the artificial photosynthesis four steps are involved: i) the sunlight absorption and harvesting, ii) the charge generation and separation, iii) the electrons and holes transfer on the catalyst surface and finally iv) the charge use in the redox reactions on the photocatalyst surface. In the whole mechanism the third step is the critical one because of the facile recombination of the charges just photogenerated, and the consequent loss in energy in form of heat (non-radiative emission) or light emission (radiative processes). The remained separated charges available on the catalyst surface are used for different redox reactions as a function of the surface properties of the catalytic material.

The photoreduction is developed in two different ways: the photocatalysis and the photoelectrocatalysis. In the latter case, the catalyst is supported on a substrate that acts as working electrode in three-electrodes configuration and the reaction is promoted by an external load. The two configurations will be discussed in detail in the next paragraphs.

1.3.2.1. Photocatalysis

IUPAC defined photocatalysis as *a change in the rate of a chemical reaction or its initiation under the action of ultraviolet, visible or infrared radiation in the presence of a substance, the photocatalyst, that absorb light and is involved in the chemical transformation of the reaction partners*[51].

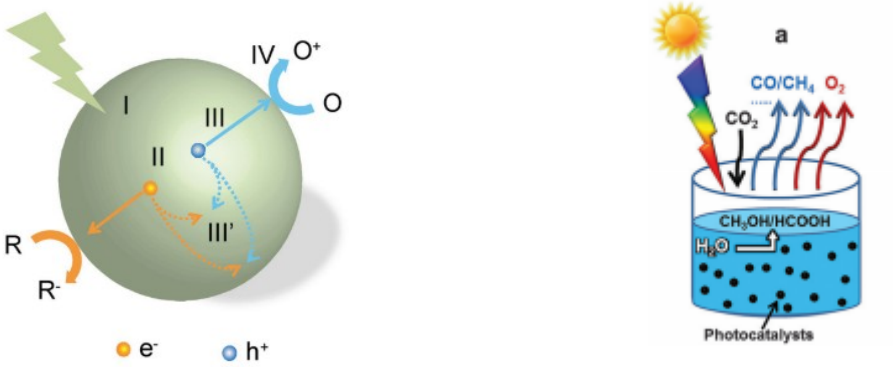

Fig 1.9: a) mechanism during the photocatalysis process and b) photocatalysis of CO_2.

The definition is suitable if photons act also as reducer of the activation energy and the reaction is thermodynamically spontaneous. On the contrary, when the reactions are endergonic ($\Delta G^0>0$) as in the fuels productions, the photoexcitation of the charges participates in active way inverting the ΔG^0 sign[45].

In general, in photocatalysis the driving force for the reduction of the carbon dioxide is only the solar energy and can be done in two different ways: heterogeneous or homogeneous[52]; in the first case, the catalyst in form of nanoparticles is suspended in an electrolyte solution, while in the second case, a molecular photocatalyst dissolved in water could harvest the light and promoted to the exited state. The photocatalyst has energy levels able to carry out both the water splitting and the CO_2 reduction but to facilitate the reactions, a sacrificial agent acting as oxidative or reducing quenching is

added to the solution, to capture oxidant species leaving the reducing one to assess the CO_2 reduction, or to catch the reducing species allowing the oxidation of the water (Fig 1.10).

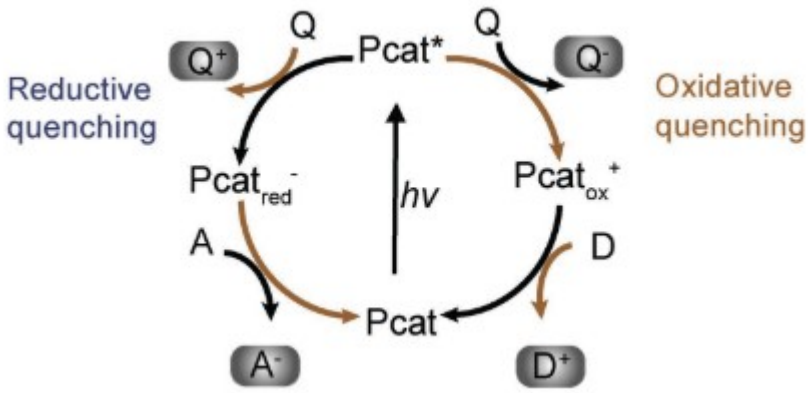

Fig 1.10: Use of sacrificial agents for enhancing the performances of the CO_2 conversion.

Some disadvantages are typical of the homogeneous photocatalysis: first of all, the complete solubility of the catalyst impedes the separation or the recovery of the catalyst from the electrolyte and the purification of the products is difficult. Moreover, the activity of the photocatalysis and its stability is strictly dependent on its molecular structure.

The most common configuration is the heterogeneous one, where the catalyst in form of nanoparticles is suspended in a solvent (often aqueous) where the CO_2 is dissolved. The reduction and the oxidation reactions are carried out on the active sites of the catalyst powder, in this way each particle acts as at the same time as photoanode and photocathode. Even if the process is a low cost one, the efficiency is very low. The products of reaction are mixed, together with the unreacted reagents at the end of the reaction. Moreover, being the reduced species in the same space of the charge photo-generated (in particular the holes) the re-oxidation of the reduced species generally occurs, obliging to a costly further step of purification of the products. The problem could be avoided or decreased using hole scavenger molecules which capture the holes impeding the oxidation of the products just reduced and reducing the holes avoiding its recombination with the electrons. Having nano-scaled dimension, the photocatalyst could have more active sites available but they tend to form aggregates and decrease their stability in water. Furthermore, major surface area means more possibility of

recombination. Finally, the light-scattering phenomenon due to the particle closer to the light source can impede the penetration of the light into all the system.

1.3.2.2. Photoelectrocatalysis

In a photoelectrocatalytic system, the cell is composed mainly by two electrodes with at least one photoactive, inserted in two different compartments, and an electrolyte. The photoelectrode is considered the working electrode (WE), the other is the counter electrode (CE), while a reference electrode (RE) is considered to measure the potential during the analyses and to help the electron-hole separation; the two compartments are separated by a Nafion membrane sensitive to H^+ ions and able to keep the gases products separated. To complete the assembly, a magnetic stirrer avoids pH gradient between the two compartments and increase the mobility of the reactants. Three different configurations of photoelectrochemical cell are commonly considered (Fig. 1.11)[53]:

- photocathode and dark anode
- dark cathode and photoanode
- photocathode and photoanode

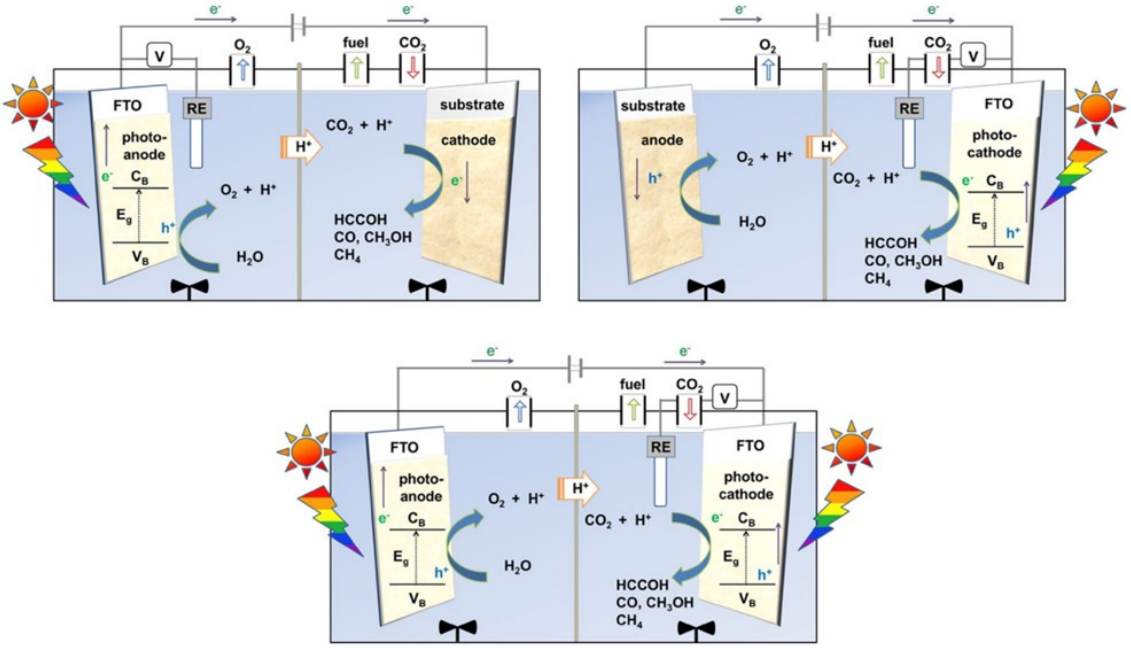

Fig 1.11: Three different configurations of a photoelectrochemical cell.

When only one electrode is photoactive, an external bias is applied in order to promote the conversion reaction, while in the ideal scenario when both the electrodes are photoactive the external bias could be avoided exploiting only the solar energy and the working electrode is defined depending on the reaction of interest (oxidation or reduction).

For the CO_2 reduction reaction when the active element is the photoanode, it acts as WE and is formed by a semiconductor able to perform the reaction, the CE is often Pt-based and the Ag/AgCl electrode is the RE. The RE and the WE are positioned in the anodic part of the cell, and the CE in the cathodic one. In the photocathode-based PEC system, the WE and the RE are hosted in the cathodic compartment while the CE is in the anodic part of the cell. In this configuration, WE is the photocathode and the reference electrode corresponds to a standard Ag/AgCl electrode while the counter electrode is a Pt wire or mesh. In the ideal PEC system, when both the electrodes are photoactive and there is no need of an external bias, the choice of the materials is fundamental. In particular the materials must absorb in the visible range of the electromagnetic spectra, they have to be stable in the electrolyte solutions and should allow the development of a Z-scheme configuration. The Z scheme consists in the electron transfer between the anode and the cathode without the use of the external voltage, furthermore the

oxidation of water and reduction of carbon dioxide should be simultaneous. For the CO_2 reduction in PEC configuration, the two semi-reactions are:

$CO_2 + H^+ + 2e^- \rightarrow HCO_2^-$ reduction of carbon dioxide

$2\ H_2O \rightarrow O_2 + 4\ H^+ + 4e^-$ oxidation of water

The oxidation of water in the anodic compartment generates the holes which moves through the Nafion membrane to the cathodic compartment thanks to the gradient of concentration; the reduction of CO_2 instead takes place in the cathodic compartment. When the photoelectrode is the photocathode, the electrons and holes are photogenerated on the cathode surface, the electrons reduce the carbon dioxide, while the holes pass through the selective membrane moving to the cathode surface to oxidize water. The opposite situation arises when the photoactive electrode is the photoanode: the photogenerated holes oxidize the water molecules present in the anodic compartment, while the electrons are transported thanks to the external bias in the cathodic compartments to reduce the CO_2 on the cathode. In contrast to the photocatalysis by suspension, in a PEC cell, the material is deposited as film on a conductive substrate, usually Fluorine doped Tin Oxide (FTO) or Indium doped Tin Oxide (ITO). Generally, in a photoanode configuration PEC, the semiconductive and photoactive material, is a n-type semiconductor, presenting an excess of electrons on the conduction band (C_B). In this configuration the photogenerated holes oxidize water and the electrons moves on the surface of the dark cathode to reduce the CO_2. On the other hand, when the photocathode configuration is used, the photoactive materials shows an p-type nature, hence having the valence band with a surplus of holes. With this system the photogenerated electrons could be used to generates fuels in the photoactive compartments, while the holes move to carry out the oxidation of water. To reach good selectivity levels of the products, the C_B of the photocatalyst have to correspond or at least be a more negative than the CO_2 reduction potential. On the other side the V_B have to be more positive than the oxidation of water potential. The electrolyte also plays an important role in the CO_2 photoelectrochemical reduction, the electrolyte is a solvent containing ionic species which gives the conductivity and restore a charge equilibrium in the whole system. Faradic efficiency and selectivity could depend

on the electrolyte nature, also the pH of the solution could influence the performance of the PEC cell.

1.3.2.3. Materials for photo- and photoeletrochemical conversion

A photoelectrode material must have semiconductive properties and therefore a material characterized by a valence and a conduction band separated by an energy band gap (Eg). When sunlight strikes the semiconductor with an energy greater or equal to Eg, the electrons (e^-) goes from the valence to the conduction band while holes (h^+) remain on the valence band.

The best efficiency in a semiconductive photocatalyst is reached using a material with a small bandgap, in this way a wide part of the visible region can be absorbed[54]. Unfortunately, many semiconductors have large band gap corresponding to absorption in the range of 400 nm; to achieve the red shift necessary to obtain a visible range absorption, the semiconductor is coupled or sensitized with dyes or organic molecule able to absorb the visible light. The use of nanoparticles (quantum dots) with a narrow-band semiconductors on the other hand, is useful because the photogenerated electrons migrate in the lower energy semiconductor conduction band while the photogenerated holes go in the opposite way on the more energetic valence band of the quantum dots, examples of this behavior are the couples CdS/TiO_2 or CdSe/ZnO couples.

In the case of organic molecules or dyes on the other hand, the coupling is between their HOMO and LUMO energy levels. In particular the energy of the LUMO of the dye have to be higher than the conduction band of the semiconductor material (Fig. 1.12).

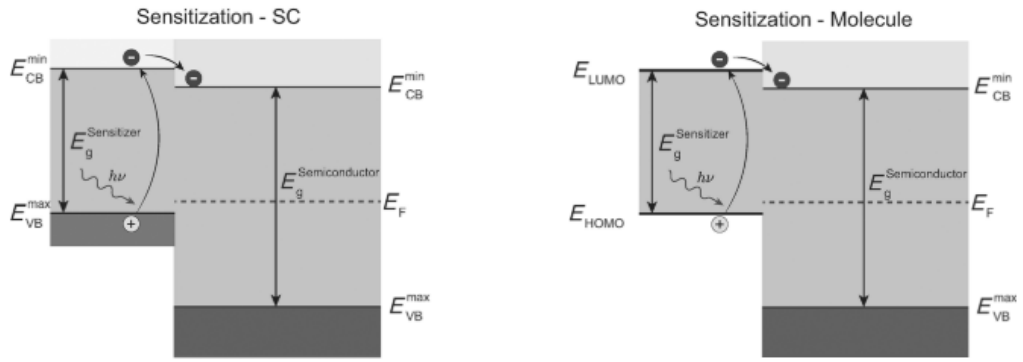

Fig 1.12: Energy levels of semiconductor with wide band gap combined with other semiconductor materials with narrow band gap or dye molecules absorber in the visible region[54].

Other strategies to decrease the band gap of the semiconductive materials, without any coupling is modifying the structure of the materials (Fig 1.13):

- Doping the structure with atoms as nitrogen (N_2), forming intraband states with higher energy than the valence band;
- Forming a solid solution of two or more different semiconductors to raising the valence band;
- Creating the intraband impurity states with oxygen vacancies between the valence band of the semiconductor and the Fermi level.

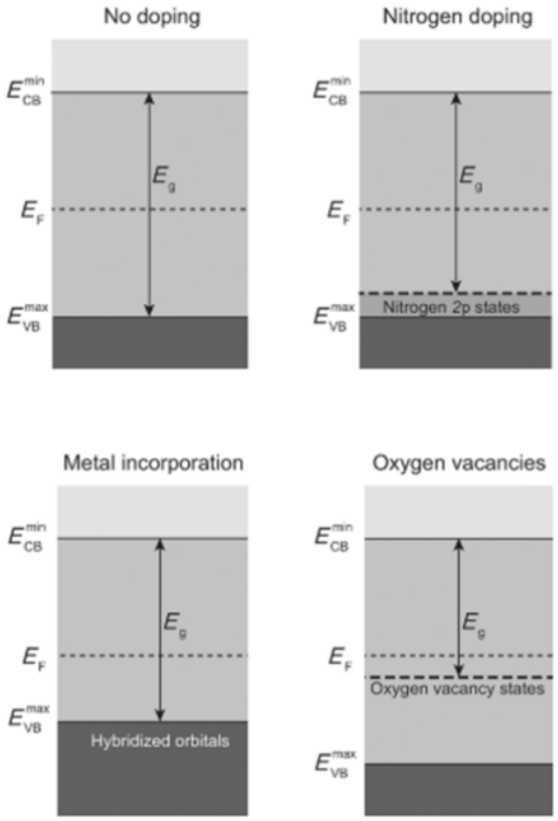

Fig 1.13: Strategies to decrease the band gap of the material[54].

In addition to the composition of the semiconductive materials, also the size and the crystal structures are parameters which influence the efficiency of the electrons promotion[55]. Nanostructured materials show completely different properties than the same material in bulk form. When the nanoscale is achieved, the surface of the material exposed, increases and as a consequence also the active sites available for the CO_2 reduction. Electronic and optical properties are related to the dimension of the particles because the movements of the charge carriers are limited in a small space as consequence of the quantum confinement effect while the band gap is inversely proportional to the size.

Also the light absorption depends on the size: in thin film photoelectrodes, the 95% of the light penetrate in a thickness of $3\delta_P$, where δ_P is the optical penetration depth, different for each material, therefore for thickness higher than this values the material is not active anymore.

The dimensionalities of the particles play an important role in the mechanism of the reaction pathway, therefore 0D, 1D, 2D and 3D structure are widely studied. 0D nanoparticles (NPs), are generally employed in photocatalysis where they could be well suspended. In 1D nanomaterials on the other hand one dimension is higher than the others: this definition is therefore associated to nanotubes, nanorods, nanowires or nanofibers. The light scatter is the results of the increased optical path length; in these materials than there is a definite increase in the charge transport property. With this configuration in fact, the light is trapped and scatters between the length of the nanowires or nanotubes enhancing the optical path length once again. With 2D materials, we consider nanosheets or nanoplates where the whole area is available to reacts, and it could be exploited as substrate for other catalytic materials. Assembling the 2D nanomaterials it is possible to obtain 3D complex structures that could be divided into ordered 3D and disordered 3D structures. While the latter do not induce any particular enhancement, the former give specific properties to the material.

Finally, the crystal structure is a determining factor for the semiconductive properties of a material. Single crystals or polycrystalline structures can be considered in this case: single crystals present low charge recombination and high mobility, while the polycrystalline compounds present high charge recombination as a consequence of the high charge mobility. With single crystals it is possible to choose different crystals facets to control the products of the reaction.

The semiconductive material more studied is *titanium dioxide* TiO_2: it shows good performances in pollutant degradation, water cleaning and dye bleaching reactions, and can promote the water splitting and CO_2 reduction.

Different crystallographic studies, surface and charge transport analysis have been conducted to better evaluate the mechanism and pathway of CO_2 reduction using the TiO_2. The great advantages of using TiO_2 is its low cost, its abundance and non-toxicity and the resistance from photo-corrosion. Its band gap is equal to 3.0 eV which corresponds to an absorption of 400 nm, hence in the UV range and the conduction band is at a potential of -0.16 V vs NHE at pH = 0 i.e. titanium oxide can either reduce protons or oxidize water. Titanium dioxide is present in nature mainly in 3 polymorphs: i) rutile, ii) anatase, and iii) brookite: the first two polymorphs are the most studied, especially for the photocatalytic CO_2 reduction. Both species are n-type semiconductors,

rutile shows a band gap of 3.2 eV while anatase of 3.0 eV. The difference is also observed in the position of the conduction band, with the one of anatase C_B is higher of 0.2 eV than the one of rutile.

The small difference in band gap give to similar properties in terms of photoreduction. Even if anatase is commonly considered the most efficient for the photocatalytic CO_2 reduction, a mixture of the two is considered the most useful: P-25 from Evonik (Degussa), composed by 80 % of anatase and 20 % of rutile, is commonly used as standard in photocatalysis[56–58].

From the mechanistic point of view, the single-electron reduction step to form the radical anion species, has an extremely negative potential compared to the conduction band of the TiO_2 and the step is thermodynamically forbidden. On the other hand, the proton reduction is favorite and therefore compete with the CO_2 reduction. The bigger disadvantage of using the TiO_2 as photocatalyst is its ability to absorb only in the UV region of the spectrum and hence only the 10 % of the total incident light that arrives on the catalyst surface can been used for the reaction.

Other catalysts have been studied to avoid this critical aspect, such as sulfides, oxides, nitrides and phosphides, to enhance the efficiency using materials with more negative C_B, and smaller band gap.

The *sulfides* are the first materials to attract attention after titanium dioxide for their more negative conduction band and a small band gap that allow the absorption in the visible region. The most common sulfides used are CdS and ZnS: the latter reduces CO_2 producing mainly formate, while CdS nanoparticles with a band gap of 2.4 eV lead to the production of CO. Even if their efficiency, these materials are however instable in aqueous environment when illuminated, as a consequence of the oxidation of the S^{2-} to sulfur or sulfates.

The *oxides* do not run into photooxidation problems like sulfides and are commonly divided into two groups: the d^0 transition metals ions, and the d^{10} coordination group of the transition metals. The first one includes Ti^{4+}, Zr^{4+}, Nb^{5+}, Ta^{5+}, V^{5+} and W^{6+}, all characterized by an empty *d* orbital, and other than in binary oxide they are used also in form of perovskites, oxide with general formula AMO_3. In this group, the excitation from the valence band to the conduction band of an electron is compared to an electron transfer from the oxygen to the metal which means that in these compounds, the *d*

character is significant. The conduction band position and consequently the band gap are inversely related to the electronegativity: the position of the conduction band increase with the decrease of the metal ion electronegativity, the WO_3 having the higher electronegativity present the most negative conduction band energy. The d^{10} group consist of Ge, Ga, In, Sn or Sb and they are often present in general formula M_xO_y or $A_xM_yO_z$. In the latter structure A is often represents as an alkali or alkaline earth cation, and they are stable in aqueous solution when irradiated. The conduction band of these compounds is particularly interesting as it is formed by occupied *s* and *p* hybridized orbitals, which lead to a high electron mobility in the semiconductor. When the oxides are in ternary configuration ($A_xM_yO_z$), M is often occupied by the cation Zn^{2+} because its orbital configuration allows the increase of the valence band position leaving the conduction band height unchanged and reducing the band gap.

Phosphides and in particular GaP and InP are p-type semiconductors: GaP reduces the CO_2 to methanol and formaldehyde with good yields, while InP is able to convert the carbon monoxide to formate.

1.4. Perovskites: an important class of electronic materials

Perovskitic materials have attracted great interest for a long time: they are compounds with a ternary structure (ABX_3) and ideal cubic structure, (Fig 1.14) where the B cation is at the corner of the cube, the A cation is at the center of the cube and the X anion (either oxygen or an halide) is located at the center of the cube edges, forming the octahedra BX_6.

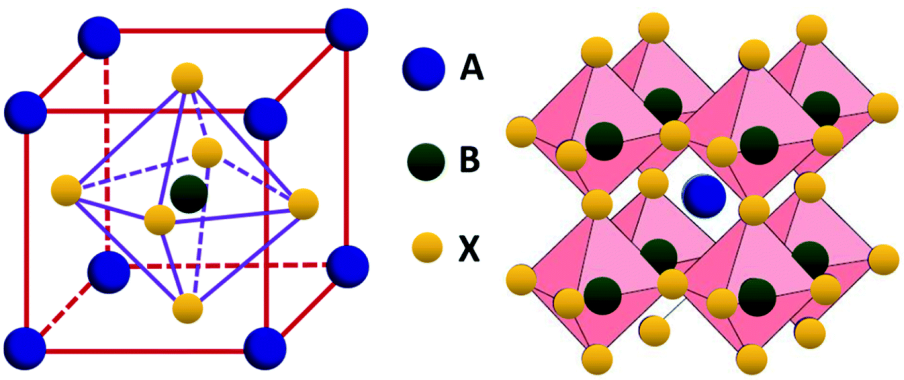

Fig 1.14: The ideal structure of the cubic ABX_3 perovskite[59].

The first perovskite considered, $CaTiO_3$ is the mineral that gave the name to the whole class of compounds.

These materials have a well-defined structure governed by the so-called tolerance factor t introduced by Goldschmidt, with formula:

$$t = \frac{(r_A + r_X)}{\sqrt{2}(r_B + r_X)} \qquad (1.3)$$

t is calculated with the ionic radius value of the elements used and must be between 0,8 and 1,1 to avoid the collapse of the crystalline structure. The use of the perovskites starts during the second world war as substituent for the mica, used as main insulator in capacitors: $BaTiO_3$ was considered (and it still is) for this purpose for its dielectric properties. Successively, these materials were studied for their important and different electronic properties such as ferroelectricity, piezoelectricity and superconductivity[59].

The perovskite can be produced using the conventional solid-state reaction or using chemical methods such as co-precipitation, sol-gel, hydrothermal synthesis eventually applying microwave heating to improve the homogeneity and reduce the dimensions of the particles[55,56]. The perovskites are commonly classified on the basis of the X atom in oxide or halide perovskites.

1.4.1. Oxide perovskites[60]

Perovskites show interesting properties such as ferroelectricity, dielectric properties, optical properties, superconductivity, multiferroicity or piezoelectricity. These properties together with the stable perovskitic structure make the perovskites excellent materials for many applications. They are used as sensors (gas, glucose or neurotransmitters sensors), solid oxide fuel cells, catalysts or solar cells.

They show good resistance to electric current, for this reason they are often used in capacitors. The dielectric behavior of the materials can be explained with the soft-mode model, referring to the parent compound $BaTiO_3$. Oxide perovskites with high dielectric

constant show spontaneous polarization if they are under the effect of an external electric field, showing ferroelectricity. Other important aspects of the perovskites are their good optical and photoluminescent properties, with many compounds showing an almost constant refractive index at different temperatures. $SrTiO_3$ and $CaTiO_3$ show similar absorption in the near infrared (NIR) range, characteristics widely exploited for infrared detectors. The photoluminescence is also of interest for its stability in different environments.

When they are cooled under specific temperatures perovskites exhibit superconductivity and show zero electrical resistance when an electric field is applied. While some compounds exhibit electric charges as a consequence of mechanical stress, i.e. they are piezoelectric materials, the polarization been proportional to the mechanical stress. If the material is exposed to an electric field on the other hand, it will undergo mechanical distortions, following the so-called inverse polarization effect.

Perovskites are also known for being multiferroic materials. Multiferroicity is the concomitance of ferroelectric (polarization of the material after the application of an electric field), ferromagnetic (magnetization of a material then the application of a magnetic field) and ferroelastic (deformation of a material after the application of a stress) abilities in a single material. The simultaneous presence of at least two of these three properties make the multiferroics materials interesting for memory devices and sensors.

Oxide perovskites $LaFeO_3$ and $SrTiO_3$ are used as gas sensors or for the detection of important chemicals as glucose or dopamine for their good bandgap, thermal stability and different size between A-site and B-site cations.

Oxide perovskite could be used also as components in the solid oxide fuel cells (SOFC) for their electrical conductivity compatible with the metal high ionic conductivity.

In catalytic field, perovskites are widely considered for the hydrogen and oxygen evolution and reductions reactions.

1.4.2. Halide perovskites

In the general formula ABX_3 of metal halide perovskites A corresponds to a monovalent cation or an organic group, B to a bivalent cation, Pb^{2+}, Sn^{2+} or Ge^{2+} and X is referred to a halide (Cl^-, Br^- or I^-). In Fig 1.15 is presented the ideal cubic crystal structure where A is at the vertices of the cube while B and X occupy the inside of the cube assembling in an octahedral structure (BX_6^{4-}).

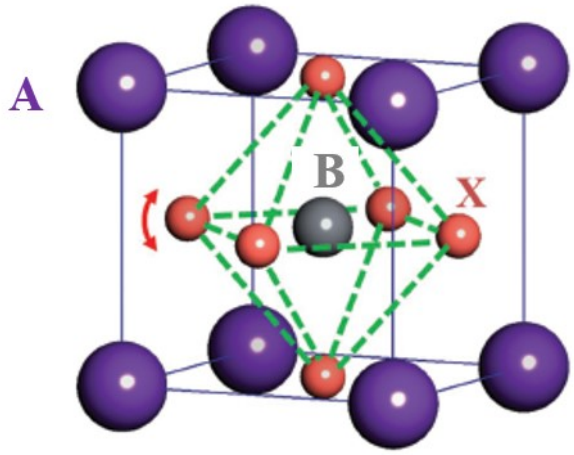

Fig 1.15: Structure of a generic cubic perovskite ABX_3.

Two main groups are part of this family of perovskites, the hybrid organic-inorganic halide perovskites (OHP) and the all inorganic halide perovskites (IHP). In the first one group, the component A correspond to an organic compound, often methyl ammonium [$CH_3NH_3^+$] or formamidinium [$CH_3(NH_2)_2^+$], while in the IHP, the monovalent cation is an inorganic cation, often corresponding to Cs^+, K^+ or Rb^+. These materials have to respect the aforementioned tolerance factor t to avoid issues in the perovskite structure. Hybrid organic/inorganic perovskites ($MAPbX_3$ or $FAPbX_3$) were the first metal halide perovskites studied for their promising properties when employed in solar cells. In particular their use pushes the photoconversion efficiency to 22%. OHP were firstly applies in the optoelectronic field, such as light emitting diodes (LEDs), photodetectors, laser or flexible electronics. Although the high success reached, the hybrid organic-inorganic lead halide perovskites showed important stability issues in ambient condition. Moisture, oxygen, light exposure and heat are causes of degradation of the perovskite structure; replacing the organic group with an inorganic cation, it is possible to

significantly increase the stability. The more suitable monovalent cation was found to be Cs^+, that leaded to development of an entire class of all inorganic halide perovskites: $CsPbX_3$, (X=Cl, Br or I).

1.4.2.1. Synthesis methods

In 2015 the Kovalenko group[61] developed an efficient synthesis route, the hot injection, obtaining $CsPbX_3$ nanocrystals (NCs); with this technique, a Cs-oleate precursor is prepared at high temperature and under inert gas and a solution of PbX_2 in octadecene is rapidly injected, forming immediately the $CsPbX_3$ NCs. The NCs obtained shown good photostability, high photoluminescent quantum yield (PLQY ≈ 90%), high melting point (T > 500°C), narrow line widths (12 - 40 nm) and wide colour gamut (≈ 140%). After the Kovalenko synthesis, a wide range of synthesis pathway was tried by other research groups to reduce the harsh conditions required by the abovementioned conditions.

In a very similar approach to the hot-injection synthesis Chen et al[62] used the same precursors and capping agents as well as the solvent of the Kovalenko hot injection, but in a single step and without inert gas and high temperature, obtaining the $CsPbX_3$ NCs with comparable properties, nano dimension and strong PLQY.

In the ligand-assisted reprecipitation method[63], the precursors CsX and PbX_2 are dissolved separately in a polar solvent, and then injected in a non-polar solvent. This synthesis route allows to achieve grams of product avoiding the inert gas and the high temperature need, is cheaper and rapid. The $CsPbX_3$ produced with this method shows optimal PLQY (≈ 90%) and high photostability. $CsPbX_3$ NCs are also synthesized through ultrasonication[64] where the precursors Cs_2CO_3 and PbX_2 are sonicated with the non-polar solvent 1-octadecene. The synthesis is not using polar solvents and allows to easily modify the halide ions thanks to the ion-exchange process, to control the thickness of the $CsPbX_3$ nanoplates. The solvothermal approach[65] allowed to reach hot injection comparable optical properties, and interesting morphologies such as nanowires.

The synthesis of all-inorganic halide perovskites has been investigated also changing the way in which heat is transferred to the precursors, passing from the use of a common hot plate with the silicon bath to the microwave assisted heating[66,67]. The use of

microwave heating allows the easy tuning of the possible morphologies and dimensionality of the particles just changing and modulating the capping ligands and the reaction parameters. Dimensions are dependent on the irradiation power set on the microwave reactors as demonstrated in Fig 1.16 while changing the ratio between the main capping ligands (oleic acid and oleylamine) lead to different morphologies (nanocubes, nanorods and nanosheets).

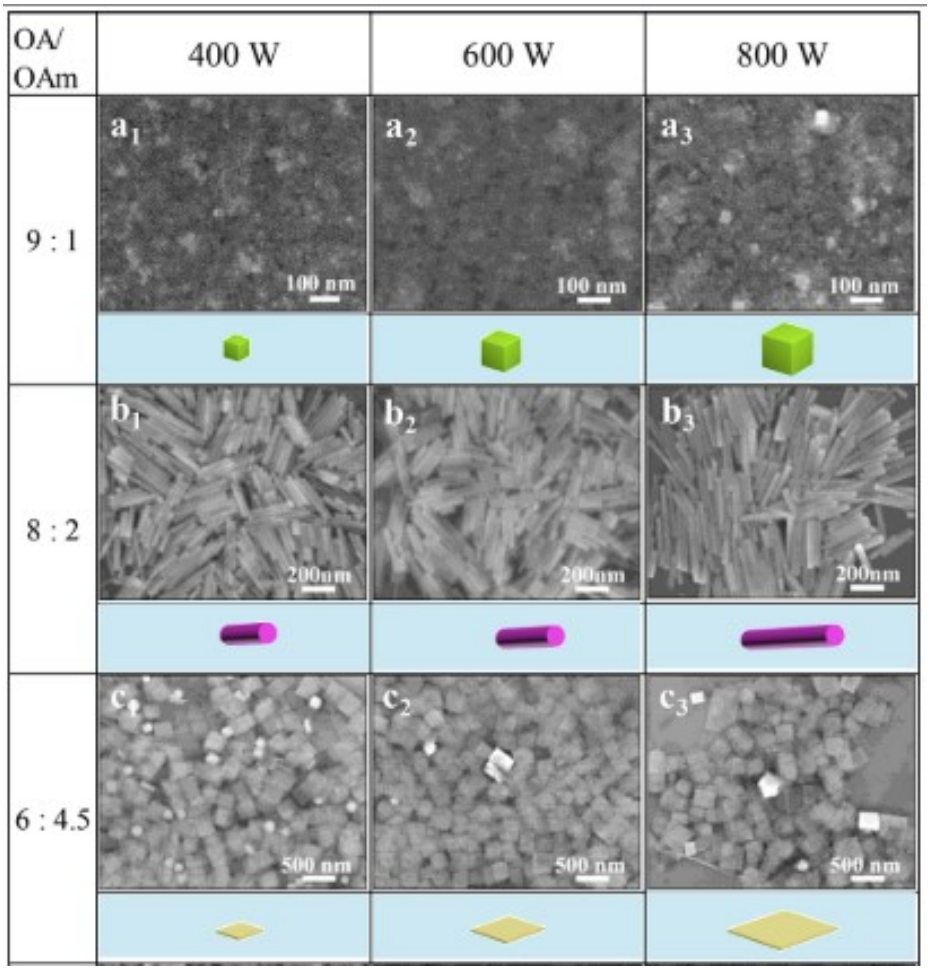

Fig 1.16: Different morphologies of the nanoparticles obtained with different microwave energies and ratio between oleic acid and oleylamine[67].

$CsPbBr_3$ single crystal has been obtained through a simple and fast room temperature synthesis[68]. The bromide salts precursors CsBr and $PbBr_2$ were dissolved in hydrobromic acid preparing two different solutions, and the solutions simultaneously added dropwise in a beaker containing HBr. The $CsPbBr_3$ precipitate can be convert into a single crystal through a thermic treatment. The crystal structure depends on the temperature: at

T=87°C it changes from orthorhombic to tetragonal and at T=127°C from tetragonal to cubic. As aforementioned the dimensionality of the semiconductor's particles is linked to its optoelectronic properties: for example, the single crystal and the bulk material, have different band gap value in comparison with the nanocrystals: 2.25 eV for the bulk $CsPbBr_3$ and 2.34 eV for NCs.

$CsPbX_3$ has also been produced via mechanosynthesis[69]. The halide salts are grinded, or ball milled at room temperature. The powder is obtained when the mixture of the powder turns from white to yellow. This synthesis is an optimal green approach that bypasses the use of toxic solvents and gives NCs with rapid charge-transfer properties interesting also for photocatalytic applications.

1.4.2.2. Halide perovskite properties

All the three species belonging to the halide all-inorganic perovskites($CsPbBr_3$, $CsPbCl_3$ and $CsPbI_3$) present semiconductor nature with band gaps ranging from 0.79 eV to 2.54 eV[70]. The value of the band gap is not only dependent on the halide present in the formula, but also from the structure of the lattice. The perovskite structure changes with the increasing of the temperature due to the distortion of the octahedra PbX_6 leading to a blue shift in the absorption spectra[71]. In addiction passing from Cl^- to the I^-, the atomic size increase, causing a decrease of the electrostatic forces between the external shell of the electrons and the inner nucleus. This caused the decrease of the band gap value. the optical properties of the halide perovskites were considered as the answer of the material to the incident photon flux. These properties could be summary in i) absorption coefficient, ii) energy loss function, and iii) refractive index. Their values were estimated thanks to computational calculations of the real and imaginary parts of the dielectric function[72]. Among all the three species, $CsPbI_3$ results the best to harvest the light (due to its bandgap) while the $CsPbCl_3$ presents a significant peak at high energy of the spectrum. This because it presents many electrons available to transit from the V_B to the C_B. For solar applications it is of high importance also to know the refractive index (n) of these materials. "n" was found to be optimal for $CsPbX_3$: $CsPbBr_3$, in particular in its

orthorhombic phase, shows a refractive index higher than the one of best natural refractive material: the diamond. For this reason, it could be used as artificial gemstone.

1.4.2.3. Halide perovskite applications

Halide perovskite are used in different applications. The most relevant for this thesis are examined in detail below.

Solar cells. The most common metal halide perovskite solar cells (MHPSCs) are based on the organic halide perovskite (OHP), these materials passed from a photocurrent efficiency (PCE) of 3.8 % of the first years to the more recently 25 %. Besides the progress in the PCE values, the stability issues of these materials in air lead to replace the organic cations with the inorganic ones in the same architecture used for the OHPSCs. The first inorganic halide perovskite solar cells (IHPSCs) based on $CsPbBr_3$, showed a PCE of 5.95 %. In the last years, the increased focus on the IHPSCs allowed the enhancement of the efficiency. Band gap and optical properties were significant in the solar cell construction[73]. $CsPbBr_3$ has a band gap of 2.34eV which is not ideal for solar cell applications; replacing bromine with iodine, the value drops to 1.73 eV in the right range for PV applications. The cubic $CsPbI_3$ however, is extremely instable in air and undergoes a transition from the cubic active phase to the inactive orthorhombic one. A mixture between bromide and iodine, $CsPb(I_{1-x}Br_x)_3$, is therefore considered to couple the stability of the $CsPbBr_3$ and the small band gap of the $CsPbI_3$.

The solar cells are commonly composed by a layer of compact TiO_2 (c-TiO_2) deposited on a fluorine doped tin oxide (FTO), and successive layers of mesoporous TiO_2 (m-TiO_2) with $CsPbX_3$ quantum dots (QDs) and a dense perovskite layer, an hole transport material and noble metals (Fig 1.17). The hole transport materials (HTM) are polymers such as poly[bis(4-phenyl)(2,4,6-trimethylphenyl)amine] while as noble metals Au or Pt are often used; both these materials increase the cost of the solar cells and are sometimes replaced with a layer of carbon electrode.

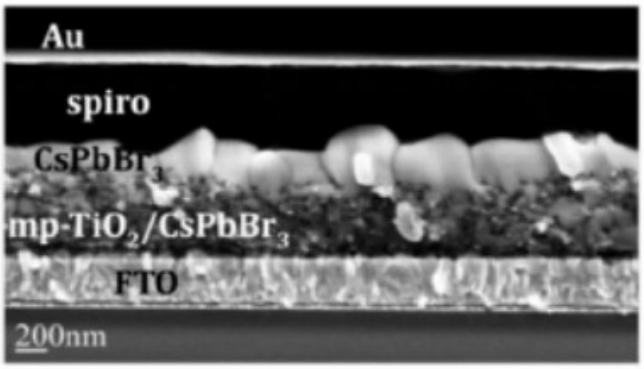

Fig 1.17: Section of a typical structure of all inorganic halide solar cell.

The inorganic halide perovskites are characterized by a good stability: they resist in humid air (≈90%) and at T=25°C for 3 months, and to strong temperature cycles (from 100°C to -22°C).

Light emitting diodes LEDs. $CsPbX_3$ are widely used for LEDs application, both for lighting and displays. LEDs with $CsPbX_3$ perovskites can be tuned from blue to orange modulating the composition of the anions present in the structure. Like in solar cells, the $CsPbX_3$ shows instability issues due to its ionic structure. To improve the performances the perovskites were coated with semiconductors shells or were passivated with organic and polymeric molecules. It is possible to control the passivation process used during the production to avoid the excess of insulating molecules at the interface between the different layers or reducing the long chain of the organic molecules; the length of the organic molecule chain is important also for the final stability of the device: without the right length, the LEDs signal decays after few minutes. The improvement of the charge transport is achievable also optimizing the configuration of the device or adding a charge injection barrier between the hole transporting layer and the perovskite $CsPbX_3$. Furthermore, washing the $CsPbX_3$ with a mixture of the ethyl acetate and hexane is used to control the amount of ligands present on the perovskite surface that can affect the recombination of charges. The external quantum efficiency (EQE) reached high values (20 %) for the green, red and near infrared regions but remain a great challenging the achievement of good EQEs in the blue region. Last researches showed the blue emission devices which use mixed Br and Cl halide perovskite[73].

Photodetectors. Photodetectors are devices sensitive to the light or other electromagnetic radiation and able to transform it in electric signals. The all-inorganic

perovskites are widely used as main component in photodetectors as a consequence of their high absorption efficiency (≈2x10^5 cm^{-1}) and large carrier mobility. To improve the external quantum efficiency (EQE), the $CsPbX_3$ film has to be compact and uniform with low roughness. A film with these characteristics is obtained through a dissolution-recrystallization process where a mixture of the toluene-ethanol is added to the $CsPbX_3$ film: the solvent evaporation activates the recrystallization of the perovskite's particles improving the film quality. $CsPbBr_3$ is considered in this application also for the possibility to tune the morphology of the crystals. It is common, for example, to use $CsPbBr_3$ nanosheets for 2D flexible photodetectors, characterized by a long carrier diffusion length and an intense light absorption. These devices show a high on/off photocurrent ratio, short rise and decay times and they exhibit good flexibility. To enhance the conductivity, the $CsPbBr_3$ can be mixed with carbon nanotubes (CNTs) to reach better performances preserving at the same time, the signal flexibility.

Lasers. All inorganic halide perovskites exhibit low density defects and high absorption coefficient, properties important for lasing applications. They show a very low threshold and an easy tunable emission wavelength from blue to red thanks to the possibility to modify the synthesis in order to obtain different shape and size. The properties can be furthermore using single crystal ad a consequence of the reduced number of defects.

Photocatalytic application. $CsPbX_3$ is a potential photocatalyst for its low cost in synthesis and processing, tunable band gap, long diffusion length, high charge mobility, large absorption coefficient, ultra-high photoluminescence quantum yield, excellent stability in air condition and narrow band emission. $CsPbX_3$ nanocrystals have been considered in water depollution[74–77] for their ability to photodegrade and convert hazardous contaminants in harmless and smaller molecules when suspended in a solution reach of pollutants or dyes contaminants. The system is kept under agitation in dark for a precise time allowing the absorption and desorption equilibrium between the catalysts and the molecules to be degraded. Then during the visible light exposure, the degradation of the pollutant by the perovskite take place following the mechanism reported below:

$$CsPbX_3 + h\nu \rightarrow CsPbX_3(h^+) + e^-$$

$$O_2 + e^- \rightarrow O_2^-$$

$$HO_2^- + H^+ \rightarrow H_2O_2$$

$$H_2O_2 + e^- \rightarrow {}^{\cdot}OH + OH^-$$

The holes and the electrons generated by the light into $CsPbX_3$ interact with water, through a radical mechanism that leads to the formation of the ·OH species. ·OH is a strong oxidant able to degrade the pollutant.

In general, the ability of a photocatalyst to degrade a pollutant is tested on specific dye molecule, such as rhodamine B (Fig 1.18).

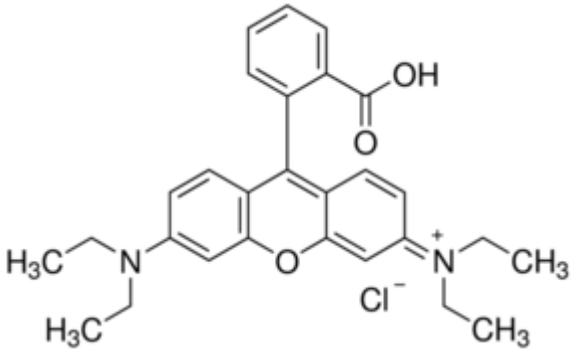

Fig 1.18: Structure of Rhodamine B molecule

In this case the degradation mechanism consists in 3 steps: N-de-ethylation, cleavage of the chromophore and the mineralization of the dye. The first step is the less significant one and consists in the successive loss of the ethylene groups in the rhodamine B structure. In the second step (cleavage of the chromophore), the more significant one, for each N-de-ethylation the dye molecule can formed different species. In water-based environment, after the sunlight absorption by the photocatalysts, the holes generated reacts with water molecules forming additional ·OH species useful to enhance the degradation process. Of all the halide perovskites, the $CsPbCl_3$ seems to be the better in terms of degradation performance, reaching 90% of degradation in 180 minutes. Furthermore, $CsPbX_3$ can be used for more than one cycle, improving the life of the catalysts. In recent times, $CsPbX_3$ are employed also in H_2 evolution, CO_2 reduction or for organic synthesis reaction[78–80]. $CsPbBr_3$ is no active in the H_2 evolution but the substitution of Br with I ($CsPbBr_{3-x}I_x$) creates a band gap funnel which allows the improvement in the transfer of photogenerated electrons from the internal to the

surface of the sample increasing the photocatalytic activity. However, using an HBr saturate solution and adding Pt as co-catalyst, the efficiency in the H_2 evolution increases. The formation of new chemical bond through photocatalysis is a goal of many researcher for the development of new drugs or materials. In order to do so, the photocatalyst should possess good charge separation and transfer, properties typical to all inorganic halide perovskite. The photons generate the electrons and holes, able to reducing and oxidizing molecules, which do not have to recombine and reach the catalytic site where the reaction takes place. As aforementioned the stability of the catalyst during the reactions depends on the solvent: in organic nonpolar solvent $CsPbBr_3$ is stable for various weeks; in polar solvent the photoluminescence of the perovskites collapsed indicating the instability in such environment. The presence of different anions in solution or in the substrate can affect the properties of the perovskite through an anion exchange reaction during the irradiation time to form hybrid structures, such as for example $CsPbBr_xCl_{3-x}$. The modification of the stoichiometry prevents the reusability of the catalysts, while using halogen free solvents and/or substrates the reusability is guarantee. The real and great advantage of the $CsPbBr_3$ and in general of $CsPbX_3$ perovskites is the air stability and tolerance that avoid the need of external protection with N_2 as inert gas. The reactions of oxygen evolution and production of solar fuels and chemicals require a good stabilization of the semiconductor in aqueous electrolyte. $CsPbBr_3$ displays better stability in air condition and hence to the moisture, oxygen and light than the hybrid organic perovskite. Nevertheless, it presents a lot of issues in water environments where it undergoes dissolution and morphology change after only few seconds.

1.4.2.4. Instability issues

$CsPbX_3$ showed a better stability in air than the hybrid organic-inorganic lead halide perovskites, nevertheless the aqueous environment remains an issue also for the all-inorganic perovskites. The contact between water molecules and the pristine $CsPbX_3$ caused a dissolution and degradation of their initial structure. The stabilization of the $CsPbX_3$ in water depends on the synthesis way and the use or not of capping ligands,

which with their long alkyl-chain could passivate partially the surface of the inorganic particles limiting its dissolution. The passivation of the surface can be obtained also with layers of inorganic materials such as TiO_2, SiO_2 or Al_2O_3. Some studies[81–83] reported the organic passivation of the $CsPbX_3$ surface with amines and their relative acids with different chains length or acidity and in stoichiometry or not stoichiometry ratio: the most commons are oleic acid and oleylamine. Other surfactants molecules such as trioctylphosphine oxide (TOPO), are used as capping ligands due to their strong steric effect. A way to assess the stability of these compounds is to measure their Photoluminesce Quantum Yield (PLQY). This property is strictly related to the stoichiometry of the system and therefore can give a useful indication of the retention of the structure. The surface stabilization of $CsPbX_3$ is the result of the interaction (hydrogen bond) between the NH_3^+ group of the oleylamine and the Br^- on the perovskite surface leading to a higher PLQY and to a better stability filling the Br^- or Pb^{2+} vacancy of the structure. Another type of passivation consists in the encapsulation the perovskite with polymers (polymethyl metacrylate, PMMA or polyvinyl pyrrolidone, PVP or with poly(maleic anhydridealt-1-octadecene), PMA). The anion exchange effect could be useful also to stabilize the perovskite synthetizing for example $CsPbBr_3@NH_4Br$ able to resist in water environment and having high absolute PLQY. On the other hand, the encapsulation with solid lipid nanoparticles lead to water stability up to two months. Another approach to the stabilization is the inorganic passivation[83–86], for example using metal-bromide passivation with $ZnBr_2$ or encapsulating the $CsPbX_3$ NCs with amorphous alumina (AlO_x) through the atomic layer deposition process (ALD). In this way after 45 days in air or under 8 hours of irradiation time, the PLQY is still high. ALD is also employed for the stabilization of $CsPbBr_3$ with silica luminescent sphere, this embedding allows to enhance the stabilization and to maintain the PLQY for the optoelectronic applications. Furthermore, the $CsPbX_3$ NCs could be encapsulated with a Ti-precursor forming $CsPbX_3/TiO_x$ and after a thermal treatment obtaining $CsPbX_3/TiO_2$. The encapsulated material shows a decrease in the PLQY but a significant enhancement of stability in water milli-Q environment.

1.4.2.5. Lead substitution

Besides all the good properties and characteristics of the inorganic halide perovskites, the presence of lead (Pb) in the structure remains an important issue. The Pb in fact, is highly toxic and hazardous to the people and to the environment. In order to replace Pb into the perovskite structure, the non-toxic metals, Bi, Ge, Sn or rare earths were taken into account[87,88]. The synthesis of the lead free $CsSnX_3$ was successfully reached tuning the band-gap in the near infrared spectra with the halide exchange process and the quantum confinement effect achieved thanks to the nanocrystal size of the particles. Nevertheless, tin presents in the structure is easily oxidized from Sn^{2+} to Sn^{4+} bringing to a low stability of the perovskite and lower efficiency in solar cells application[89]. Another alternative consists in the replacement of the lead with bismuth, changing the stoichiometry of the perovskite into $Cs_3Bi_2X_9$. These nanocrystals were synthetized showing absorption in the range between 400 to 560 nm, and a blue emission even if with low PLQY. Moreover, they show good stability upon 30 days when exposed to the air. Recently also the partial substitution of lead with other cations, as Zn, Sn or Cd was considered. These three cations enter in the structures thanks to a post synthetic cation exchange process[90] which causes a blue shift of the PL emission yet maintaining the high quantum yield. The blue shifting is due to the contraction of the lattice because of the smaller cations size in comparison with the Pb one. Manganese is employed in another partial replacement of lead[91]. The new system is considerably interesting for its double emission in the visible spectra even if the synthesis has to be carried out with strenuous conditions of high temperature and inert conditions.

As describe above, the research in the substitution or doping of the lead perovskite is still in progress, beside this many issues remains in form of stability and structure of the perovskites. The total replacement of lead remains today a great challenge.

1.5. References

1. Chu, S., Cui, Y. & Liu, N. The path towards sustainable energy. *Nat. Mater.* **16**, 16–22 (2016).

2. Ahmad, T. & Zhang, D. A critical review of comparative global historical energy consumption and future demand: The story told so far. *Energy Reports* **6**, 1973–1991 (2020).

3. Chu, S. & Majumdar, A. Opportunities and challenges for a sustainable energy future. *Nature* **488**, 294–303 (2012).

4. CO2 concentration. *CO2.earth* Available at: https://www.co2.earth/.

5. Höök, M. & Tang, X. Depletion of fossil fuels and anthropogenic climate change-A review. *Energy Policy* **52**, 797–809 (2013).

6. Day, C. & Day, G. Climate change, fossil fuel prices and depletion: The rationale for a falling export tax. *Econ. Model.* **63**, 153–160 (2017).

7. Arutyunov, V. S. & Lisichkin, G. V. Energy resources of the 21st century: problems and forecasts. Can renewable energy sources replace fossil fuels? *Russ. Chem. Rev.* **86**, 777–804 (2017).

8. Panwar, N. L., Kaushik, S. C. & Kothari, S. Role of renewable energy sources in environmental protection: A review. *Renew. Sustain. Energy Rev.* **15**, 1513–1524 (2011).

9. Blaabjerg, F. & Ma, K. Wind Energy Systems, reviews application of power electronics in wind energy systems. *IEEE Power Energy Soc.* **105**, 2116–2131 (2017).

10. Toledo, S., Rivera, M. & Elizondo, J. L. Overview of wind energy conversion systems development, technologies and power electronics research trends. *2016 IEEE Int. Conf. Autom. ICA-ACCA 2016* 9–14 (2016). doi:10.1109/ICA-ACCA.2016.7778454

11. Shoaib, M., Siddiqui, I., Rehman, S., Khan, S. & Alhems, L. M. Assessment of wind energy potential using wind energy conversion system. *J. Clean. Prod.* **216**, 346–360 (2019).

12. Nazir, M. S., Ali, N., Bilal, M. & Iqbal, H. M. N. Potential environmental impacts of wind energy development: A global perspective. *Curr. Opin. Environ. Sci. Heal.* **13**, 85–90 (2020).

13. Mcnew, L. B., Hunt, L. M., Gregory, A. J., Wisely, S. M. & Sandercock, B. K. Effects of wind energy development on nesting ecology of greater prairie-chickens in fragmented grasslands. *Conserv. Biol.* **28**, 1089–1099 (2014).

14. Saidur, R., Rahim, N. A., Islam, M. R. & Solangi, K. H. Environmental impact of wind energy. *Renew. Sustain. Energy Rev.* **15**, 2423–2430 (2011).

15. Kikuchi, R. Adverse impacts of wind power generation on collision behaviour of birds and anti-predator behaviour of squirrels. *J. Nat. Conserv.* **16**, 44–55 (2008).

16. Rypkema, H. A. Environmental Chemistry, Renewable Energy, and Global Policy. *Green Chem. An Incl. Approach* 19–47 (2018). doi:10.1016/B978-0-12-809270-5.00002-9

17. Lu, C. Geothermal Power Stations in China. 581–582 (1985).

18. Kanoglu, M. & Bolatturk, A. Performance and parametric investigation of a binary geothermal power plant by exergy. *Renew. Energy* **33**, 2366–2374 (2008).

19. Kabir, E., Kumar, P., Kumar, S., Adelodun, A. A. & Kim, K. H. Solar energy: Potential and future prospects. *Renew. Sustain. Energy Rev.* **82**, 894–900 (2018).

20. Solomon, S. C. *et al.* Whole Atmosphere Climate Change: Dependence on Solar Activity. *J. Geophys. Res. Sp. Phys.* **124**, 3799–3809 (2019).

21. Omara, A. A. M., Abuelnuor, A. A. A., Mohammed, H. A., Habibi, D. & Younis, O. Improving solar cooker performance using phase change materials: A comprehensive review. *Sol. Energy* **207**, 539–563 (2020).

22. Jamar, A., Majid, Z. A. A., Azmi, W. H., Norhafana, M. & Razak, A. A. A review of water heating system for solar energy applications. *Int. Commun. Heat Mass Transf.* **76**, 178–187 (2016).

23. Lingayat, A. B., Chandramohan, V. P., Raju, V. R. K. & Meda, V. A review on indirect type solar dryers for agricultural crops – Dryer setup, its performance, energy storage and important highlights. *Appl. Energy* **258**, 114005 (2020).

24. Evangelisti, L., De Lieto Vollaro, R. & Asdrubali, F. Latest advances on solar thermal collectors: A comprehensive review. *Renew. Sustain. Energy Rev.* **114**, 109318 (2019).

25. Koçak, B., Fernandez, A. I. & Paksoy, H. Review on sensible thermal energy storage for industrial solar applications and sustainability aspects. *Sol. Energy* **209**, 135–169 (2020).

26. Inganäs, O. & Sundström, V. Solar energy for electricity and fuels. *Ambio* **45**, 15–23 (2016).

27. Zhang, H. *et al.* Surface-Plasmon-Enhanced Photodriven CO2Reduction Catalyzed by Metal-Organic-Framework-Derived Iron Nanoparticles Encapsulated by Ultrathin Carbon Layers. *Adv. Mater.* **28**, 3703–3710 (2016).

28. Khezri, B., Fisher, A. C. & Pumera, M. CO2 reduction: The quest for electrocatalytic materials. *J. Mater. Chem. A* **5**, 8230–8246 (2017).

29. Hori, Y., Wakebe, H., Tsukamoto, T. & Koga, O. Electrocatalytic process of CO selectivity in electrochemical reduction of CO2 at metal electrodes in aqueous media. *Electrochim. Acta* **39**, 1833–1839 (1994).

30. Chang, X., Wang, T. & Gong, J. CO2 photo-reduction: Insights into CO2 activation and reaction on surfaces of photocatalysts. *Energy Environ. Sci.* **9**, 2177–2196 (2016).

31. Kwak, B. S. & Kang, M. Photocatalytic reduction of CO 2 with H 2 O using perovskite Ca x Ti y O 3. *Appl. Surf. Sci.* **337**, 138–144 (2015).

32. Ikeue, K., Nozaki, S., Ogawa, M. & Anpo, M. Characterization of self-standing Ti-containing porous silica thin films and their reactivity for the photocatalytic reduction of CO2 with H2O. *Catal. Today* **74**, 241–248 (2002).

33. Lu, Q. *et al.* A selective and efficient electrocatalyst for carbon dioxide reduction. *Nat. Commun.* **5**, 1–6 (2014).

34. Ma, M., Trześniewski, B. J., Xie, J. & Smith, W. A. Selective and Efficient Reduction of Carbon Dioxide to Carbon Monoxide on Oxide-Derived Nanostructured Silver Electrocatalysts. *Angew. Chemie - Int. Ed.* **55**, 9748–9752 (2016).

35. Hori, Y., Murata, A. & Takahashi, R. Formation of hydrocarbons in the electrochemical reduction of carbon dioxide at a copper electrode in aqueous solution. *J. Chem. Soc. Faraday Trans. 1 Phys. Chem. Condens. Phases* **85**, 2309–2326 (1989).

36. Khezri, B., Fisher, A. C. & Pumera, M. CO2 reduction: The quest for electrocatalytic materials. *J. Mater. Chem. A* **5**, 8230–8246 (2017).

37. Kozuch, S. & Martin, J. M. L. 'Turning over' definitions in catalytic cycles. *ACS Catal.* **2**, 2787–2794 (2012).

38. Roduner, E. Selected fundamentals of catalysis and electrocatalysis in energy conversion reactions—A tutorial. *Catal. Today* **309**, 263–268 (2018).

39. Pašti, I. A., Skorodumova, N. V. & Mentus, S. V. Theoretical studies in catalysis and electrocatalysis: From fundamental knowledge to catalyst design. *React. Kinet. Mech. Catal.* **115**, 5–32 (2015).

40. Zhang, W. *et al.* Progress and Perspective of Electrocatalytic CO2 Reduction for Renewable Carbonaceous Fuels and Chemicals. *Adv. Sci.* **5**, (2018).

41. Zhu, D. D., Liu, J. L. & Qiao, S. Z. Recent Advances in Inorganic Heterogeneous Electrocatalysts for Reduction of Carbon Dioxide. *Adv. Mater.* **28**, 3423–3452 (2016).

42. Guntern, Y. T. *et al.* Nanocrystal/Metal–Organic Framework Hybrids as Electrocatalytic Platforms for CO2 Conversion. *Angew. Chemie - Int. Ed.* **58**, 12632–12639 (2019).

43. He, J., Dettelbach, K. E., Salvatore, D. A., Li, T. & Berlinguette, C. P. High-Throughput Synthesis of Mixed-Metal Electrocatalysts for CO 2 Reduction . *Angew. Chemie* **129**, 6164–6168 (2017).

44. Vasileff, A., Zheng, Y. & Qiao, S. Z. Carbon Solving Carbon's Problems: Recent Progress of Nanostructured Carbon-Based Catalysts for the Electrochemical Reduction of CO2. *Adv. Energy Mater.* **7**, 1–21 (2017).

45. Stolarczyk, J. K., Bhattacharyya, S., Polavarapu, L. & Feldmann, J. Challenges and Prospects in Solar Water Splitting and CO2 Reduction with Inorganic and Hybrid Nanostructures. *ACS Catal.* **8**, 3602–3635 (2018).

46. Sayama, K., Mukasa, K., Abe, R., Abe, Y. & Arakawa, H. A new photocatalytic water splitting system under visible light irradiation mimicking a Z-scheme mechanism in photosynthesis. *J. Photochem. Photobiol. A Chem.* **148**, 71–77 (2002).

47. Raines, C. A. The Calvin cycle revisited. *Photosynth. Res.* **75**, 1–10 (2003).

48. Berardi, S. *et al.* Molecular artificial photosynthesis. *Chem. Soc. Rev.* **43**, 7501–7519 (2014).

49. Gust, D., Moore, T. A. & Moore, A. L. Solar fuels via artificial photosynthesis. *Acc. Chem. Res.* **42**, 1890–1898 (2009).

50. Bensaid, S., Centi, G., Garrone, E., Perathoner, S. & Saracco, G. Towards artificial leaves for solar hydrogen and fuels from carbon dioxide. *ChemSusChem* **5**, 500–521 (2012).

51. Braslavsky, S. E. *et al.* Glossary of terms used in photocatalysis and radiation catalysis (IUPAC recommendations 2011). *Pure Appl. Chem.* **83**, 931–1014 (2011).

52. Zhu, S. & Wang, D. Photocatalysis: Basic principles, diverse forms of implementations and emerging scientific opportunities. *Adv. Energy Mater.* **7**, 1–24 (2017).

53. Sangiorgi, N., Tuci, G., Sanson, A., Peruzzini, M. & Giambastiani, G. Metal-free carbon-based materials for electrocatalytic and photo-electrocatalytic CO2 reduction. *Rend. Lincei* **30**, 497–513 (2019).

54. Habisreutinger, S. N., Schmidt-Mende, L. & Stolarczyk, J. K. Photocatalytic reduction of CO2 on TiO2 and other semiconductors. *Angew. Chemie - Int. Ed.* **52**, 7372–7408 (2013).

55. Li, J. & Wu, N. Semiconductor-based photocatalysts and photoelectrochemical cells for solar fuel generation: A review. *Catal. Sci. Technol.* **5**, 1360–1384 (2015).

56. Miyagi, T., Kamei, M., Mitsuhashi, T., Ishigaki, T. & Yamazaki, A. Charge separation at the rutile/anatase interface: A dominant factor of photocatalytic activity. *Chem. Phys. Lett.* **390**, 399–402 (2004).

57. Li, G. & Gray, K. A. The solid-solid interface: Explaining the high and unique photocatalytic reactivity of TiO2-based nanocomposite materials. *Chem. Phys.* **339**, 173–187 (2007).

58. Boppella, R., Basak, P. & Manorama, S. V. Viable method for the synthesis of biphasic TiO 2 nanocrystals with tunable phase composition and enabled visible-light photocatalytic performance. *ACS Appl. Mater. Interfaces* **4**, 1239–1246 (2012).

59. Bhalla, A. S., Guo, R. & Roy, R. The perovskite structure - A review of its role in ceramic science and technology. *Mater. Res. Innov.* **4**, 3–26 (2000).

60. Assirey, E. A. R. Perovskite synthesis, properties and their related biochemical and industrial application. *Saudi Pharm. J.* **27**, 817–829 (2019).

61. Protesescu, L. *et al.* Nanocrystals of Cesium Lead Halide Perovskites (CsPbX3, X = Cl, Br, and I): Novel Optoelectronic Materials Showing Bright Emission with Wide Color Gamut. *Nano Lett.* **15**, 3692–3696 (2015).

62. Ye, S., Yu, M., Zhao, M., Song, J. & Qu, J. Low temperature synthesis of high-quality all-inorganic cesium lead halide perovskite nanocrystals in open air and their upconversion luminescence. *J. Alloys Compd.* **730**, 62–70 (2018).

63. Li, X. *et al.* CsPbX3 Quantum Dots for Lighting and Displays: Roomerature Synthesis, Photoluminescence Superiorities, Underlying Origins and White Light-Emitting Diodes. *Adv. Funct. Mater.* **26**, 2435–2445 (2016).

64. Tong, Y. *et al.* Highly Luminescent Cesium Lead Halide Perovskite Nanocrystals with Tunable Composition and Thickness by Ultrasonication. *Angew. Chemie - Int. Ed.* **55**, 13887–13892 (2016).

65. Chen, M. *et al.* Solvothermal Synthesis of High-Quality All-Inorganic Cesium Lead Halide Perovskite Nanocrystals: From Nanocube to Ultrathin Nanowire. *Adv. Funct. Mater.* **27**, (2017).

66. Pan, Q. *et al.* Microwave-assisted synthesis of high-quality 'all-inorganic' CsPbX3 (X = Cl, Br, I) perovskite nanocrystals and their application in light emitting diodes. *J. Mater.*

Chem. C **5**, 10947–10954 (2017).

67. Liu, W. *et al.* General Strategy for Rapid Production of Low-Dimensional All-Inorganic CsPbBr3 Perovskite Nanocrystals with Controlled Dimensionalities and Sizes. *Inorg. Chem.* **57**, 1598–1603 (2018).

68. Zhang, M. *et al.* Growth and characterization of all-inorganic lead halide perovskite semiconductor CsPbBr3 single crystals. *CrystEngComm* **19**, 6797–6803 (2017).

69. Jana, A., Mittal, M., Singla, A. & Sapra, S. Solvent-free, mechanochemical syntheses of bulk trihalide perovskites and their nanoparticles. *Chem. Commun.* **53**, 3046–3049 (2017).

70. Maqbool, M. *et al.* Structural, electronic and optical properties of CsPbX3(X=Cl, Br, I) for energy storage and hybrid solar cell applications. *J. Alloys Compd.* **705**, 828–839 (2017).

71. Saran, R., Heuer-Jungemann, A., Kanaras, A. G. & Curry, R. J. Giant Bandgap Renormalization and Exciton–Phonon Scattering in Perovskite Nanocrystals. *Adv. Opt. Mater.* **5**, 1–18 (2017).

72. Babu, K. E. Structural , Elastic , Electronic , and Optical Properties of Cubic Perovskite. **8**, 23–28 (2014).

73. Wu, Y., Wei, H., Xu, L., Cao, B. & Zeng, H. Progress and perspective on CsPbX3nanocrystals for light emitting diodes and solar cells. *J. Appl. Phys.* **128**, (2020).

74. Das, S., Paul, T., Maiti, S. & Chattopadhyay, K. K. Ambient processed CsPbX3 perovskite cubes for photocatalysis. *Mater. Lett.* **267**, 127501 (2020).

75. Gao, G. *et al.* Novel inorganic perovskite quantum dots for photocatalysis. *Nanoscale* **9**, 12032–12038 (2017).

76. Zhao, Y., Shi, H., Hu, X., Liu, E. & Fan, J. Fabricating CsPbX3/CN heterostructures with enhanced photocatalytic activity for penicillins 6-APA degradation. *Chem. Eng. J.* **381**, 122692 (2020).

77. Feng, X. *et al.* Highly Efficient Photocatalytic Degradation Performance of CsPb(Br 1- x Cl x) 3 -Au Nanoheterostructures. *ACS Sustain. Chem. Eng.* **7**, 5152–5156 (2019).

78. Guan, Z. *et al.* Perovskite photocatalyst CsPbBr3-xIx with a bandgap funnel structure for H2 evolution under visible light. *Appl. Catal. B Environ.* **245**, 522–527 (2019).

79. Shyamal, S. *et al.* Facets and Defects in Perovskite Nanocrystals for Photocatalytic CO2 Reduction. *J. Phys. Chem. Lett.* **11**, 3608–3614 (2020).

80. Zhu, X. *et al.* Lead halide perovskites for photocatalytic organic synthesis. *Nat. Commun.* **10**, 1–10 (2019).

81. Quarta, D. *et al.* Stable Ligand Coordination at the Surface of Colloidal CsPbBr3 Nanocrystals. *J. Phys. Chem. Lett.* **10**, 3715–3726 (2019).

82. Xin, Y., Zhao, H. & Zhang, J. Highly Stable and Luminescent Perovskite-Polymer Composites from a Convenient and Universal Strategy. *ACS Appl. Mater. Interfaces* **10**, 4971–4980 (2018).

83. Yang, D., Li, X. & Zeng, H. Surface Chemistry of All Inorganic Halide Perovskite Nanocrystals: Passivation Mechanism and Stability. *Adv. Mater. Interfaces* **5**, 1–13 (2018).

84. Loiudice, A., Saris, S., Oveisi, E., Alexander, D. T. L. & Buonsanti, R. Innenrücktitelbild: CsPbBr 3 QD/AlO x Inorganic Nanocomposites with Exceptional Stability in Water, Light, and Heat (Angew. Chem. 36/2017) . *Angew. Chemie* **129**, 11099–11099 (2017).

85. Li, Z. J. *et al.* Photoelectrochemically active and environmentally stable cspbbr3/tio2 core/shell nanocrystals. *Adv. Funct. Mater.* **28**, 1–7 (2018).

86. Xiang, Q. *et al.* Bottom up Stabilization of CsPbBr3 Quantum Dots-Silica Sphere with Selective Surface Passivation via Atomic Layer Deposition. *Chem. Mater.* **30**, 8486–8494 (2018).

87. Jellicoe, T. C. *et al.* Synthesis and Optical Properties of Lead-Free Cesium Tin Halide Perovskite Nanocrystals. *J. Am. Chem. Soc.* **138**, 2941–2944 (2016).

88. Yang, B. *et al.* Lead-Free, Air-Stable All-Inorganic Cesium Bismuth Halide Perovskite Nanocrystals. *Angew. Chemie* **129**, 12645–12649 (2017).

89. Lanzetta, L., Aristidou, N. & Haque, S. A. Stability of Lead and Tin Halide Perovskites: The Link between Defects and Degradation. *J. Phys. Chem. Lett.* **11**, 574–585 (2020).

90. Stam, W. Van Der *et al.* Highly Emissive Divalent-Ion-Doped Colloidal CsPb 1 −. (2020). doi:10.1021/jacs.6b13079

91. Dong, L. *et al.* Gram-scale synthesis of all-inorganic perovskite quantum dots with high Mn substitution ratio and enhanced dual-color emission. *Nano Res.* **12**, 1733–1738 (2019).

Chapter 2

Experimental

2.1. $CsPbBr_3$ synthesis methods

In this work, $CsPbBr_3$ was synthetized using three different synthesis pathways: the co-precipitation synthesis, the oleate synthesis and the microwave assisted synthesis.

2.1.1 Co-precipitation synthesis

4 mmol of CsBr (CsBr anhydrous 99.999%, Sigma Aldrich, Germany) were dissolved in a beaker with 4 mL of hydrobromic acid (HBr 47%, Merck, Germany), while 2 mmol of $PbBr_2$ (99.999%, Sigma Aldrich, Germany) were dissolved in another beaker with 2 mL of HBr. Both the solutions were simultaneously dropped in 0.5 mL of HBr: this addition caused the immediate formation of a brilliant orange precipitate. The latter was centrifuged (Sorvall Legend XTR Centrifuge, Thermo Scientific, USA) at 12000 rpm for 15 minutes, and the powder separated washed with 5 mL of ethanol by centrifugation at 12000 rpm for 10 minutes. The powder recovered was dried at 50 °C in a vacuum oven and then stored in a glass vial.

2.1.2 Oleate synthesis[92]

3 mmol of $PbBr_2$ (99.999%, Sigma Aldrich, Germany) and 1 mmol of Cs_2CO_3 (99.995%, Sigma Aldrich, Germany) were loaded in a two-neck flask. 100 mL of 1-octadecene (1-ODE, ≥95% Sigma-Aldrich, Germany) were used as solvent and two different capping ligands to tune the size and dimension of the particles: 5 mL of oleylamine (OLA, technical grade 70% Sigma-Aldrich, Germany) and 5 mL of oleic acid (OA, Honeywell, Austria). The obtained system was heated on a hotplate at 110 °C for 20 minutes under stirring; after this time, the suspension was cooled down and acetone was added to wash the $CsPbBr_3$ formed by centrifugation at 9500 rpm for 10 minutes. The collected crystals were dispersed in toluene or hexane with another centrifugation at 3000 rpm for 5 minutes. The suspension was stored in a glass vial.

2.1.3. Microwave assisted synthesis

A synthesis microwave oven (Milestone microsynth Plus, USA) was used for the synthesis of the $CsPbBr_3$. The microwave heating exploits the properties of specific chemical species to directly interact with the microwave radiation. In particular, the magnetons present into the MW oven, apply the electric field which is able to align the polar molecule of the chemical species. Changing the direction of the electric field, induces a rapid change in the alignment of the molecules' dipole generating heat. The effects of the MW heating are of two types: thermal and non-thermal (Fig 2.1), that influence the kinetic of the reaction and increase its velocity.

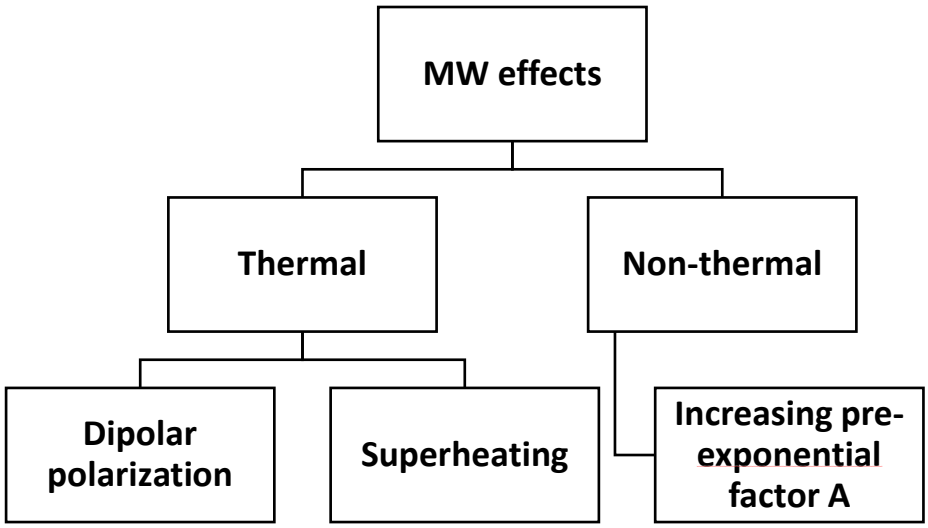

Fig 2.1: Schematic representation of the MW effects.

The increase in the velocity is due to the direct interaction between the material and the microwave radiation (thermal effects) on the other hand, the non-thermal effects control the Arrhenius law, increasing the pre-exponential A factor.

$$K = Ae^{-E_a/RT} \qquad (2.1)$$

where K is the reaction speed constant, A is the pre-exponential factor, E_a is the activation energy, T is the temperature and R is the universal gas constant.

3 mmol of $PbBr_2$ (99.999%, Sigma Aldrich, Germany) and 1 mmol of Cs_2CO_3 (99.995%, Sigma Aldrich, Germany) as two precursors were loaded in a two-neck flask. 100 mL of di diethylene glycol monobutyl ether (DGBE, Sigma Aldrich, Germany) were considered as solvent and 5 mL of oleylamine (OLA, technical grade 70% Sigma-Aldrich, Germany) and 5 mL of oleic acid (OA, Honeywell, Austria) were added as capping ligands to tune the size and the dimension of the particles. Different microwave cycles were considered changing the time and temperature of the reaction (described in detail in chapter 3). The suspension was cooled down and then centrifuged at 9500 rpm for 10 minutes with acetone to wash the crystals, another centrifugation cycle was then carried out to suspend the crystals in hexane or toluene. The powder was then dry and stored in an Eppendorf vial. A second set of trials were carried out using different ratio of precursors: 0.19 mmol of $PbBr_2$ (99.999%, Sigma Aldrich, Germany) and 0.025 mmol of Cs_2CO_3 (99.995%, Sigma Aldrich, Germany) in a 3 necked flask using 20 mL of 1-octadecene (1-ODE, ≥95% Sigma-Aldrich, Germany) as solvent, 2 mL of oleic acid (OA, Honeywell, Austria) and 2 mL of oleylamine (OLA, technical grade 70% Sigma-Aldrich, Germany).

2.1.4. Synthesis of the bP/$CsPbBr_3$ and GO/$CsPbBr_3$ hybrids[93]

The 2D materials were loaded in a 25 mL beaker with 0.5 mmol of Cs_2CO_3 (99.995%, Sigma Aldrich, Germany) and 1 mmol of PbO (≤10 µm, Sigma Aldrich, Germany), 5 mL of oleic acid (OA, Honeywell, Austria) and 5 mL of oleylamine (OLA, technical grade 70% Sigma-Aldrich, Germany). The system was heated at 160 °C under stirring, until the complete dissolution of the salts to have a limpid solution and then it was cooled down at room temperature. 5 mL of $CHCl_3$ (Sigma Aldrich, Germany) were added to dilute the obtained Pb-Cs oleate.

In another 25 mL beaker 0.2 mmol of tetrabutylammonium bromide (TBABr, ACS reagent ≥98%, Sigma Aldrich, Germany) were put together with 1 mL of OA and 4 mL of $CHCl_3$; the mixture was stirred at room temperature until the dissolution of the TBABr.

In a third beaker 1 mL of Pb and Cs oleate with 14 mL of $CHCl_3$ 1 mL of suspension of bP or GO 1mg mL^{-1} concentrated were stirred at room temperature for 5 minutes, then 2.5

mL of the precursor obtained with TBABr was quickly added to the Pb and Cs mixture causing the immediate precipitation of the $CsPbBr_3$ crystals on the 2D materials surfaces. The hybrids materials were left under stirring for 10 seconds and then centrifuged at 9500 rpm for 30 minutes to separate the solvents used during the synthesis from the hybrids; an additional cycle with acetone at 12000 rpm for 30 minutes was done to wash the product. For comparison, the same synthesis route was carried out to produce pure $CsPbBr_3$.

2.2. Photocatalytic tests

During the photocatalytic process the holes and the electrons generated by the light into the semiconductor material interacts with the solvent, through a radical mechanism that leads to the formation of the $^{\cdot}OH$ species[92].

$$\text{Semiconductor} + h\nu \rightarrow \text{semiconductor}\,(h^+) + e^-$$

$$e^- + O_2 \rightarrow O_2^-$$

$$e^- + O_2^- + H^+ \rightarrow HO_2^-$$

$$HO_2^- + H^+ \rightarrow H_2O_2$$

$$H_2O_2 + e^- \rightarrow {}^{\cdot}OH + OH^-$$

$^{\cdot}OH$ is a strong oxidant able to degrade the dye. In general, rhodamine B degradation mechanism consists in 3 steps: N-de-ethylation, cleavage of the chromophore and the mineralization of the dye. The first one is the less significant and consists in the successive loss of the ethylene groups of the rhodamine B structure. For each N-de-ethylation the rhodamine B molecule could formed different species in the second step (cleavage of the chromophore), which is the more significant one[30,94,95]. In water-based environment, after the sunlight absorption by the photocatalysts, the holes generated reacts with water molecules forming additional $^{\cdot}OH$ species. While the ethyl acetate having an hole scavenger role, can rapidly trap the photoholes (< 10 ns) inhibiting the recombination of the charge just photogenerated[96,97,98].

The $CsPbBr_3$ nanocrystals were tested in terms of photo-catalytic activity, following the degradation of Rhodamine B (≥95%, Sigma Aldrich) or methyl orange (in both water and

organic solvent (ethyl acetate, Sigma Aldrich). For these analyses a solar simulator (ABET technologies Sun 2000, Connecticut) calibrated with Silicon reference cell at 1000 W/m^2 AM 1.5 and a digital source-meter (Keithley, 2440 5A) was used. The analyses were done at 10 °C in a refrigerated reactor under stirring conditions: 1 mL of NCs suspended in hexane were dropped into the photo-reactor, and after the evaporation of the solvent, 40 mL of RhodB or MO solution with a concentration of 2.5 mg/L was added to the suspension. The mixture was then stirred for 30 minutes in dark before the tests under illumination. The amount of organic pollutant photodegraded was quantified with UV-Vis spectrophotometer in the range between 350 and 750 nm.

For the photocatalytic tests with hybrid $CsPbBr_3$/bP and $CsPbBr_3$/GO only the degradation of Rhodamine B was considered. 1 mg of $CsPbBr_3$/bP or $CsPbBr_3$/GO were loaded into the photo-reactor with 10 mL of Rhodamine B solution 2.5 mg/L concentrated. The mixture was then stirred for 30 minutes in dark before the tests under illumination. Also in this case, the amount of Rhodamine B photodegraded was quantified with UV-Vis spectrophotometer in the range between 350 and 750 nm.

2.3. Assembling of the PEC cell and photoelectrode production

The PEC was composed by two compartments, the anodic and the cathodic ones, separated by a Nafion membrane (Sigma Aldrich, 211). The cathodic compartment was filled with an electrolyte solution, ($KHCO_3$ 0.1 M, >98%, Sigma Aldrich, Germany) where was immersed the reference electrode (Ag/AgCl). The working electrode composed by the film of $CsPbBr_3$, was positioned on the side of the cathodic compartment in order to be reached from the light of the solar simulator. On the other hand, the anodic compartment filled with H_2SO_4 0.1 M (Sigma Aldrich, Germany) hosts the platinum mesh acting as counter electrode. The GC input was connected to the PEC cell while the three electrodes were connected to the potentiostat/galvanostat (PGSTAT 302N + FRA32M, Metrohm, Autolab).

The films were prepared with different techniques in order to make the electrodes to be used in a three electrodes cell for the electrochemical characterizations, and in the photoelectrochemical cell for the solar fuels production. The deposition methods used

were drop by drop deposition, spin coating and ink-jet printing. The films were deposited on a conductive substrate, doped fluorine tin oxide glass (FTO, 7Ω/sq, Sigma Aldrich, Germany) with and active area of 1 cm^2 of active area.

2.3.1. FTO glass cleaning

The pristine 5x5 cm FTO glass was cut to achieve a substrate with dimension 2.5 cm x 2.5 cm and it was sonicated with Isopropanol (anhydrous 99.5 %, Sigma Aldrich, Germany), washed with distilled water, and dried in oven at 100 °C for 10 minutes to remove any possible organic residue that could affect the final properties of the substrate.

2.3.2. Drop by drop deposition

The FTO glass was covered with a Kapton scotch to create the deposition area of interest and put on a hot plate at 110°C. 50 µL of suspension were dropped for 5 times on the active area of the FTO glass waiting 1 minute between each deposition.

2.3.3. Spin coating deposition

Spin coating is a deposition technique with which it is possible to achieve uniform thin film on a flat substrate. Many parameters have to be optimized to obtain a crack-free deposition: the spin speed and time, the acceleration and the thermal treatment between different depositions (baking). The process considers four steps (Fig 2.2):

- Dispense stage;
- Substrate acceleration stage;
- A stage of substrate spinning at a constant rate where the fluid viscous forces dominate the fluid thinning behavior;
- A stage of substrate spinning at a constant rate where solvent evaporation dominates the coating thinning behavior.

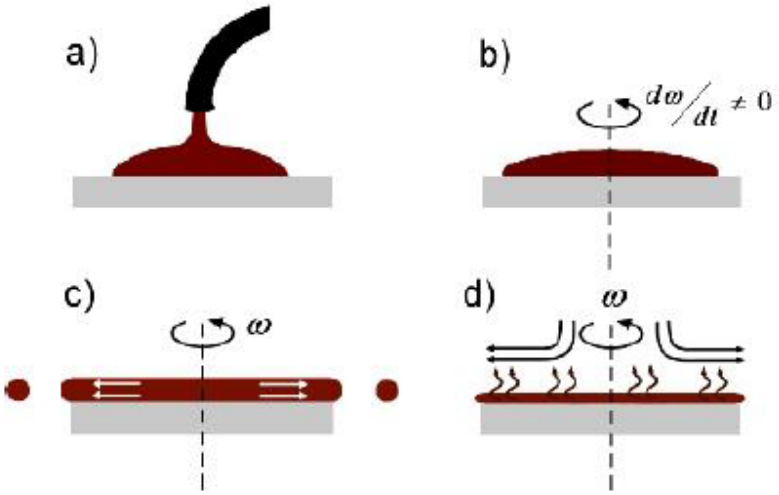

Fig 2.2: The four distinct stages to spin coating.

The *dispense stage* (that can be static or dynamic) consists in the deposition of the fluid at the center of the substrate. The static dispense stage is simply the deposition of the fluid on the substrate center at rest, the volume of the fluid depends on the viscosity and on the dimension of the substrate. During the dynamic dispense stage the fluid is deposited while the substrates turns at low speed.

The *substrate acceleration stage* is the phase where the fluid is distributed from the substrate center to the all surface due to the rotational motion. Initially, the fluid is not flat on the substrate but it has a definite thickness just in the center: this cause a twisting motion between the inertia at the top of the fluid and the substrate below which rotate faster; once the film reaches a suitable thickness, they co-rotate.

A *stage of substrate spinning at a constant rate and fluid viscous forces dominate fluid thinning behavior*: this stage is characterized by the gradual fluid thinning. Some edge effects are seen for the uniform flows of the fluid outward forming droplet on the edge of the film. The surface tension, the viscosity and the rotation rate are useful to control the uniformity of the film in this stage.

In the fourth and last stage (*A stage of substrate spinning at a constant rate and solvent evaporation dominates the coating thinning behavior*), the main process is the evaporation of volatile solvents. The coating gels thanks to the solvent evaporation, and its viscosity correspondingly increases.

The spin coating deposition were carried out with a POLOS Spin 150i-NPP, SPS Europe, spin coater, and with $CsPbBr_3$ suspensions both in hexane and in toluene. 20 cycles were considered for each deposition. The spin coating parameters deposition were set differently for the two solvents as reported in Table 2.3. 20 µL of suspension in toluene or in hexane were dropped on the conductive glass. After each deposition the samples were dried at 110 °C on the surface of a hotplate (POLOS 150).

Table 2.3: spin coating conditions of deposition

Solvents	Spin speed (rpm)	Spin acceleration (rpm s^{-1})	Spin time (s)
Hexane	250	125	20
Toluene	500	250	20

2.3.4. Ink-jet printing

The ink-jet printing is a common technology used in everyday life as manufacturing process for the deposition of various materials on various substrates. The materials to deposit are defined inks, and their formulation have to be studied and developed in order to be printed. The formation of single small drop is the main characteristics of the ink-jet printing: each small droplet of ink is created and deposited under digital control allowing the easy creation of complex patterns. In the digital process the position of the drops is on a two-dimension grid and can be modified also during the deposition allowing the correction of possible wrong patterns, for example. Another advantage of this technique is the possibility to use fragile substrates due to the absence of forces applied on the substrate for its non-contact nature. As mentioned before, the variety of materials that could be deposited and processed is huge even if the chemistry of the ink should be carefully controlled in order to respect the process constrained.

The inks are composed by different species: the liquid (water, organic solvent, crosslinkable monomers) which is the main vehicle of the ink, the additives (surfactants, preservatives, photo initiators) used to enhance the stability of the ink, and the active elements , i.e. the actual component of interest. The inks are classified in 4 types: i) phase-change ii) water-based, iii) solvent-based and iv) UV-curable. The phase-change inks are solid materials which are melted just before the moment of the injection. They

are used in application such as printing of bare code on non-porous substrates and they showed fast drying, good opacity and they are environmentally friendly; on the other hand, they are less resistant to the abrasions and they do not have durability. Water-based inks are environmentally friendly and inexpensive, they are perfect for deposition on porous substrates, while on non-porous ones the ink often does not adhere. Solvent based inks are the most common used thank to their high-quality printing, durability and the versatility substrates that can be considered. They are generally low cost, but they present environmental issues in addition to the increased clogging of the nozzle due to the fast drying of the volatile solvents. The UV curable inks are particularly interesting for their good stability as fluid until when they are irradiated with a specific wavelength. The real advantage of these inks is their application in a wide range of fields, from the traditional application to the more niche sectors of products for coatings, package decoration or labelling. The main disadvantages is the cost due to the UV curable hardware, and the impossibility, for health reason, to be used in food and edible packaging field[99].

Hansell in 1940 for the first time described the ink-jet printing process. He also indicated the parameters necessary to achieve a good print. These are illustrated in the so called "Magic Triangle of Ink-Jet Printing Technology" (Fig 2.3).

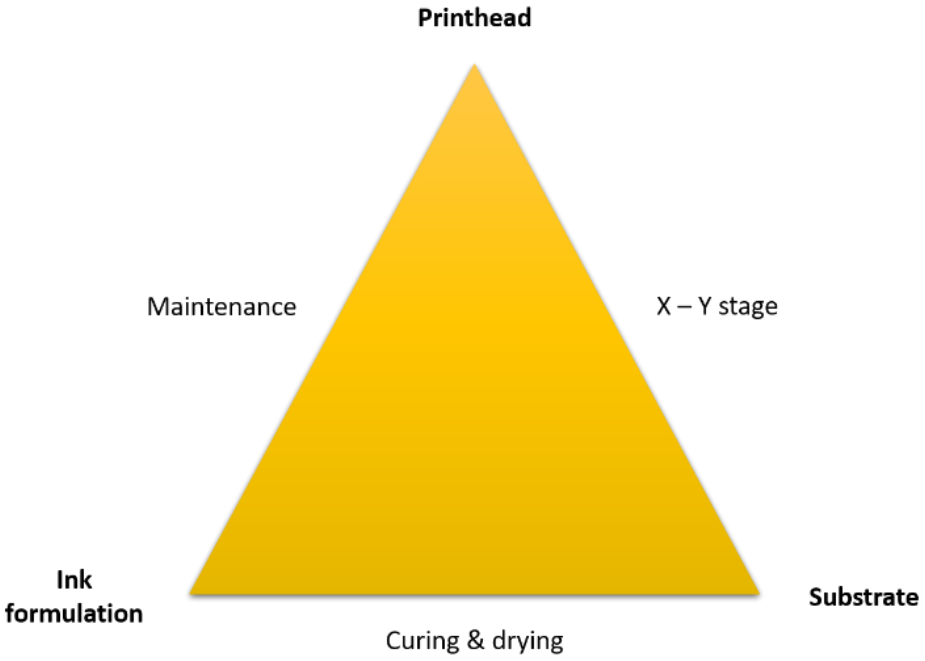

Fig 2.3: Magic triangle of inkjet printing technique.

The formation of the drops is ruled by physical properties, mainly viscosity and surface tension. These are included into the formula of two important dimensionless number: the Reynolds number and the Weber number:

$$Re = \frac{\rho\, d\, v}{\eta} \qquad We = \frac{\rho\, d\, v^2}{\sigma} \qquad (2.2)$$

Where ρ is the density of the ink, d is the diameter of the nozzle, v is the speed, η is the viscosity and σ is the surface tension. The two numbers present at the numerator represent the inertial of the fluid, and both includes the speed of the ink through the nozzle. They are commonly combined in a third dimensionless number, the Ohnesorge number (*Oh*)

$$Oh = \frac{\sqrt{We}}{Re} = \frac{\eta}{\sqrt{\sigma \rho d}} \qquad (2.3)$$

The *Oh* number represents the behavior of the jet emerging from the nozzle: if the Oh number is too high; the viscosity do not allow the separation of the drops at the exit of the nozzle. On the contrary, if *Oh* is too low, satellite drops will appear. To better understand the limits of the ink's physical properties the researcher considered the reciprocal of Oh commonly indicated with *Z.* This parameter should be between 1 and 10, for the ink to be printable (Fig. 2.4).

$$Z = \frac{1}{Oh} \qquad 1 < Z < 10 \qquad (2.4)$$

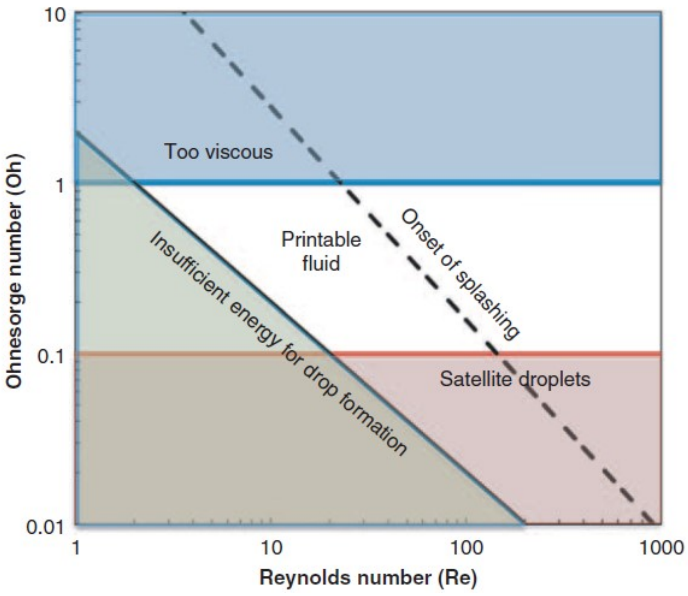

Fig 2.4: Range of printability determined by Re and Oh numbers[100].

Another property that has to be taken into account, is the interaction between the ink and the substrate, that influences the transformation of spherical drop into a flat dot. The transformation depends on the physical and chemical properties of both ink and substrate, and in particular the line width depends on the contact angle of the ink with the substrate. Another important parameter is the evaporation time of the carrier solvent of the ink: a non-perfect evaporation process often leads to the onset of the so-called coffee stain effect in which the major part of the material is on the edge of the droplet, or to some undesired morphologies such as bulging. To prevent these defects, the use of a mixture of solvents with different evaporation temperatures could be useful.

In general, if the temperature of the drying is too high or the time between each drop deposition is too long, the deposited drops are dried before the deposition of the next. On the other hand, if the temperature is too low and/or the time deposition between each droplet is too short, the line tends to exhibit bulges.

Ink-jet printing is carried out using the multi-deposition techniques station EXCEL (Aurel Automation) equipped with the microdrop printing head MD-K-140, with the nozzle diameter of 70 µm. Both the suspension of perovskite in hexane and toluene were analyzed measuring the surface tension and the contact angle. The main parameters

chosen for the printed head were: 1 second of time loop and a holding pressure of -10 mbar. The pulse voltage, pulse length and the frequency of the impulse are function of the formulation of the ink. Different trials were carried out on the $CsPbBr_3$ considering the pulse voltage between 201 and 230 V, pulse length between 75 and 135 µs and frequency from 116 to 1036 Hz. The conditions were set in order to obtain a unique, straight and stable jet of the ink. The optimal jet was achieved using a pulse voltage of 210 V, a pulse length of 75 µs and a frequency of 116 Hz. The substrate (FTO, Sigma Aldrich, Germany) was put on a hot plate during the deposition, changing the temperature in order to find the best compromise of solvent evaporation and film homogeneity. Three different temperatures were considered: 50 °C, 62.5 °C and 75 °C, keeping the distance between the nozzle and the substrate at 1.5 mm. The suspension was firstly deposited forming a line on the substrate, and multiple layers were deposited to increase the thickness: 5 and 10 layers were considered for each deposition. To reach a fully covered 1 cm^2 area, a serpentine path was optimized, setting the distance between each lines of the path at 550 µm. IR heating treatment was applied after the depositions, to dry the area, using the IR oven (Nannetti, R. I. 15, Italy) with a heating ramp of 5°C/min up to 80 °C and a dwell time of 10 minutes.

2.3.5. Deposition of the protective coatings

The protective coating of 10 nm layer of platinum (Pt target) or graphite (C, graphite braid packing) were deposited by sputtering (Quorum, Q150T ES, 2M strumenti, Italy).

2.4. Characterizations [92]

2.4.1. X-Ray Diffraction (XRD)

XRD analyses were performed at room temperature using a Bruker D8 Advance diffractometer (Bruker AXS GmbH, Karlsruhe, Germany) with a Bragg-Brentano geometry and an X-ray tube operating at 40 kV and 40 mA. Data were collected through a one-dimensional LynkEye detector based on silicon strip technology, set to

discriminate Cu *Kα*1,2 radiation, in the 10-80° 2θ measuring range, with an equivalent counting time of 10s per 0.02° 2θ step anode X-ray. Phase analysis of XRD collected data were performed by means of (PANalytical B. V., Almelo, The Netherlands). The $CsPbBr_3$ crystals were collected, in the 2θ region from 20° to 60° in 2Θ with 0.02° for 2θ-step and 5 s/step.

2.4.2. UV-Vis spectroscopy

UV-Vis spectroscopy is a technique based on the interaction of the electromagnetic radiation with the sample at a specific wavelength. When the matter absorbs the radiation, it produced excitation and de-excitation that can be detected as a spectrum. A ray is generated by a source, generally a tungsten lamp for the visible region and a deuterium one for the UV, and then it is direct to a monochromator that separates the polychromatic ray in a series of monochromatic bands. The resulting ray is split by a chopper into two rays directed to the sample and the reference. Finally, after interacting with the samples, the rays reach the detector that converts the energy in an electrical signal. UV-Vis spectra were recorded between 400 and 800 nm at 25 °C using UV-Vis spectrophotometer (PerkinElmer Lambda 35, Italy) at 25°C. The bandgap was calculated from UV-Vis spectra through the Tauc equation:

$$\alpha h\nu = A\ (h\nu - E_g)^n \qquad (2.5)$$

Where α is absorption coefficient, h is the Planck's constant (J·s), v is the light frequency (s^{-1}), A is the absorption constant and E_g is the value of band gap energy. The exponential n refers to the type of electronic transition specific to the semiconductor: 2 for indirect allowed transition, 3 for indirect forbidden transition, 1/2 for the direct allowed transition and 3/2 for the direct forbidden ones. In this work n = 1/2 was used. For the characterization of the film, the transmission spectra were recorded using the diffuse reflectance technique through the PVE300 system of Bentham (United Kingdom) and the integrating sphere in order to collect all the scattered light without any dispersion. The inner part of the sphere is coated by a barium sulfate layer, for its high

reflection properties in the visible range. The transmittance (T), is defined as the ratio I/ I_0 (I_0 is the intensity of the incident light and I the transmitted one), while the amount of absorbed light is instead defined Absorbance (A) calculated as Log T.

2.4.3. Scanning Electron Microscopy (SEM)

Scanning electron microscopy was used to observe the microstructure of the ceramic layers. This technique exploits an accelerated electron beam to scan the surface of the sample and register an image. This process generates different signals, the most used are the ones produced by secondary and back-scattered electrons. The first are electrons with energy up to 50 eV, coming mainly from the interaction between the beam and the nuclei of the atoms. In this case a field emission gun - scanning electron microscope (FEG-SEM ΣIGMA: Zeiss, Germany) was used. In this class of microscopes, the beam is produced by a tungsten single crystal, in this way the beam is smaller, more coherent and has a higher current density than the ones generated by traditional thermo-ionic emitters (LaF_6). The result is a significantly improved signal-to-noise ratio and resolution. During the investigation of the $CsPbBr_3$ particles, their average dimension was determined using ImageJ program.

2.4.4. Transmission Electron Microscopy (TEM)

With TEM is possible to achieve images thanks to the transmission of a beam of electrons which interact with the sample. The TEM microscopy is able to reach high magnifications and for this is often used for the nanomaterial's images. Transmission Electron Microscopy (TEM) studies were carried out using a Philips instrument operating at an accelerating voltage of 80 kV. Few drops of $CsPbBr_3$/bp or $CsPbBr_3$/GO suspension in tetrahydrofuran were placed on the TEM copper/carbon grid, air dried, and measured.

2.4.5. Thermogravimetry and Differential Scanning Calorimeter (TG/DSC)

Thermogravimetric analysis is the technique suitable to study the stability of the materials during a constant rate heating. The highly sensitive balance present in the instrument allows to recognize the losses or gains of weight due to different phenomena such as evaporations, decompositions, reductions, oxidations or absorptions and desorption's of gases onto porous materials. The analyses are always carried out with a carrier gas which protect the inner part of the instrument from the corrosion due to eventual species decomposed at high temperature. The DSC is perfect to determine the thermal transitions of a material such as the glass transition point, or the transition between different polymorphs. This information was recorded thanks to the measure of the heating flow produced with the constant increase of the temperature.
Scanning calorimeter (DSC) and thermogravimetric analyses (TGA) on a NETZSCH STA 449 F3 Jupiter (Germany) thermal analyzer were utilized to check the thermal evolution of the materials. The TG/DSC analysis of the $CsPbBr_3$ was collected in air condition, from 10 °C to 500 °C with a heating ramp of 10 °C/min.

2.4.6. Profilometry

Profilometry analyses were conducted to study the surface features of the deposited layers and to determine their thickness. To avoid damages to the surface of the samples induced by the stylus, a non-contact system was used (Contour GT-K 3D non-contact profilometer, Bruker, Germany). This system is based on white light interferometry i.e the wave superimposition principle in order to extract information from the results of the combination of waves. In particular the waves form a pattern dependent on the phase difference between them, which will generate a constructive or destructive interference. In practice, a CCD sensor is placed at the point where the two images are superimposed. A white light source (generally a laser) is used to illuminate the test and the reference surface, and the light is collimated by a lens. A splitter separates the light into the reference and measurement beams reflected by the reference mirror and from

the test surface respectively. The returning beams are then collected by the CCD sensor that converts the resulting interference pattern into the surface topography.

2.4.7. Surface tension and contact angle

Surface tension, expressed as mN m^{-1}, is a force acting at the interface between different phases (solid-liquid-gas) and for the liquids can be defined as the energy needed to increase the surface of a unit. This force is strictly dependent on the chemical-physical characteristics of the systems and by the thermodynamic equilibrium between the phases. Contact angle is related both to the surface tension and the thermodynamic equilibrium between phases, and it is analysed to measure the wettability of surfaces. Considering a droplet deposited on a horizontal surface, it can be defined contact angle the angle formed by the liquid-gas interface with respect to the solid. Usually, surfaces showing contact angle with water higher than 90 are considered hydrophobic and for contact angle lower than 90 degrees hydrophilic. Measurements were performed using an optical contact angle system (Drop shape analyzer DSA 30S, Krüss GmbH, Germany). The instrument software (SCA 20) provides information about the samples throughout the analysis of its image, while an algorithm based on the Young-Laplace equation, is used to correlate the drop shape with the surface tension and the contact angle. With this instrument is possible to measure the surface tension through the pendant drop method and the contact angle by using the sessile drop method. In the pendant drop method, a drop hangs by the top of a flat needle, while in the sessile drop method, a drop of a liquid is placed on a solid, plane and waterproof surface. In both cases the drop gets a shape that depends by its weight, density, surface tension and by the liquid affinity toward the surface. The drop profile is analysed by the high-performance video camera and processed by the software in order to obtain surface tension and contact angle.

2.4.8. X-ray Photoelectron Spectroscopy (XPS)

XPS analysis were performed at ICMATE-CNR (Padova) with a Perkin-Elmer Φ-5600-ci spectrometer using Mg Kα radiation. The sample analysis area was 800 µm in diameter. Survey scans were obtained in the 0−1100 eV range (187.8 eV pass energy, 0.8 eV $step^{-1}$, 0.05 s $step^{-1}$). Detailed scans were recorded for selected elements (23.5 eV pass energy, 0.1 eV $step^{-1}$, 0.1 s $step^{-1}$). The standard deviation for the Binding Energies (BEs) values is ± 0.2 eV. The BE shifts were corrected by assigning to the C1s peak associated with adventitious hydrocarbons a value of 284.8 eV. The atomic compositions were evaluated from peak areas using sensitivity factors supplied by Perkin-Elmer, taking into account the geometric configuration of the apparatus. The experimental uncertainty on the reported atomic composition values does not exceed ± 5%.

2.4.9. Photoluminescence (PL)

Luminescence spectra were recorded at ICMATE-CNR (Padova) with a Horiba JobinYvon *Fluorolog-3* spectrofluorimeter in a front-face acquisition geometry. The instrument is equipped with a double-grating monochromator in the excitation side and a Horiba iHR320 imaging spectrometer in emission sides coupled to a *R928P* Hamamatsu photomultiplier and Horiba Sincerity CCD detector. A 450 W Xe arc lamp was used as the excitation source. Emission spectra were corrected for detection and optical spectral response of the spectrofluorimeter supplied by the manufacturer. The excitation spectra were corrected for the spectral distribution of the lamp intensity using a photodiode reference detector. The luminescence lifetimes were measured with an experimental uncertainty of ±10 %, using a Horiba Nanoled (460 nm) as excitation source and elaborated with standard software fitting procedures. Absolute photoluminescence quantum yields (PLQY) were calculated from corrected emission spectra obtained with an apparatus consisting of a Spectralon coated integrating sphere accessory (4'', F-3018, Horiba Jobin Yvon), fitted in the fluorimeter sample chamber. For each compound, three independent measurements were carried out, with an estimated error of ±20 %.

2.4.10. Electrochemical characterization

Cyclic voltammetry, Linear sweep voltammetry, electrochemical impedance spectroscopy and Mott-Schottky analysis were carried out in a three-electrode cell, using the $CsPbBr_3$ as working electrodes, the Pt as counter electrode and the saturated calomel electrode (SCE) as reference electrode. The analyses were recorded using the potentiostat/galvanostat with impedance analyzer and an optical bench (PGSTAT 302N + FRA32M, Metrohm, Autolab).

2.4.10.1. Cyclic voltammetry (CV)

Cyclic Voltammetry is a technique able to measure the current produced in an electrochemical cell when an external voltage is applied. The potential applied changes during the time of analysis, from a greater potential to a lower one until the switching. The vertex potential is set in order to have the oxidation or the reduction of the species present in the electrolyte. Fig 2.2 shows the fluctuation of the potential as a function of time: during the reduction the potential increases with time, while during the oxidation, the potential decreases with the increase of the time. The curves could be recorded at different scan rates, which in Fig 2.2 is the slope of the graph.

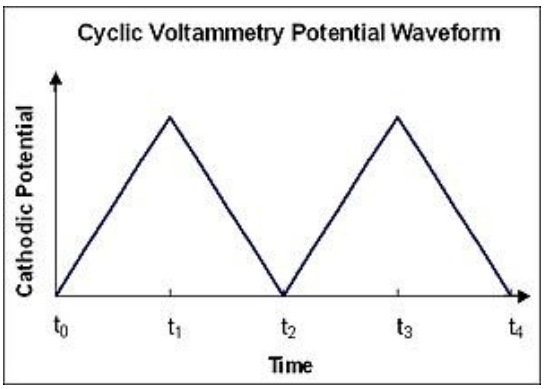

Fig 2.5: CV excitation signal

The current is measured by the working electrode during the scanning of the potentials, the graph is recorded in reduction from the starting potential to the first vertex potential, and in oxidation from the first vertex potential to the final potential. The

appeared peaks in reduction (cathodic peak I_{pc}) and oxidation (anodic peak I_{pa}) are related to the current produced during the reduction and oxidation respectively (Fig 2.3).

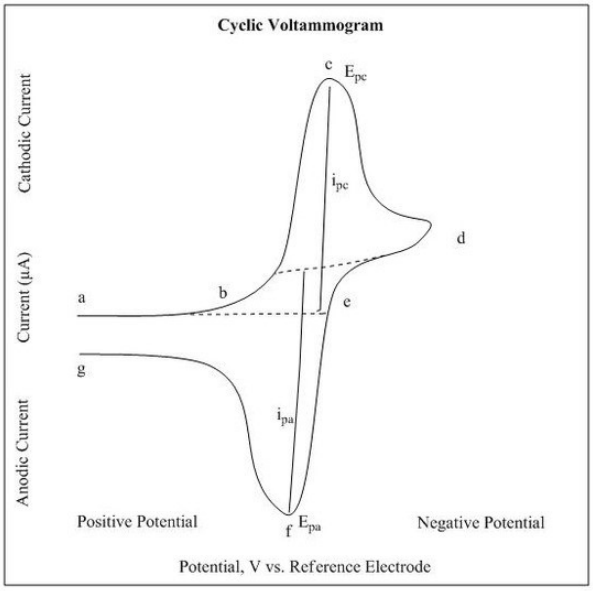

Fig 2.6: Voltammogram of a redox process.

CV were firstly performed in a three electrodes cell using $CsPbBr_3$ as working electrode, Pt as counter electrode, Saturated Calomel Electrode (SCE, KCl 3.5 M) as reference electrode and 1mM $K_3Fe(CN)_6$ (Sigma Aldrich, Germany) and $Ru(NH_3)_6Cl_3$ 1mM (Sigma Aldrich, Germany) both in KCl 0.1M (Sigma Aldrich, Germany) as electrolytes. The starting potential was 0 V, while the first and second vertex potentials were respectively +0.8V and -0.8V vs SCE. 6 scans at 100 mV s^{-1} were considered for each measurement. The three electrodes cell for the CV analyses was composed by FTO+$CsPbBr_3$/C or Pt films as working electrode (active area 1 cm^2), Saturated Calomel Electrode (SCE, KCl 3.5M) as a reference electrode and platinum foil as counter-electrode. They were done at 20 mV/s, from +0.8 V to -0.8 V vs SCE in $K_3Fe(CN)_6$ (Sigma Aldrich, Germany) 1 mM in KCl (Sigma Aldrich, Germany) 0.1 M as electrolyte. Each electrode was exposed to 30 scans.

2.4.10.2. Linear Sweep Voltammetry (LSV)

The Linear Sweep Voltammetry is able to measure the current when a range of potential is applied in an electrochemical cell. If the potential applied starts from a negative potential to a positive one, the current recorded is about an oxidation, on contrary if the potential applied starts from a positive value to a negative one, the reduction of the species into the electrolyte, occurs. LSV analysis were done in the same electrochemical cell in dark and under illumination in 0.1 M $KHCO_3$ (>98%, Sigma Aldrich, Germany) as electrolyte and under stirring. The potential was swept linearly at a scan rate of 20 mV s^{-1} between 0 and -1.5 V vs SCE. The LSV were carried out both under inert (N_2) or CO_2 saturated atmosphere (CO_2 99.998%, at flow rate of 1 L min^{-1}) purged before the test for 15 minutes into the cell.

2.4.10.3. Electrochemical Impedance Spectroscopy (EIS)

Electrochemical Impedance Spectroscopy EIS, measures an alternating current as a response of an alternating potential applied. The impedance (Z) is a circuit parameter very similar to the resistance (R) and it could be described as the resistance of the system to the charge current flux:

$$Z = \frac{V(t)}{I(t)} \qquad (2.6)$$

The impedance Z depends on the time and the frequency, the latter is generally applied from 100 KHz to 1mHz. The pseudo-linear response of a sinusoidal potential applied is a sinusoidal current with the same frequency but with shifted phase. Z is composed by a real part and an imaginary one, the real part represents the resistance of the electric circuits, while the imaginary part (reactance) is related to the other components of the system. The so-called Nyquist plot reports the impedance plotting the real part on the X-axis and the imaginary part on the Y-axis. For this thesis, EIS were done in dark conditions in the frequency range from 10^5 to $5x10^{-2}$ Hz with applied voltages of 0 V and -0.8 V and amplitude of 10 mV. The cell was filled with $LiClO_4$ (Sigma Aldrich, Germany)

0.1 M as electrolyte and a purging with N_2 was done for 15 minutes before the measurement.

2.4.10.4. Mott-Schottky

MS analysis were done in $LiClO_4$ 0.1M (Sigma Aldrich, Germany) (pH=6.3) as electrolyte in the range of potentials between +0.8 V and -0.8 V vs SCE (starting from the anodic potential), waiting 120 s before recording each spectrum. The range of frequency considered were between 10 KHz and 0.5 Hz with 10 mV amplitude of the AC signal. The solution was purged with N_2 for 20 minutes prior to start the analysis. The flat band potentials were determined graphically, interpolating the fitting of the linear part of the slope with the X axis.

2.4.10.5. Chronoamperometry

Chronoamperometry is a time-dependant technique where a square-wave potential is applied to the working electrode of the (photo)electrochemical cell. The current measured depends on the ionic diffusion of the electrolyte species from the bulk of the system to the surface of the electrode. For the thesis's purpose the current produced is used in the calculation of the faradic efficiency of the reaction's products. In fact, the integrating area of the curve reveal the amount of the electric charge (Q) produced during the CO_2 reduction, value presents at the denominator of the FE equation.

2.5. Photo-electrochemical tests (PEC)

A photoelectrochemical cell is composed by two compartments, the anodic and the cathodic one. The cathodic part was composed by the working electrodes ($CsPbBr_3$+C or $CsPbBr_3$+Pt) and the reference electrodes (Ag/AgCl) both immersed in a solution 0.1 M of $KHCO_3$ (>98%, Sigma Aldrich, Germany), the electrolyte. In the anodic part there was the counter electrode (platinum grid) immersed in a H_3SO_4 0.1 M (Sigma Aldrich,

Germany). The two compartments were separated by a Nafion membrane (Sigma Aldrich, 211). Once the PEC cell was assembled, the CO_2 is bubbled in the cathodic compartment for 30 minutes to saturate the $KHCO_3$ solution. The chronoamperometry was conducted at two different potentials (0.5 V and 0.8 V) for both the working electrodes for 3 hours. The working electrodes were illuminated by a solar simulator (LOT-QuantumDesign GmbH, Germany) during all the reaction time.

2.6. Chromatography

High-Performance Liquid Chromatography (HPLC) and Gas Chromatography (GC) were used to determine the nature of the products of the CO_2 photo-reduction.

HPLC was done using a Shimadzu USA MFG INC., Japan equipped with an UV-Vis detector (SPD-20A) and an injection loop of 20 µL. Two types of liquid products were considered: organic acids and carbonyl compounds (aldehydes and ketones). The two columns Supelcogel C-610H 30CMx7.8MM (Sigma Aldirich, Germany) and Supelcosil LC-18 5um 25cmx4.6mm (Sigma Aldrich, Germany) were used for the determination of the organic acids and aldehydes and ketones respectively. The methods for each column was optimized, starting from the method for the organic acid detection, using a solution of 0.1% H_3PO_4 (Sigma Aldrich, Germany) as mobile phase fluxed at 0.5 mL min^{-1}; the time of the analysis was set to 30 minutes. The methods were set using 3 standard solutions of formic and acetic acid, by dilution of concentrated stock solutions of 250 ppm to 10, 25 and 50 ppm. For the determination of aldehydes and ketones, the sample must be derivatized to be detectable with the UV-Vis detector. The samples were then treated at 40 °C for 1 hour with 300 µL of 2,4-dinitrophenylhydrazine phosphoric acid (Sigma Aldrich, Germany) 0.02 M and 200 µL of citrate buffer. The latter was prepared mixing 80 mL of citric acid (>99.5%, ACS reagent, Sigma Aldrich, Germany) 1M and 20 mL Sodium citrate (≥99%, FG, Sigma Aldrich, Germany) 1M and adjusting the pH to pH=3 with HCl or NaOH. After the derivatization the sample was injected in the column using acetonitrile (for HPLC, gradient grade, Sigma Aldrich, Germany) as eluent and successively a mixture of acetonitrile and water (for HPLC, Sigma Aldrich, Germany) in ratio 80:20 respectively. The eluent was fluxed at 1.5 mL min^{-1} for 15 minutes. The

method was used with standards containing formaldehyde-DNPH (Sigma Aldrich, Germany), acetaldehyde-DNPH (Sigma Aldrich, Germany) and acetone-DNPH (Sigma Aldrich, Germany) already derivatized. A solution of acetone (Sigma Aldrich, Germany) 0.79 ppm was then prepared and derivatized as aforementioned described.

The Gas products were analyzed injecting the gaseous samples using three channel columns (MS5A, 10m; PPu, 10m; 5CB, 4m) of a micro GC (990 Micro GC Agilent, USA). The instrument allows the detection of hydrogen, oxygen, nitrogen, argon, CO, CO_2, CH_4, propane, i-butane and n-butane. The GC was connected to the photoelectrochemical cell during all the reaction duration; the gases produced were sampled 10 times, every 18 minutes.

2.7. References

92. Bergamini, L., Sangiorgi, N., Gondolini, A. & Sanson, A. CsPbBr3 for photoelectrochemical cells. *Sol. Energy* **212**, 62–72 (2020).
93. Huang, H. *et al.* In situ growth of all-inorganic perovskite nanocrystals on black phosphorus nanosheets. *Chem. Commun.* **54**, 2365–2368 (2018).
94. Yu, K. *et al.* Visible light-driven photocatalytic degradation of rhodamine B over NaBiO3: Pathways and mechanism. *J. Phys. Chem. A* **113**, 10024–10032 (2009).
95. Yang, Y., Ajmal, S., Zheng, X. & Zhang, L. Efficient nanomaterials for harvesting clean fuels from electrochemical and photoelectrochemical CO 2 reduction. *Sustain. Energy Fuels* **2**, 510–537 (2018).
96. Gao, G. *et al.* Novel inorganic perovskite quantum dots for photocatalysis. *Nanoscale* **9**, 12032–12038 (2017).
97. Leijtens, T. *et al.* Stability of metal halide perovskite solar cells. *Adv. Energy Mater.* **5**, 1–23 (2015).
98. Liu, M. *et al.* Characteristics and mechanism of uranium photocatalytic removal enhanced by chelating hole scavenger citric acid in a TiO 2 suspension system. *J. Radioanal. Nucl. Chem.* **319**, 147–158 (2019).
99. Carnahan, R. D. & Hou, S. L. *Ink jet*. *IEEE Transations on Industry Applications* **13**, (1977).
100. Martin, G. D. & Hutchings, I. M. Fundamentals of Inkjet Technology. *Inkjet Technol. Digit. Fabr.* 21–44 (2012). doi:10.1002/9781118452943.ch2

Chapter 3

Results and Discussion

The aim of this thesis was to investigate Cesium Lead Bromide $CsPbBr_3$ (CPB) as potential material for the production of solar fuels. CPB is an all-inorganic halide perovskite widely investigated for its optoelectronic properties in the field of solar cells, light emitting diodes (LEDs) and photovoltaic applications. In this research, CPB was considered as material for the harvesting and generation of electric charges needed for the reduction of carbon dioxide in a photoelectrode of a photoelectrochemical cell (PEC).
The work started with the synthesis and characterizations of the powders, and their deposition in form of film to produce the photoelectrode. The photoelectrode was then fully characterized and then used to assemble a complete PEC and its test for the production of solar fuels.

3.1. $CsPbBr_3$ synthesis

In literature there are different synthesis methods that allow the production of particles of $CsPbBr_3$ with different dimension and shape. The first method tried in this work was the co-precipitation one[101].

3.1.1. Co-precipitation synthesis

The two starting precursors, $PbBr_2$ and CsBr were separately dissolved into hydrobromic acid (HBr) and then dropped in HBr kept under stirring. The $CsPbBr_3$ was immediately formed as precipitate. The brilliant orange powder was recovered by centrifugation and then washed with ethanol. The powder (CPB co-prec) obtained, was formed by monoclinic $CsPbBr_3$ (PDF#18-0364), as shown in the diffractogram of Fig 3.1.

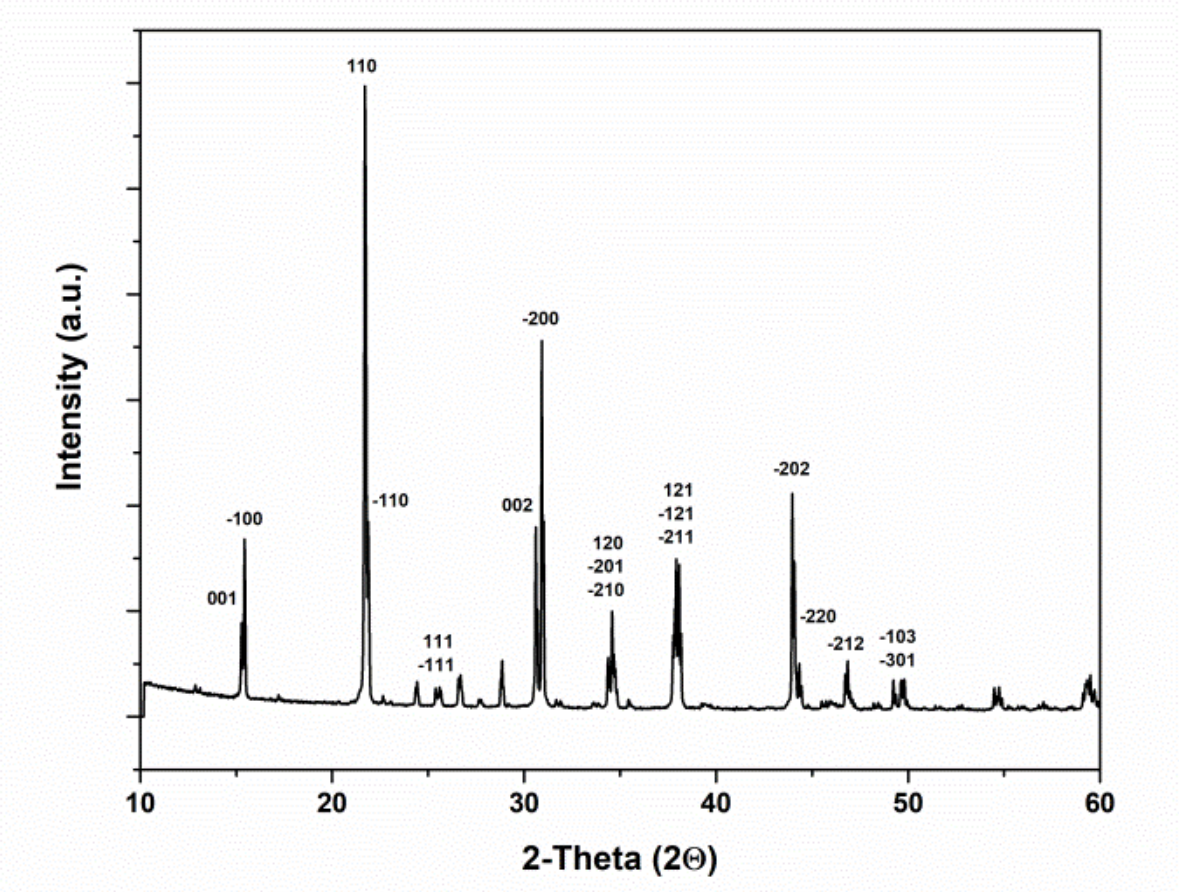

Fig 3.1: XRD of CPB co-prec.

The SEM images of Fig 3.2 show an inhomogeneous powder granulometry: bigger aggregates (≈ 20 µm) of $CsPbBr_3$ with sharp edges are mixed with smaller particles (≈ 5 µm).

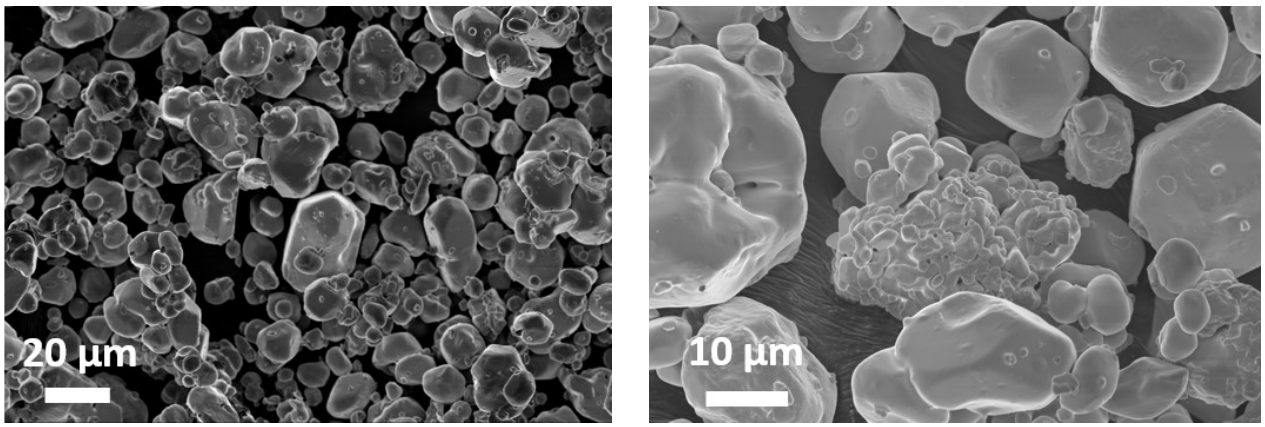

Fig 3.2: Micrographs of CPB co-prec.

The surface area determined by BET was found to be 0.95 m^2 g^{-1}, a low value for the catalytic application intended, the system was nevertheless considered for the photocatalytic study. The band gap of the sample was calculated through the reflectance spectra and elaborated by the Kubelka Munk theory and Tauc equation (Fig 3.3). The reflectance spectra (Fig 3.3a) was converted using the Kubelka Munk theory obtaining the graph shown in Fig 3.3b, where in the X-axis are reported the wavelength values, while in the Y-axis the absorbance values. The X-axis was converted from wavelength to the energy through the Planck's low:

$$E(eV) = h\nu = \frac{hc}{\lambda} = \frac{1239.7}{\lambda\ (nm)} \qquad (3.1)$$

while the Y-axis was elaborated multiplying its value with the values of the X-axis (energy – eV) to obtain a value of absorbance (αhν) and then elevated to the 1/n coefficient related to the electron transitions. "n" is considered equal to ½ if the transition is direct and allowed, 2 if is indirect and allowed, 3/2 if is direct and forbidden and 3 if the electron transition is indirect and forbidden. The n value for $CsPbBr_3$ was found to be ½[102] (direct and allowed transition) and therefore the value of the Eg equal to 2.26 eV.

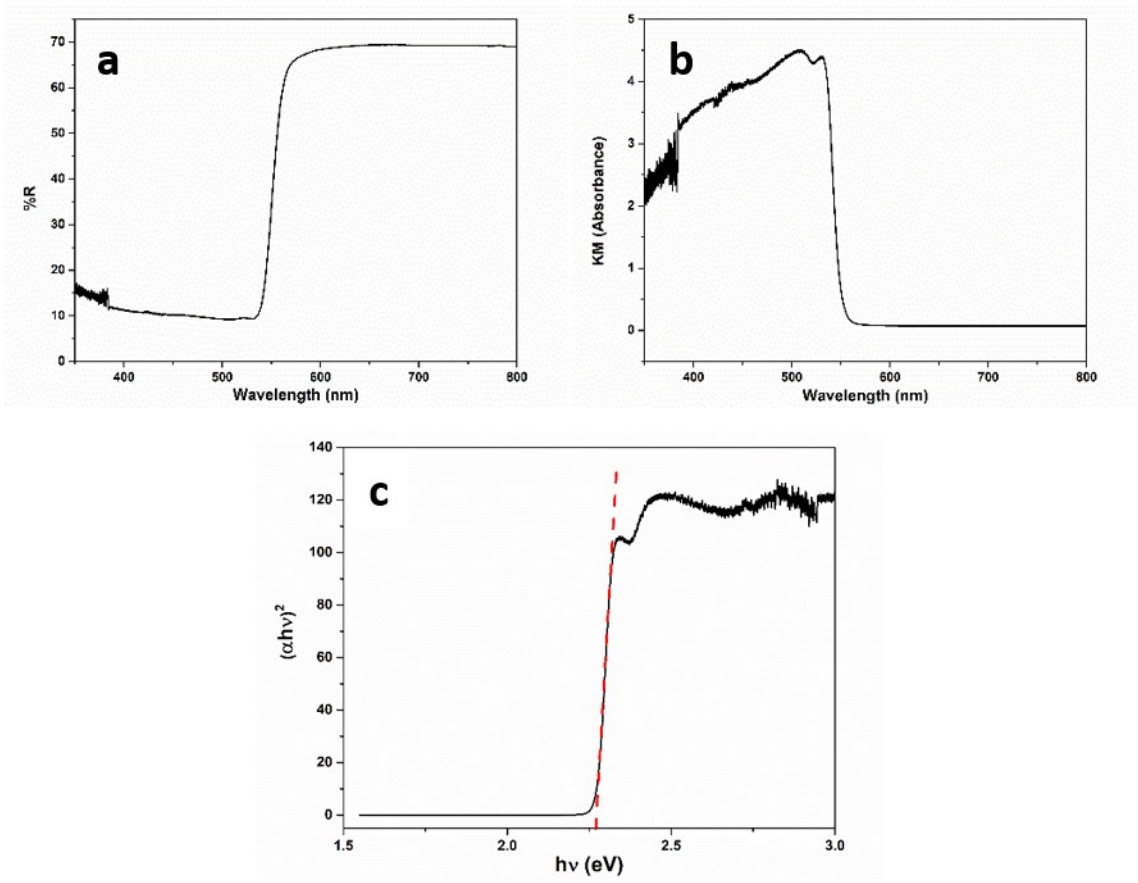

Fig 3.3: a) reflectance spectra of the CPB co-prec powder, b) related kubelka munk elaboration and c) band-gap graph extrapolation of CPB co-prec.

The results indicate that the material is able to effectively absorb photons in the visible part of the electromagnetic spectra and it is potentially suitable to be applied in PEC.

The results of the photocatalytic tests on the decomposition of rhodamine B (RhodB) and methyl orange (MO) are reported in Fig 3.4. The two molecules were chosen as target molecules, being the most common sample molecules for these tests. Their absorbance maximum is in the visible region (554 nm and 480 nm) and their degradation is easy to follow with UV-Visible spectrophotometer. The absorbance of the specific solution of RhodB or MO is reported as a function of time and as a ratio of the actual value versus the initial one. The same test was done also with the solution of RhodB and MO without powder as reference.

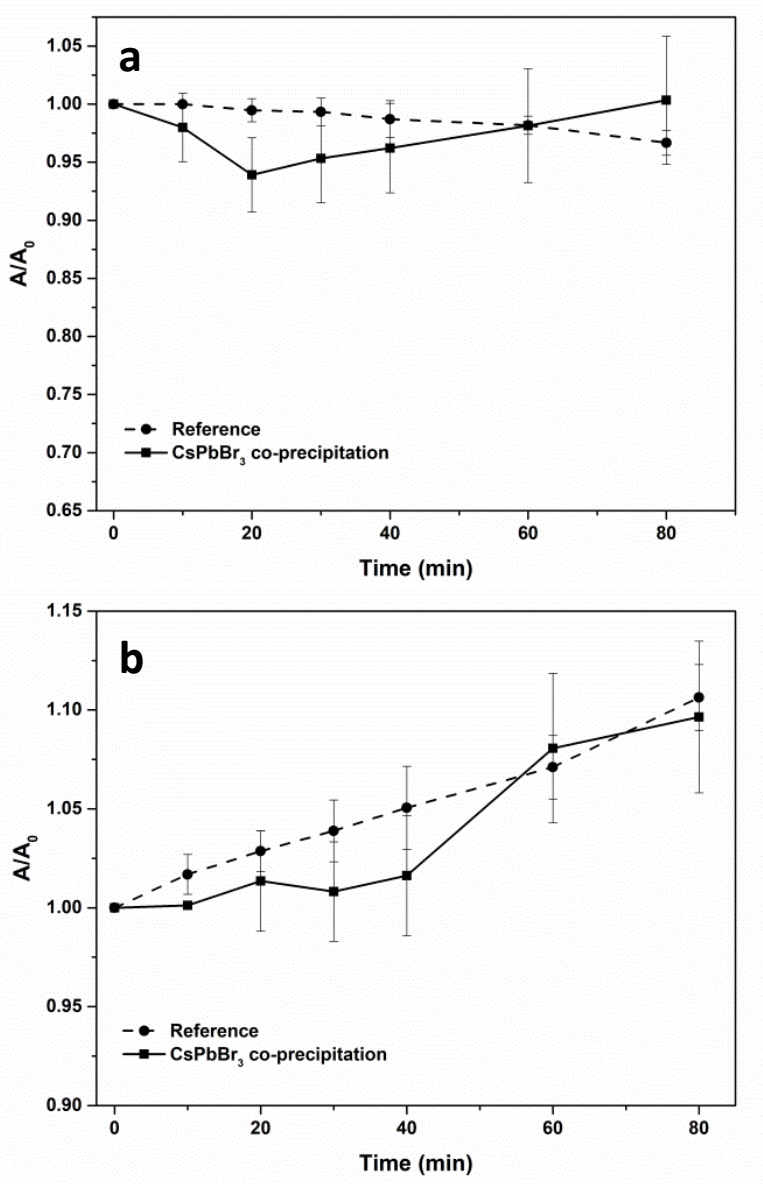

Fig 3.4: Photodegradation test of CPB co-prec carried out in a) RhodB and b) MO solution.

In both cases the trend of the lines was opposite of what expected, a photocatalytic material in fact should decompose the organic molecule with time (the fastest, the highest is the material activity). On the contrary the ratio A/A_0 increased with time after 20 minutes for RhodB and immediately with MO. These results were ascribed to problem of solubility as it will be better explained later on. Furthermore, for MO, the reference presents a non-conventional trend, an increase in the A/A_0 ratio also without the presence of catalyst, when irradiated. In literature the degradation of the azo compound is commonly followed by ESI-MS[103,104], this technique showed that under irradiation various degradations corresponding to the break of C-N bond of the

dimethylamino group and the substitution of the methyl groups with hydrogen ([-$N(CH_3)_2$] to [-NH_2]), or even the loss of the sulphate group are possible. The main bond cleavage is attributing to the azo group which brings to the formation of different species that are progressively forming compounds able to absorb the light in the same range of the parent compound. This is thought to be the case of the trend observed in Fig 3.4b.

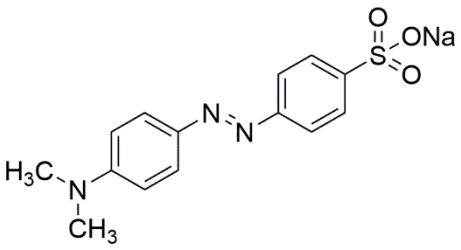

Fig 3.5: Chemical structure of MO molecule.

Coming back to the solubility issues, the perovskite synthesized was found to be soluble in water and therefore able to perform its catalytic activity for limited time, behaviour visible in Fig 3.4a, where after 20 minutes the ratio A/A_0 increase again. The powder loaded at the start of the test, was not present anymore at the end of it, indicating the dissolution of the particles in the aqueous solution. In order to overcome this problem, solubility tests were done suspending CPB co-prec in solvents of different polarity (Table 3.1).

Table 3.1: Polarity index of the solvent chosed for the solubility test.

Solvent	Polarity index
H_2O	9.0
THF	4.0
Acetone	5.1
Ethyl Acetate	4.4

The solubility was assessed visually looking at the change in the colour of the powder or at a visible decrease in the quantity in suspension; the results are reported in Table 3.2. The solubility tests were conducted for more than 80 minutes (duration of the photocatalytic tests) in order to test the stability of the materials for the times usually

used in the photoelectrochemical test in PEC cell. Among the possible solvents, acetone and tetrahydrofuran (THF) were chosen because they are soluble in water and this offer the possibility to investigate also mixtures, while ethyl acetate is immiscible with water, but it was considered as it is often used in photoelectrochemical cell to help the dissolution of CO_2 in the electrolyte.

Table 3.2: Solubility test of $CsPbBr_3$ co-prec in water, acetone, THF, ethyl acetate and heir mixture.

Time (h)	H_2O	THF	H_2O/THF (70:30)	H_2O/THF (30:70)	ACETONE	H_2O/AC (70:30)	H_2O/AC (30:70)	EtAc
0	dissolved	present	White precipitate	White precipitate	present	White precipitate	White precipitate	present
1	dissolved	present	White precipitate	White precipitate	present	White precipitate	White precipitate	present
3	dissolved	present	White precipitate	White precipitate	present	White precipitate	White precipitate	present
6	dissolved	present	White precipitate	White precipitate	present	White precipitate	White precipitate	present
20	dissolved	present	White precipitate	White precipitate	present	White precipitate	White precipitate	present

As seen in Table 3.2, the presence of low percentages of water, either with THF or acetone, dissolves or changes the crystals of CPB co-prec, which turn from a brilliant orange to a white precipitate. XRD analysis showed that the latter correspond to a different stoichiometry of lead halide perovskite: $CsPb_2Br_5$ (Fig 3.6). The stability of the powder was assured only in pure solvents (acetone, THF or EtAc). Among them, the choice fell on ethyl acetate for its ability of promoting the dissolution of CO_2 in aqueous solution and therefore helping the rate of conversion of carbon dioxide in PEC applications.

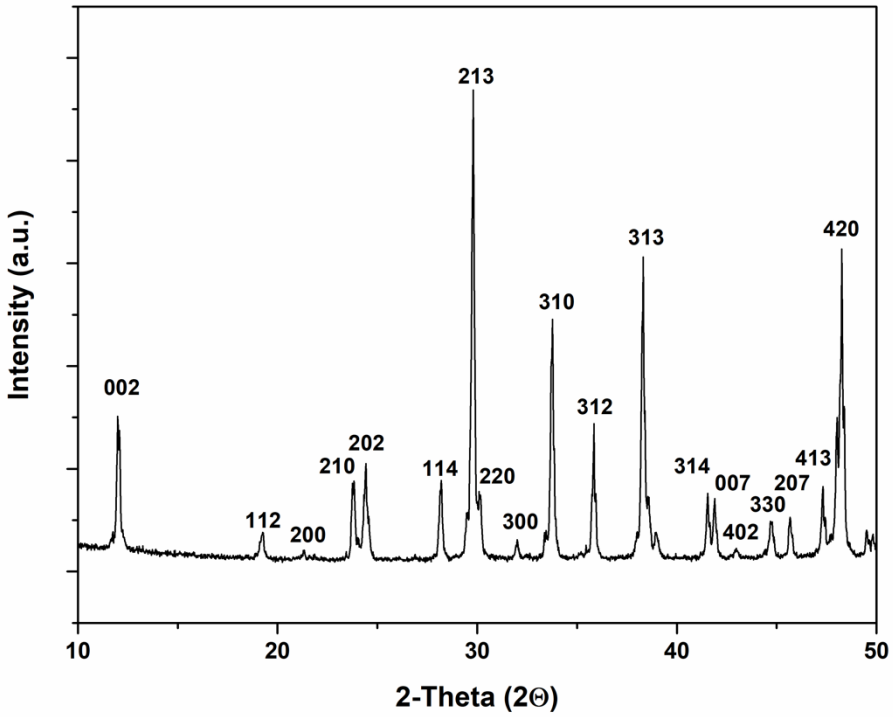

Fig 3.6: Diffractogram of the white precipitate $CsPb_2Br_5$ (PDF#25-0211) formed from $CsPbBr_3$ after 20 hours in contact with water and dried in oven at 100 °C.

Fig 3.7 reports the photocatalytic activity of CPB co-prec in a solution of MO and RhodB in EtAc obtained in the same conditions reported above. Fig 3.7a shows the good photodegradation of the CPB co-prec in the first 30 minutes (65-70 %), after this time the photodegradation stopped reaching a plateau. In this case replacing water with an organic solvent allowed stabilizing the $CsPbBr_3$. On the contrary, with the MO solution the degradation as discussed before, hindered a reliable assessment of the degradation activity of $CsPbBr_3$ towards these organic compounds.

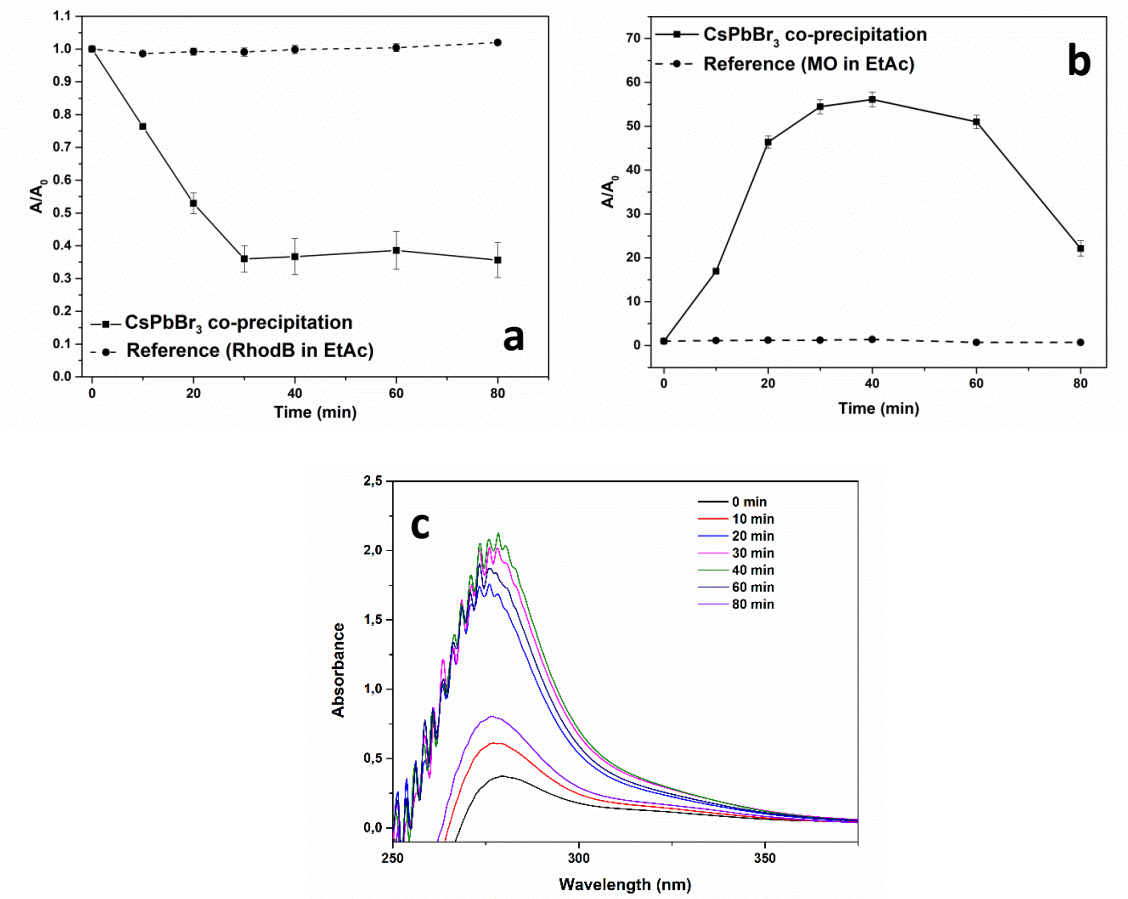

Fig 3.7: Photodegradation test of CPB co-prec carried out in a) RhodB solution in ethyl acetate, and b) MO solution in ethyl acetate and c) Absorbance spectra of MO solution in ethyl acetate.

As mentioned above, and as was found in literature[105], under irradiation MO undergoes several degradation phenomena. The cleavage of its bonds leads to the formation of compounds that are still able to absorb the light in the UV range at 279 nm. As a consequence, the decrease in absorbance due to the degradation of MO is counterbalanced (and overwhelmed) by the increase due to the degradation products. Those new peaks are responsible of the increase of the absorbance registered in the spectra reported in Fig 3.4. For this reason, the tests were no longer considered in the work. The powder obtained by co-precipitation even if showing some photocatalytic activity was found to have low surface area. Ascribing this to the synthesis condition, a new synthesis method (the oleate one) was then considered.

3.1.2. Oleate synthesis

This method is a one-step synthesis route were the precursor powders ($PbBr_2$ and Cs_2CO_3) are loaded in a flask together with the solvent, 1-octadecene and two capping ligands: oleic acid (OA) and oleylamine (OLA). The synthesis is carried out with conventional heating at 110 °C for 20 minutes, followed by washing and centrifugation of the suspension with acetone. The precipitate $CsPbBr_3$ (CPB-oleate) was then suspended with hexane.

To verify the effective formation of $CsPbBr_3$, the as-synthesized crystals were analyzed by XRD. The resulting spectrum (Fig 3.8) indicates the pure $CsPbBr_3$ monoclinic phase (PDF#18-0364), identified also previously (Fig 3.1) but with a considerably smaller dimension.

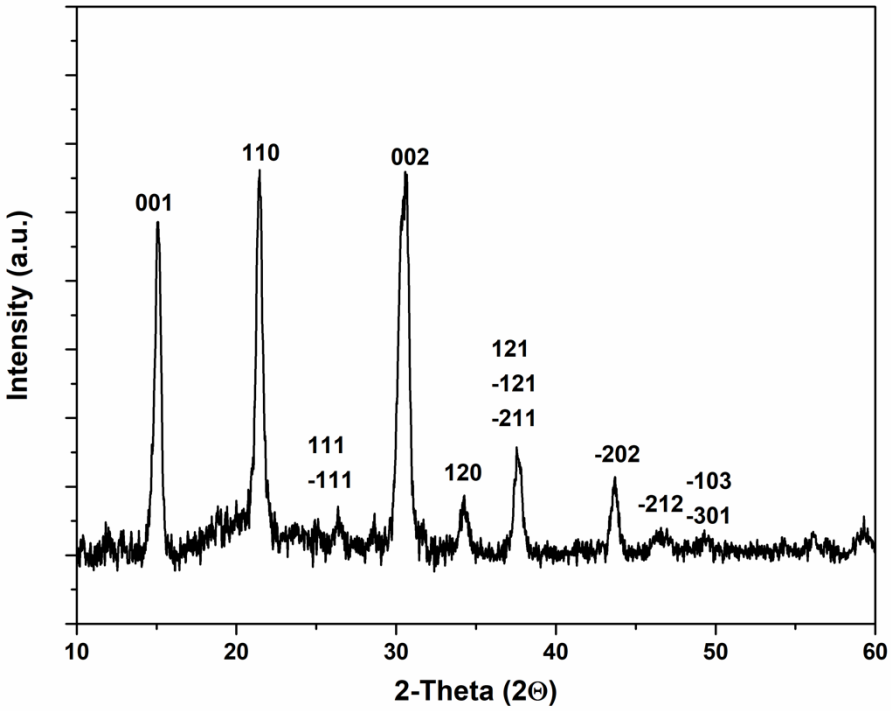

Fig 3.8: XRD patterns of the as-synthesized CPB-oleate (PDF#18-0364).

The SEM micrographs (Fig 3.9) shows particles with essentially round shape and an average particle size of 270 ± 80 nm.

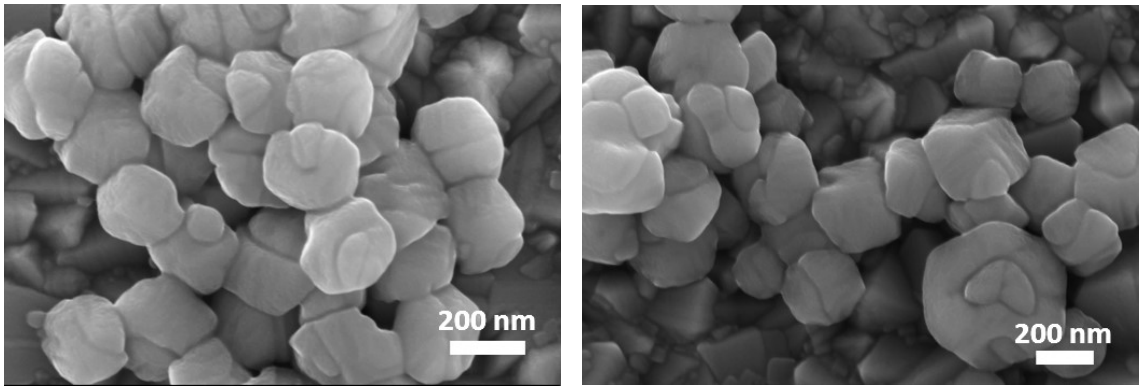

Fig 3.9: SEM micrograph of CPB-oleate.

The pure CPB-oleate phase was also confirmed by a strong absorption spectra in the visible region (530 nm)[106,107] as reported in Fig 3.10a that corresponds to a value of bandgap for this material of 2.34 eV, suitable for photoelectrochemical application (Fig 3.10b)[108]. The previous synthesis gave a value of band gap of 2.26 eV, lower than what were calculated for the oleate synthesis. This behavior can be mainly ascribed to the different dimensions of the powders: it is in fact well known that the band gap value tend to increase with an increasing of the particle dimension[109].

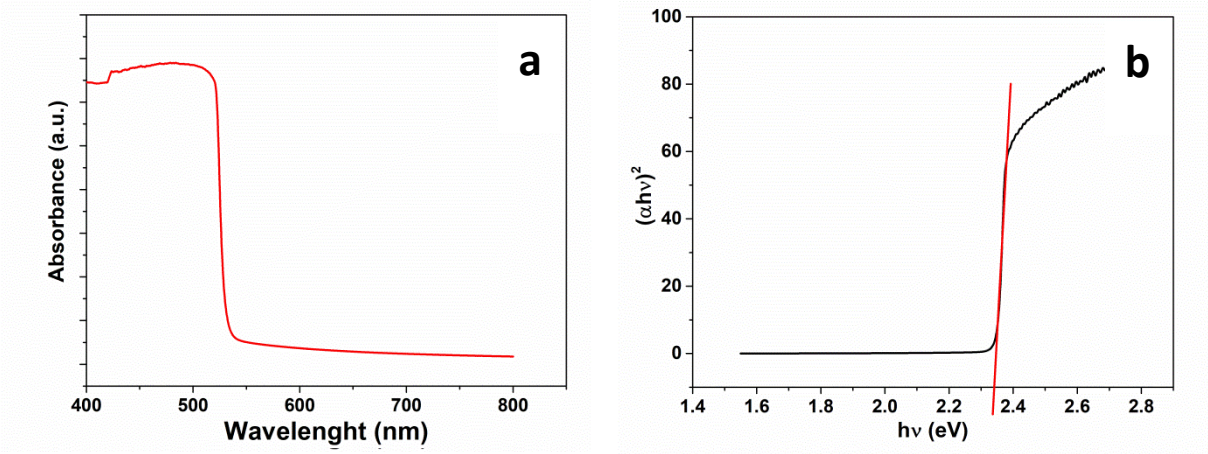

Fig 3.10: a) UV-Vis absorption spectra of CPB-oleate, and b) corresponding Tauc plot.

Considering the results obtained with the previous synthesis, stability test in different solvents were conducted also on the product of the oleate one. The suspension was left drying from the hexane (solvent) in a vacuum oven, and the remaining brilliant yellow powder at the bottom of the test tubes was suspended in the solvents listed in Table 3.3.

Table 3.3: solubility test of $CsPbBr_3$-susp in water, acetone, THF, ethyl acetate and heir mixture.

tempo (h)	H_2O	THF	H_2O/THF (70:30)	H_2O/THF (30:70)	ACETONE	H_2O/AC (70:30)	H_2O/AC (30:70)	EtAc
0	present	present	present	present	present	present	present	present
1	present	present	present	white solid	present	present	present	present
3	present	present	Present in smaller quantities	white solid	present	Present in smaller quantities	Present in smaller quantities	present
6	present	present	Present in smaller quantities	White solid	Present in smaller quantities	Present in smaller quantities	Present in smaller quantities	present
20	present	Orange	Present in smaller quantities and white	White solid	Present in smaller quantities	Present in smaller quantities	Present in smaller quantities and white	present

The CPB-oleate was generally more stable than what observed for the previous powders. In particular both in water and in ethyl acetate $CsPbBr_3$ did not change its colour and there were no dissolution processes readily observed. This improvement of stability is due to the organic molecules remaining from the capping ligands used during the synthesis that covering the powder surface increasing its stability hindering the leaching effect of water. The photocatalytic activity of CPB-oleate crystals was evaluated assessing the degradation rate of RhodB under light irradiation into two different reaction environments: water and ethyl acetate (Fig 3.11). The analysis was repeated with Rhodamine B only in both conditions as reference.

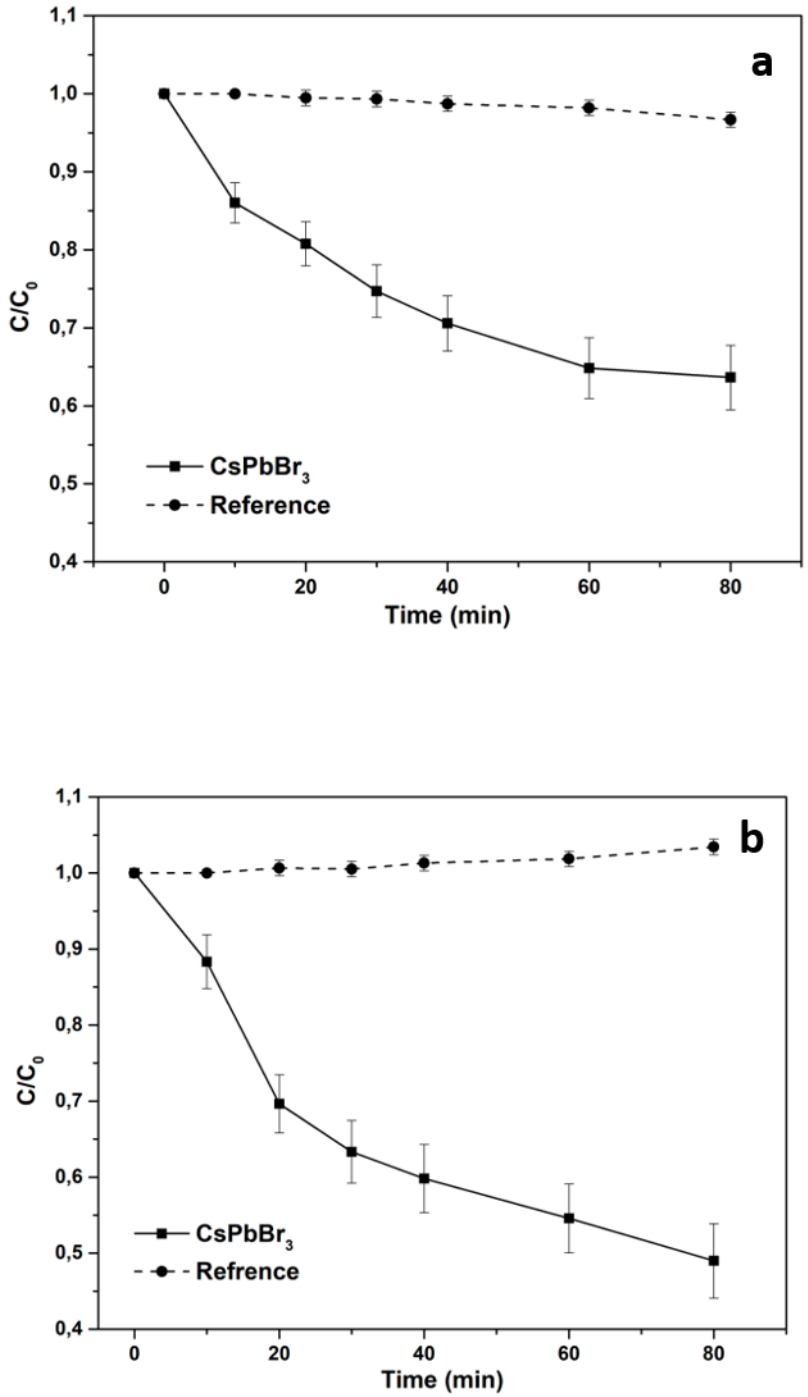

Fig 3.11: Photocatalytic tests of Rhodamine B degradation with CPB-oleate in a) water-based solution and b) ethyl acetate-based solution.

Fig 3.11 shows that the direct photolysis of Rhodamine B was negligible without photocatalyst, while CPB-oleate had the ability to degrade it in both the environments considered. In particular, the highest degradation rate (almost complete degradation after 80 minutes) was obtained using ethyl acetate, while only 70% degradation was reached for the same time in water. These results are probably consequence of two

different phenomena: the $CsPbBr_3$ stability in aqueous environment and the hole scavenger role exhibit by ethyl acetate. It is in fact, well known that in water-based systems, $CsPbBr_3$ tends to undergo a lead leaching effect that transform the material into Cs_4PbBr_6 [110]. As claimed above, the protective effect of the organic and capping ligands[111,112] (in particular oleate-based ones) used for the NCs particles synthesis used in this work, help to increase the stability toward water degradation up to 60 minutes, but after this time, the system starts to degrade leading to a mixture of $CsPbBr_3$ and the less active Cs_4PbBr_6. This assumption is confirmed by the change in slope of the curve of the system reported in Fig 3.11a. In ethyl acetate on the contrary, the system is stable and its photocatalytic activity is improved by the hole scavenger effect of the acetate that reduce the charge recombination[96,97]. The hole scavenger molecules have the characteristics to catch the holes photogenerated decreasing the probability of recombination of the charges during the photocatalysis, in this way the electrons are more available to carried out the reduction of the RhodB molecule.

3.1.3. Microwave (MW) synthesis

In order to check another possible way to produce $CsPbBr_3$, and its influence on its properties; the system was produced using MW heating, and $PbBr_2$ and Cs_2CO_3 as precursors (CPB-MW). The microwave assisted heating is of great interest in the powder synthesis for its ability of heating homogeneously the system, exploiting the dielectric properties of the molecules present in the reactor. In MW heating there is direct interaction between the microwave radiation and the materials, while in conventional heating systems; the heat is generated from electrical components and then transfer to the reagents. The MW reactor works thanks to an electrical field which interacts with the polar molecules of the reagents (Fig 3.12). The polar molecules are generally arranged in disorderly manner, but when an electric field is applied, the dipoles tend to align along the electric field direction.

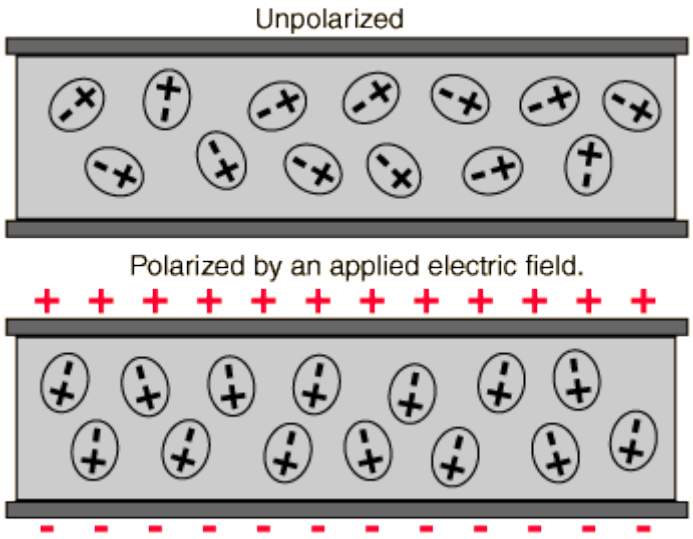

Fig 3.12: Polarization of dipoles in electric field.

The magnetrons present in the MW reactor continuously change the direction of the electric field leading to a continuous change of the orientation of the polar molecules inside the reactor. The agitation and friction due to the direction changes cause an intern and uniform heating. The microwave synthesis oven used allows tuning the heating ramp, the dwelling time as well as the power expressed in Watt (W) and the reaction temperature.

In the previous reaction methods, the principal solvent used was 1-Octadecene (ODE); this non-polar solvent is however not suitable for this synthesis as it lacks dipoles and therefore cannot be interact with the microwaves. It was therefore replaced with diethylene glycol mono butyl ether (DGBE) as polar solvent while a 1:1 mixture of oleic acid (OA) and oleylamine (OLA) was added as capping ligands to shape and to control the dimension of the particles[67]. Different tests were conducted to combine the right temperature and time necessary for the formation of the right stoichiometry.

The first synthesis test was conducted not replacing totally ODE but blending it with only a 10% of DGBE, the XRD diffractogram showed that the phase obtained was not pure $CsPbBr_3$, but some traces of rhombohedral Cs_4PbBr_6 were still clearly visible (Fig 3.13).

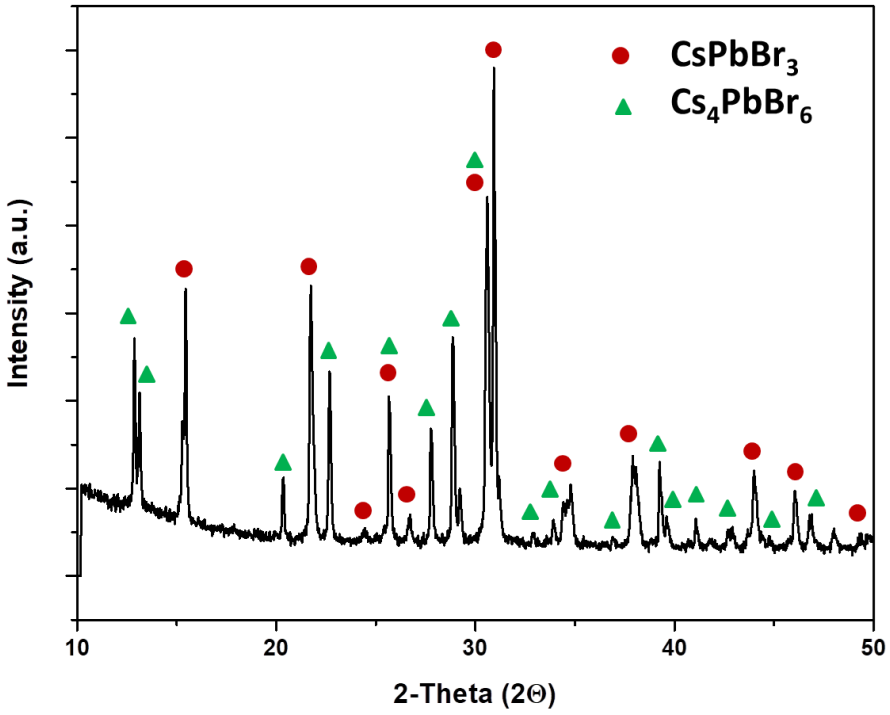

Fig 3.13: XRD of powder obtained with ODE:DGBE (9:1).

Having not reached the right composition of the perovskite but a mixture of different stoichiometries, a series of syntheses were done replacing completely the non-polar solvent with DGBE and varying temperature and time of reaction. The results are reported in Table 3.4.

Table 3.4: list of the reactions conducting with different time and temperatures.

TIME RAMP	REACTION TEMPERATURE	REACTION TIME	SOLVENT	PHASE
5 min	60°C	5 min	DGBE	Not present
5 min	80°C	5 min	DGBE	Present, not pure
5 min	110 °C	5 min	DGBE	Present, not pure
5 min	110° C	10 min	DGBE	Present, not pure
5 min	110°C	20 min	DGBE	Pure

The best conditions able to give a pure perovskite phase were 20 minutes at 110 °C; lower times or temperatures did not bring to the pure perovskite phase but a mixture of

stoichiometries as well as unreacted precursors as shown by the diffractograms of Fig 3.14.

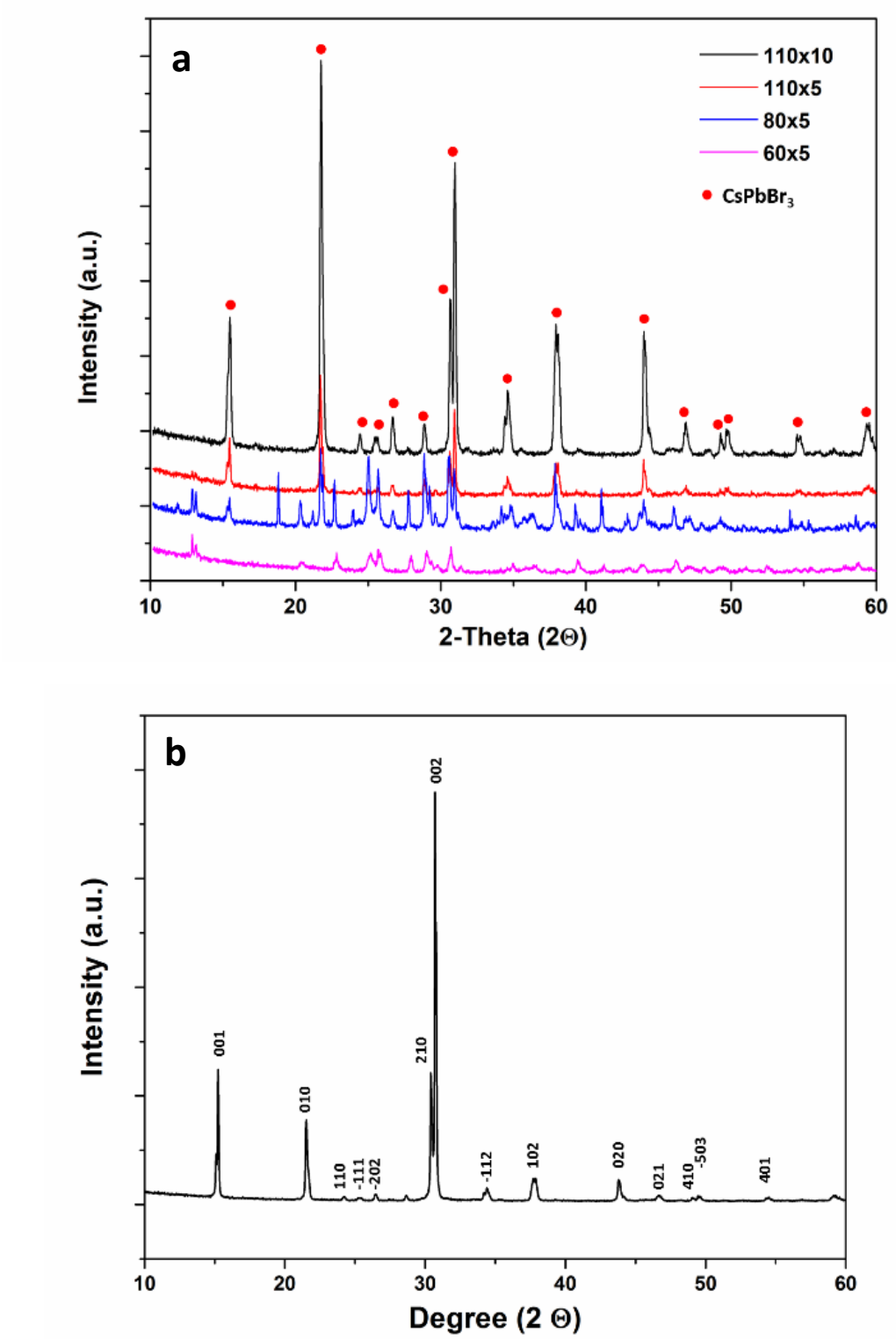

Fig 3.14: a) XRD spectra of the powders synthetized at different times and temperatures, and b) XRD peaks of the pure monoclinic MW-CPB phase achieved at 110 °C for 20 minutes.

In these conditions $CsPbBr_3$ was formed in monoclinic phase but a different from what previously found (PDF#54-0751 vs PDF#18-0364), Table 3.5.

Table 3.5: Crystallite dimension of the two monoclinic phases of $CsPbBr_3$ with different PDF cards.

Crystal parameters	PDF#18-0364	PDF#54-0751
Volume of the cell (10^6 pm^3)	200.02	235.22
a (Å)	5.827	9.843
b (Å)	5.827	4.127
c (Å)	5.891	6.874

Furthermore, the peaks are better defined in comparison with the XRD peaks of the particles resulting from the oleate synthesis. SEM micrographs (Fig 3.15) showed particles with sharp edges and not uniform shape and dimensions. In particular, the micrographs showed bigger particles with small ones that seem to grow on the surface of the bigger ones. These differences are thought to be due to the role of the capping agents that promote the heating on specific crystallographic phases and therefore influence the morphology of the final powders.

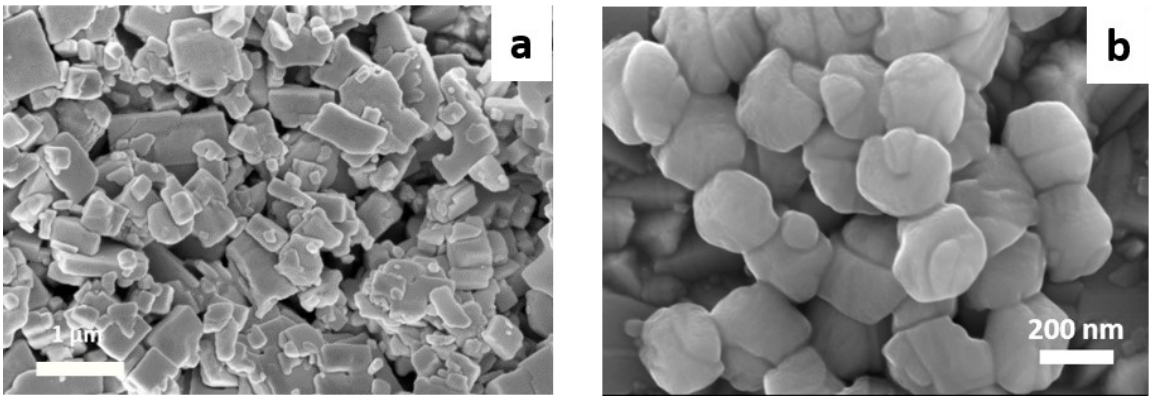

Fig 3.15: Morphology of a) the MW-CPB and b) CPB-oleate.

After having optimized the synthesis conditions, the pure CPB-MW powders were tested for its photocatalytic activity. The absorption and consequently the concentration of the organic dye did not decrease even after 80 minutes of light radiation (Fig 3.16), moreover at the end of the photocatalytic test the amount of $CsPbBr_3$ powder in the reactor was less than the loaded one, i.e. it was dissolved in the aqueous rhodamine B solution.

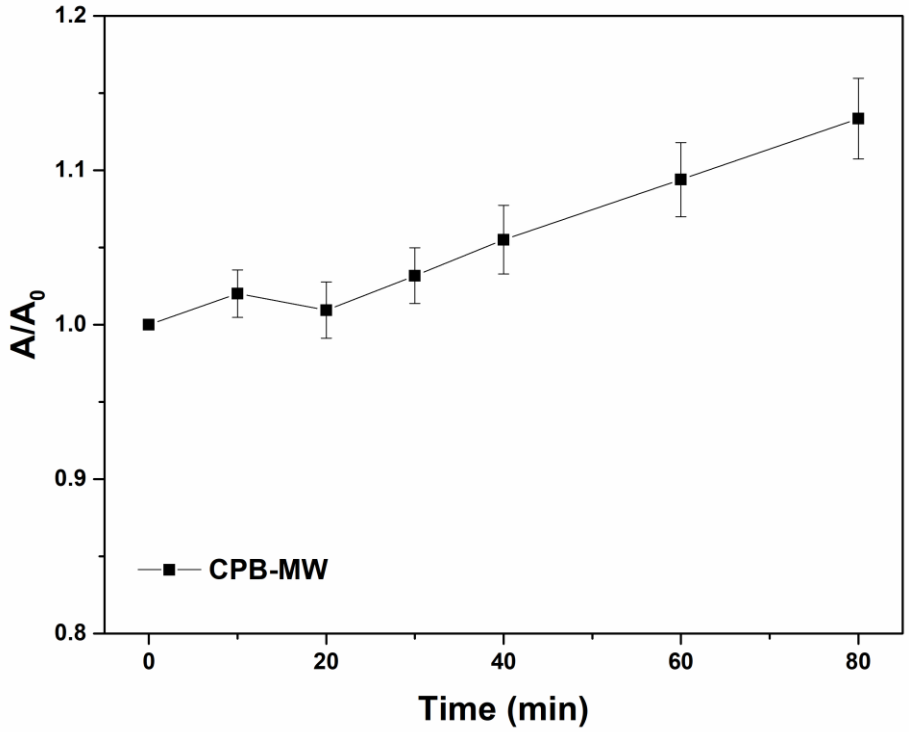

Fig 3.16: Photocatalytic test of the MW-$CsPbBr_3$.

A deeper study of the literature[113,114] indicates the importance of factors as polarity of the species, activation energies or enthalpies on the reaction path. These effects are included in the Arrhenius law:

$$k = Ae^{\left(\frac{-E_a}{RT}\right)} \qquad (3.2)$$

where K is the reaction speed constant, A is the pre-exponential factor, E_a is the activation energy, T is the temperature and R is the universal gas constant.

The electrical parts of the microwave reactor induced the orientation of dipolar molecules changing the pre-exponential A in the equation. Pre-exponential factor A represents, in fact, the collision between the molecules with the right geometric orientation. The presence of polar solvents is fundamental in microwave assisted reactions; besides this the reaction can be successfully carried out in non-polar solvents if ionic liquids or other molecules with high MW radiation absorption are added. For this reason, the next step was repeating the synthesis using as solvent 1-octadecene and modifying the ratio between the solvents and precursor powders. The precursors are in

fact good absorbing molecules and hence allow the microwave heating also in non-polar conditions. Also temperature, energy and time of the ramp heating were adjusted with the new synthesis. In this kind of synthesis in fact, if the conditions are not able to assure enough dipole alignment, and therefore heating of the system, the instrumentation automatically stopped the process. The same happens if the reaction vessel is not able to follow the heating ramp set. Table 3.6 summarizes the different conditions tested. Only the last conditions were able to assure a complete heating cycle. As mentioned before, another important factor that can affect the synthesis results is the amount of precursors considered.

Table 3.6: Different condition of synthesis in microwave reactor.

T_{ramp} (°C)	t_{ramp} (min)	E_{ramp} (W)	T_{dwell} (°C)	t_{dwell} (min)	E_{dwell} (W)	Phase formation
60	5	300	60	20	100	NO
110	5	300	110	20	100	NO
110	10	300	110	20	100	NO
110	10	350	110	20	200	OK

The first attempt was done considering literature[115], the tests were carried out keeping constant the solvent and the reagent concentration and changing the time of reaction (Table 3.7).

Table 3.7: Synthesis MW tests with different reaction time.

	T_{dwell} (°C)	t_{dwell} (min)	E_{dwell} (W)	Concentration $PbBr_2$ (mM)	Concentration Cs_2CO_3 (mM)	Total Volume (mL)
MW5	110	5	200	0.38	0.05	22
MW4	110	10	200	0.38	0.05	22
MW3	110	15	200	0.38	0.05	22
MW2	110	20	200	0.38	0.05	22

For all the systems the few peaks identified were referred to the monoclinic phase of $CsPbBr_3$ (PDF#18-0364). The peak broadening clearly present in the diffractograms are related to the nanometric nature of the powders as seen by the micrographs of Fig 3.18,

while the amorphous peak at around 20° 2θ, was probably due to the crystallization of the organic capping ligands remained from the synthesis.

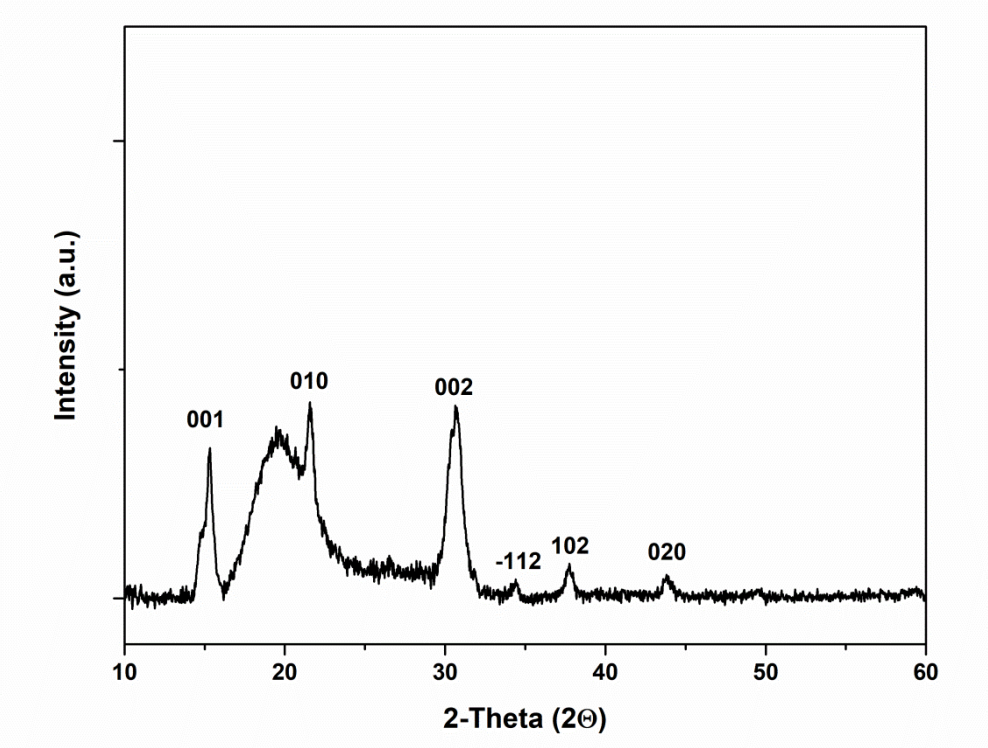

Fig 3.17: XRD results of $CsPbBr_3$ synthesized in MW reactor, MW_5.

The SEM images reported in Fig 3.18, showed the low dimension of the particles synthetized by microwave reaction at 5 minutes. The particles deriving from the MW_5, were used as the material for the construction of photoelectrode. This synthesis was chosen among all because after only 5 minutes of reactions the $CsPbBr_3$ was achieved.

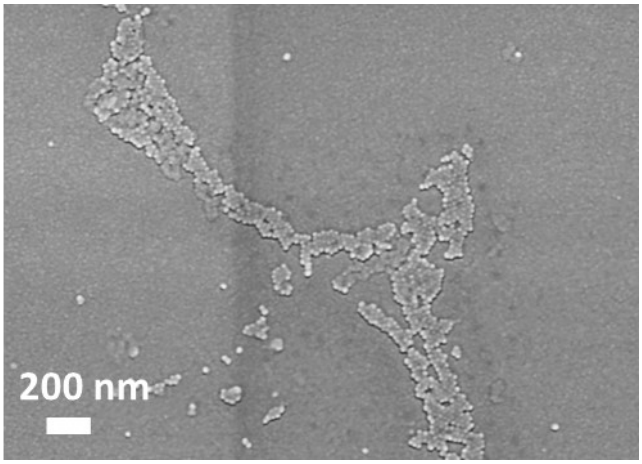

Fig 3.18: SEM images of products relative to the MW5 synthesis.

MW synthesis and oleate one, are conducted maintaining the ratio between the main solvent (1-octadecene) and the capping ligand the same (5:1), this allow us to compare the two synthesis route, with MW heating is used also a non-thermal components related to the Arrhenius law as aforementioned. Both the syntheses are carried out at 110 °C, so the thermal effect could be compared but the non-thermal effect of microwave heating allow to obtain comparable dimension of the pure crystals (Fig 3.18) but in less time of reaction.

3.2. $CsPbBr_3$ deposition methods

In order to obtain a photoelectrode to be used in PEC, the produced powder has to be deposited on a conductive substrate. Different methods of deposition were tried in order to define the best film in terms of homogeneity and performances during the electrochemical and photoelectrochemical tests.

3.2.1. Drop by drop deposition

The oleate synthesis was able to give a stable suspension of $CsPbBr_3$, suitable to be deposited by the simple drop by drop method as it stands onto a Fluorine doped Tin Oxide (FTO). TG/DSC analysis was performed to determine the thermal stability of the film obtained. The analysis reported in Figure 3.19 shows two weight losses: one around 50 °C and one just before 200 °C. The first was attributed to the solvent evaporation while the second one to the $CsPbBr_3$ thermal transformation/degradation to Cs_4PbBr_6[106]. The organics used during the synthesis (oleic acid, oleylamine and 1-octadecene) have boiling temperature higher than 300 °C, (respectively 360 °C, 364 °C and 315 °C) for this reason no degradation signs was found in the TG/DSC.

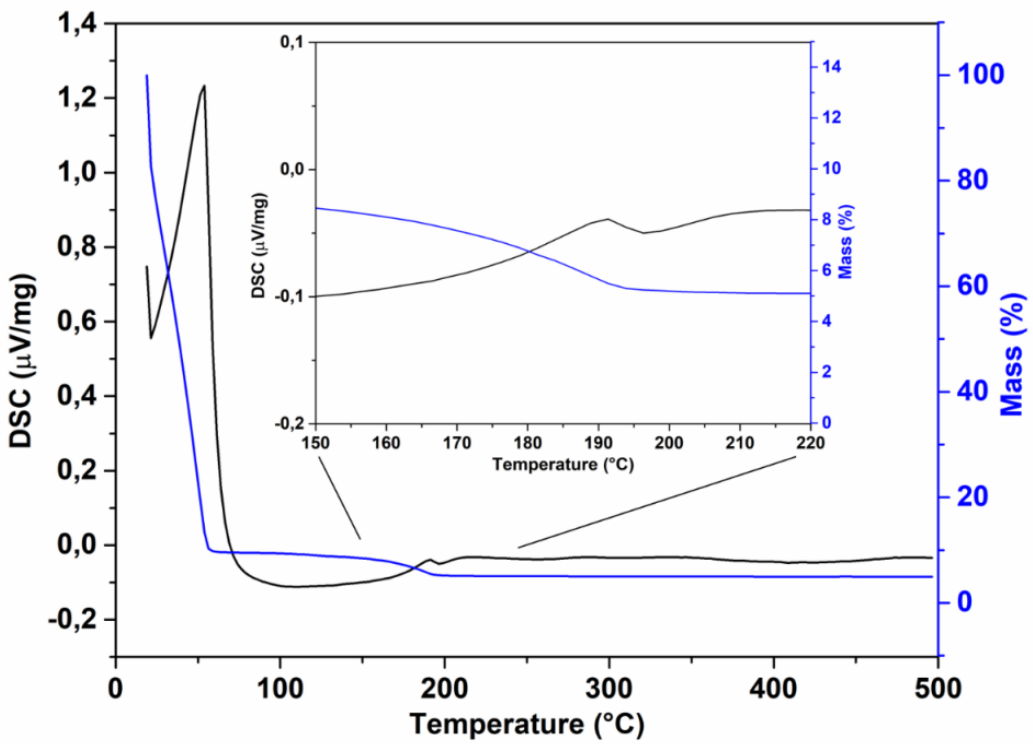

Fig 3.19: TG/DSC analysis obtained in air from 10 °C to 500 °C.

The temperature of the hot-plate was chosen on the basis of the TG/DSC information and the boiling point of the solvent used for the suspension. As the boiling point of hexane is 68 °C, the temperature of the hot plate was set at 100 °C, to let the evaporation of the hexane and the condensation of $CsPbBr_3$ on the FTO glass. The temperature after deposition could be set at 100 °C avoiding the decomposition of the perovskite but still ensuring the solvent evaporation.

For the photoanode production, the area of the FTO-glass was limited with a kapton mask to 1 cm^2 and covered dropping 20 µL of $CsPbBr_3$ suspended in hexane with a pipette. Two set of sample were considered: one repeating the deposition twice (2-dep) and the other one depositing the suspension five times (5-dep). 2 minutes of evaporation time was considered after each deposition. The EDX analyses on both set of films are reported in Fig 3.20. The spectra are example of the different samples obtained.

2-dep film **$Cs_{1.02}Pb_{0.88}Br_{3.24}$** 5-dep film **$CsPb_{0.85}Br_{3.08}$**

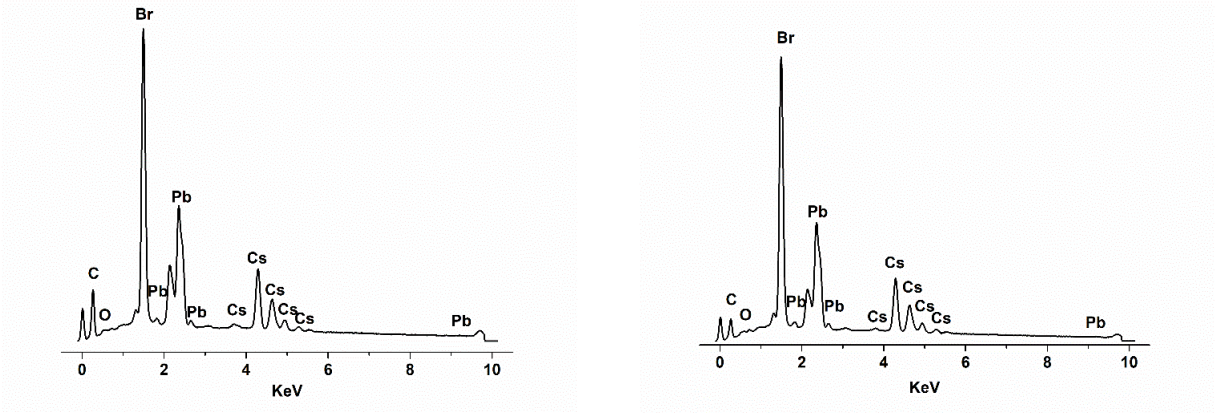

Fig 3.20: EDX spectra of the element present in the 2dep film and 5 dep film.

The elements of the perovskite are present in all the samples, the atomic percentage were elaborated and compared with the theoretical stoichiometry 1:1:3 as Cs:Pb:Br. For the 2-dep film the resulting composition is $Cs_{1.02}Pb_{0.88}Br_{3.24}$, while for the 5-dep film $CsPb_{0.85}Br_{3.08}$. In general the ratio were consistance with the stoichiometry of the perovskite but for both the samples, Pb was present slightly in defect in comparison with Cs.

The SEM micrographs of Fig 3.21, show the round particles of perovskite surrounded by the organic part still present in the suspension after deposition. The temperature used for drying the film is in fact not enough to eliminate the oleate part that remains in the film capping the particles.

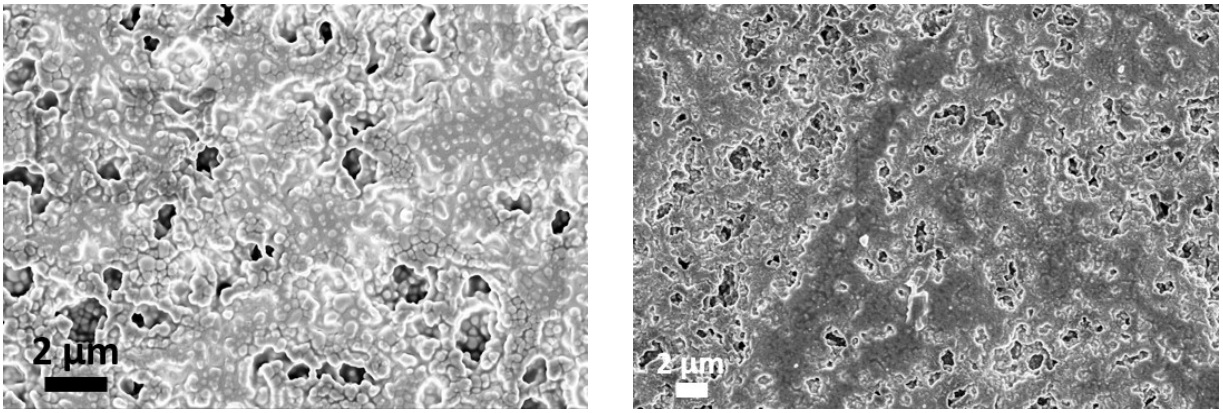

Fig 3.21: SEM images of $CsPbBr_3$ deposited with drop by drop method on the FTO substrate.

The thickness of the samples were measured by the 3D optical microscope, and the regarding the 2-dep film, the thickness was found to be 1.53±2.02 µm. The high variability of this value is ascribed by the low homogeneity of the deposited film, that was characterized by the typical "coffee-stain" phenomenon (Fig 3.22). This effect consist in the accumulation of the material on the edge of the stain dropped as a consequence of the solvent drying. The evaporation of the liquid starts from the edges of the drop, the solvent rapidly evaporated is replaced by the interior liquid of the drop, leading to the accumulation of the powders at the edges of the drop. On the other hand the 5-dep film thickness was found to be 2.00±0.43 µm, confirming the better homogeneity of the film. In the film obtained with 2-dep can be clearly seen the so call coffee-stain. The transmission spectra of the samples are reported in Fig 3.22.

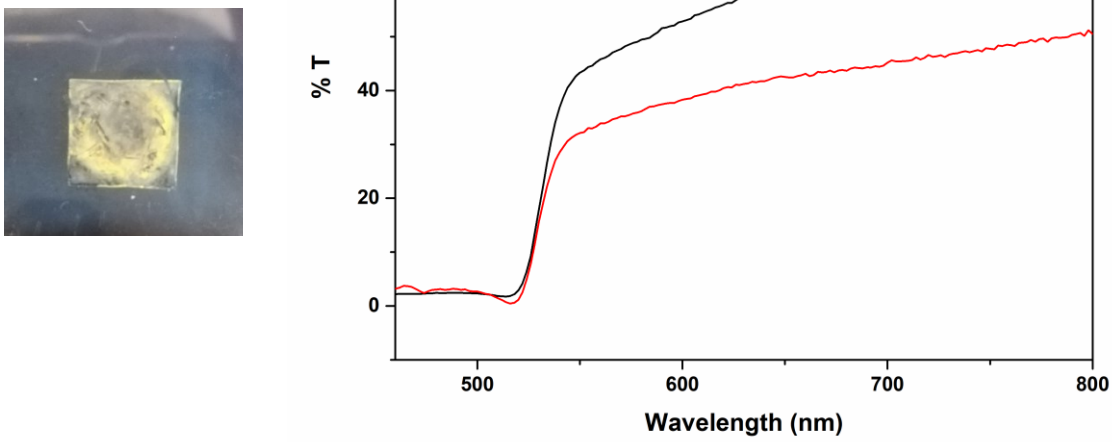

Fig 3.22: Transmission analysis of the 2 dep and 5 dep CPB-oleate films.

As expected, the absorption, and hence the transparency, of the 2-dep film is higher than the 5-dep film, confirming the different films thickness (and homogeneity). The 5-dep sample in particular, as a consequence of an improved quality of the surface shows higher transmittance in all the wavelength considered. This sample was therefore considered for the following activities.

The XRD spectra (Fig 3.23) confirms the presence of the $CsPbBr_3$ in monoclinic phase, (PDF#18-0364)[102]. Even if the diffractogram differs from the one obtained for the powder in suspension, the phase remains the monoclinic one. The baking temperature (100°C) of film is thought to be the cause of this slightly change. The change, as confirmed by the PDF cards, between the crystals and the film, is related to the dimension of the elementary cell: both the phases are monoclinic, but the dimensions are different and reported in Table 3.8:

Table 3.8: Crystallite dimension relatives to the two monoclinic phases of $CsPbBr_3$ with different PDF cards.

Crystal parameters	PDF#18-0364	PDF#54-0751
Volume of cell (10^6 pm^3)	200.02	235.22
a (Å)	5.827	9.843
b (Å)	5.827	4.127
c (Å)	5.891	6.874

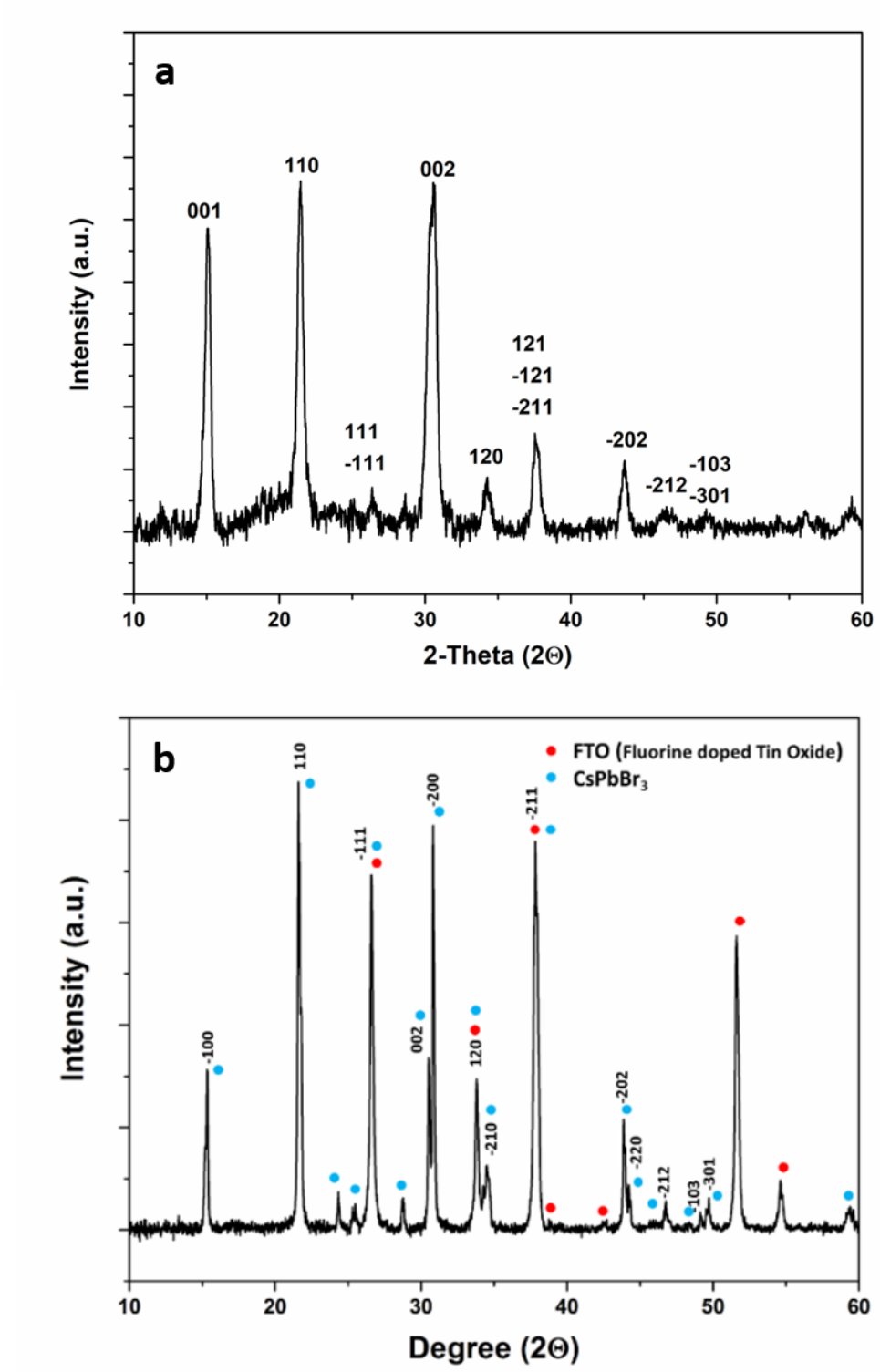

Fig 3.23: XRD analyses of a) $CsPbBr_3$ suspension and b) $CsPbBr_3$ thin film (PDF#54-0751) and FTO substrate (PDF#46-1090).

The surface of the crystals was analyzed by photoluminescence and X-ray photoelectron spectroscopy (XPS). The photoluminescense measurment was carried out with a wavelength of ecxitation of 390 nm.

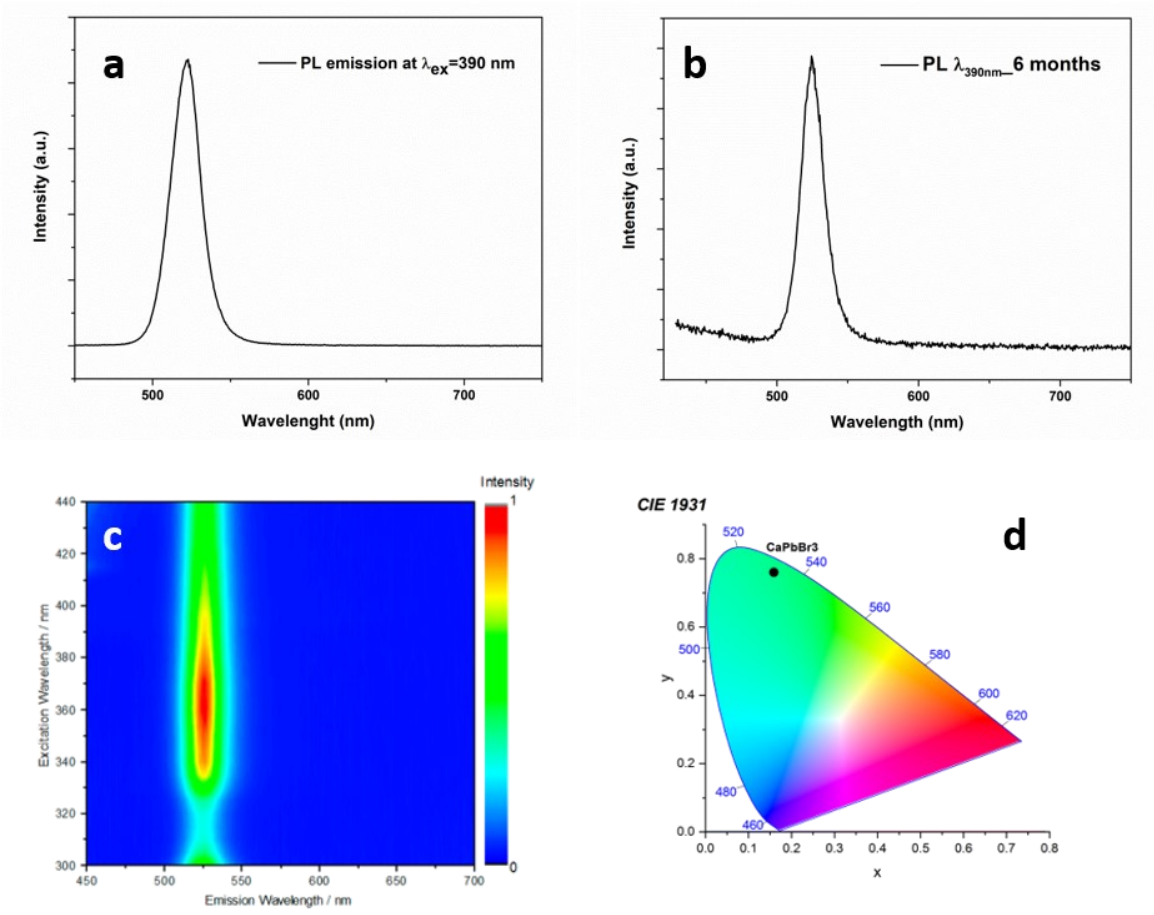

Fig 3.24: PL emission of a) $CsPbBr_3$ film b) $CsPbBr_3$ measured after 6 mounths of storage at room ambient c) and d) related CIE colorimetry position of $CsPbBr_3$.

The analysis showed in the green region (Fig 3.24) intense peak of emission at 521 nm. The same analysis was recorded after 6 months on the sample stored at ambient conditions without particular cautions regarding humidity and temperature, showed comparable results (Fig 3.24b). The PL spectrum shows a slight shift of the main peak (3 nm, from 521 nm to 524 nm), no significant differences on the film were present after 6 months, indicating the good stability of the perovskite in atmosphere conditions.

XPS measurements (Fig 3.25) shows the peaks relative to the perovkites at low energies. The three components clearly visible on the spectrum, Cs 4d, Pb 4f, Br 3p and Br 3d, the O 1s and C 1s peaks are probabily related to the chemiabsorbed OA and OLA species used during the synthesis as capping ligands[116]. The peaks relative to the Si 2s and Si 2p comes from the silicon bath used or related to the glass substrate (FTO), in all cases they could be considered contaminations.

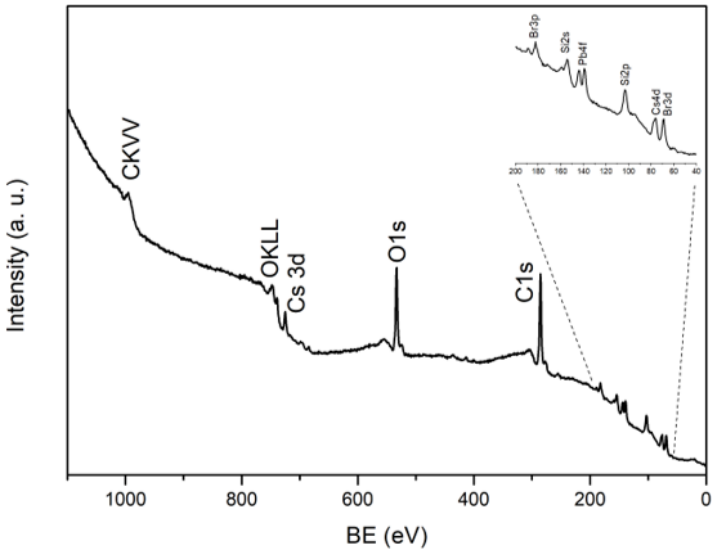

Fig 3.25: XPS of the $CsPbBr_3$ oleate film.

In Fig 3.26 the comparison between the band gap calculated for the film and for the as produced powder is reported. The two values are similar (2.32 eV and 2.34 eV) whereas the difference in the curves are consequence of the different amount of material available for the measurements.

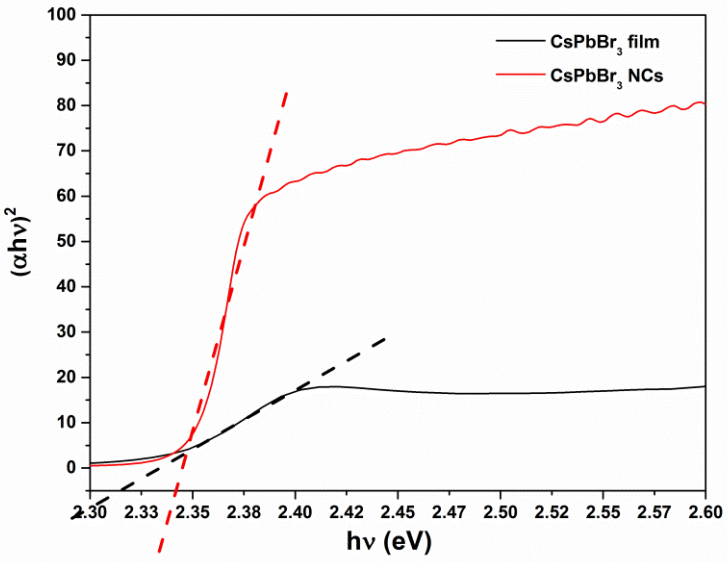

Fig 3.26: Tauc plot of $CsPbBr_3$-suspension and $CsPbBr_3$ thin film for band-gap calculation.

3.2.2. Spin coating deposition

Starting from literature data[117], where the synthesis and formation of the $CsPbBr_3$ directly on the surface of the FTO glass depositing each precursor dissolved in the right solvents and then deposited with the spin coater is reported, the hexane suspension of $CsPbBr_3$ as previous synthesized were spin coated on the FTO surface. This technique was considered in order to achieve an higher level of homogeneity of the film. Two sets of samples were prepared, one repeating the deposition 10 times and the other one 20 times. Between each deposition the electrode was baked on a hot plate at 100 °C for evaporating the solvent. As for the drop by drop deposition, the FTO was protected with a Kapton mask and only 1 cm^2 was left uncovered for the deposition. Each deposition was carried out with 20 µL of suspension with a rotation speed of 500 rpm for 40 seconds. The optical transmission analysis was conducted to understand the absorption related to the deposition.

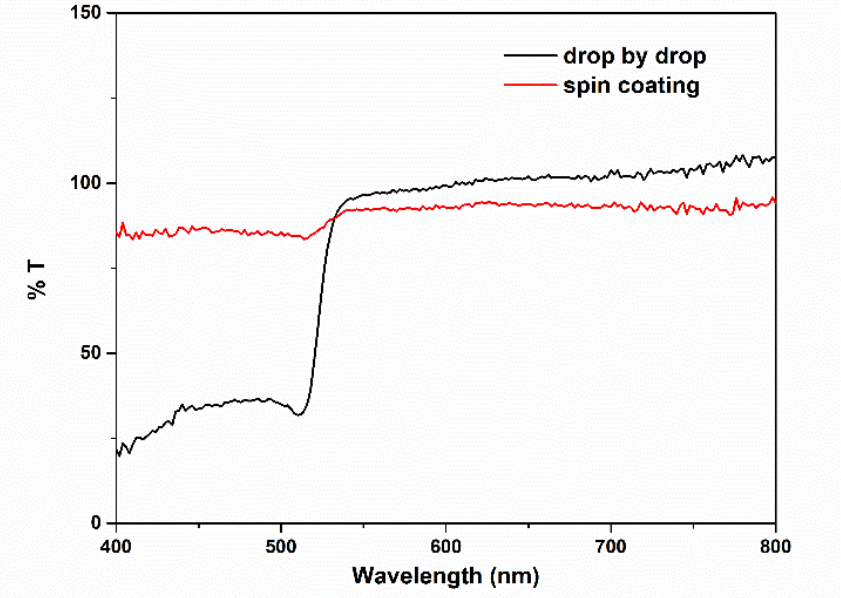

Fig 3.27: Transmission analysis of the $CsPbBr_3$ deposited by drop by drop and spin coater.

Fig 3.27 shows the transmission spectra of the films produced with the two different methods. For the spin coated film, the absorption was not as intense as expected. This behavior was ascribed by the small amount of material deposited by spin coating in comparison with the drop-by-drop method. In literature two solvents are commonly

used to process $CsPbBr_3$: hexane and toluene. These two solvents present very different behavior in terms of density, viscosity, boiling point etc. (Table 3.9).

Table 3.9: Properties of Toluene and Hexane solvents.

	Hexane	Toluene
Boiling point (T_{eb}) (°C)	68	110
Density (g cm^{-2})	0.66	0.867
Cinematic viscosity (mm^2 s^{-1})	0.5	0.64
Dynamic viscosity (mPa s)	0.33	0.56

For a successful deposition by spin coating, viscosity and the evaporation rate of the solvents have fundamental impact[118]. Toluene has higher viscosity both dynamic and cinematic, higher density and boiling point; all these properties should lead to a better spreadability on the FTO glass. The depositions were then repeated suspending $CsPbBr_3$ in toluene.

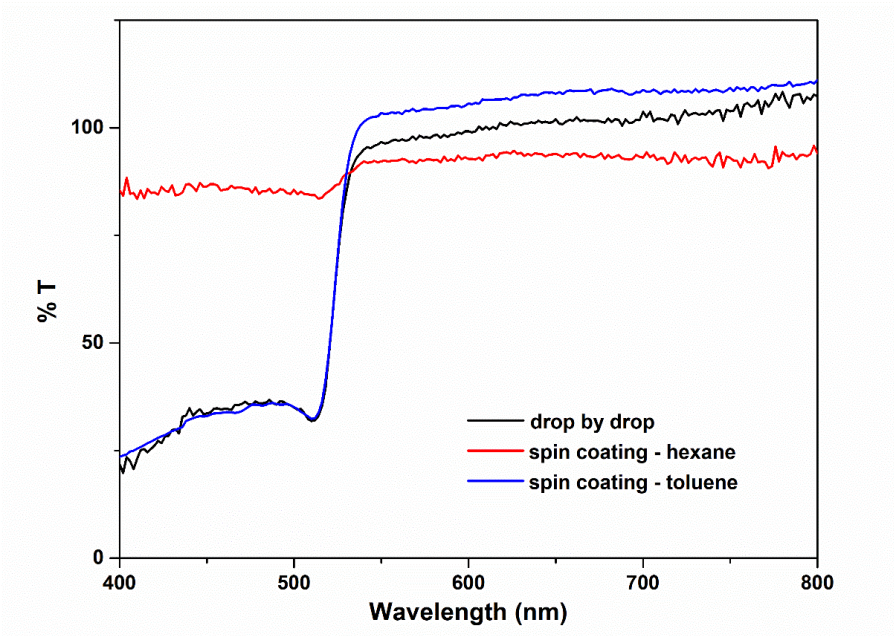

Fig 3.28: Transmission analysis of the $CsPbBr_3$ film deposited with drop by drop deposition method and spin coating method using toluene as solvent.

As results of a better film quality, the absorption of the perovskite when suspended in toluene and deposited by spin coater was more intense than what previously obtained. Toluene was therefore chosen as solvent for this process.

Both the oleate and microwave synthetized suspension were considered suitable to be deposited via spin coating. The deposition was characterized by SEM which shows the

higher homogeneity of the film produced using the CPB-oleate powders. The particles are however surrounded by the organics remained after the synthesis, as the thermal treatment on the hotplate after the deposition is not enough to eliminate them. On the other hand, for the microwave assisted synthesis the deposition was not homogeneous and the FTO was uncoated for the major part of the area.

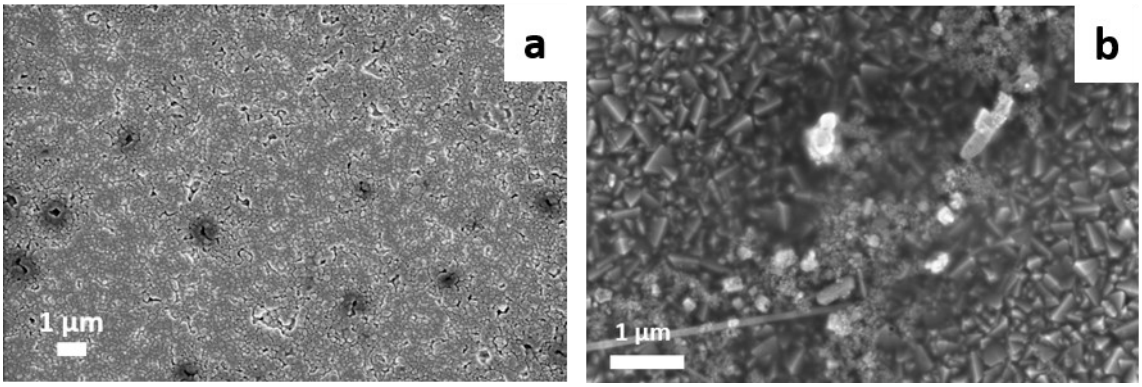

Fig 3.29: SEM images of a) CPB-oleate and b) $CsPbBr_3$-MW in toluene deposited by spin coating.

The reason of the significant differences between the two photoelectrodes, is not clear until yet. The deposition of the CPB-MW will be further investigated to understand the behavior. The only supposition is about the different ratio of the precursor during the synthesis and thus the difference in the suspension concentration. In the next chapters, the electrochemical analyses of both the photoelectrode were reported.

3.2.3. Ink-jet deposition

Ink-jet printing was studied to further enhance the $CsPbBr_3$ layers in terms of homogeneity and thickness, this technique is very powerful but its optimization is quite complex not just for the operating parameters but also because the ink have to respect some precise parameters to be printed, mainly related to the surface tension and rheology. These properties are used to calculate the Oh number, and the reciprocal value called Z that have to be between 1 and 10 ($1 < Z < 10$) to claim the ink formulated printable. The CPB-oleate suspended in hexane was considered for the determination of the surface tension, and of the contact angle on the FTO glass.

Table 3.10: values of surface tension and contact angle of the $CsPbBr_3$ suspension in hexane.

N	Surface tension (mN m^{-1})	N	Contact angle
1	20.17	**1**	7.46°
2	20.05	**2**	5.71°
3	20.15	**3**	6.95°
4	19.98	**4**	6.76°
5	20.25	**5**	6.41°
Avarage	20.12	**Avarage**	**6.66°**

The volume of each drop was 1 µL and the average value of the surface tension was of 20.12 ± 0.11 N m^{-1} while the contact angle was 6.66 ± 0.65 °. These values were used to calculate the Oh number giving the value of 0.0108 and Z = 92 that indicate that the ink is not suitable for the process.

The same characterizations were conducted on $CsPbBr_3$ suspended in toluene (Table 3.11).

Table 3.11: values of surface tension and contact angle of the $CsPbBr_3$ suspension in toluene.

N	Surface tension (mN m^{-1})	N	Contact angle
1	30.26	**1**	14.90°
2	30.27	**2**	12.79°
3	30.30	**3**	18.36°
4	30.20	**4**	26.36°
5	30.23	**5**	37.34°
Avarage	**30.25**	**Avarage**	**21.95°**

The surface tension was found to be 30.25 ± 0.04 mN m^{-1}, while the contact angle 21.95 ± 10.03° the high variability of this latter properties was due to the fact that the drop on the FTO glass spread instantly making difficult the measurements. Oh number of the $CsPbBr_3$ in toluene ink was found to be 0.013 and Z = 76.5 and also in this case, the parameters did not respect the limitation for the ink jet printing. The suspension of CPB-oleate was then modified to reach the right parameters for being printed adding two type of Polyethylene glycol (PEG 200 and PEG 300). These compounds should increase the surface tension and acting as wetting agents helping the deposition of the ink on the substrate. Three samples for each type of PEG were prepared using different

concentrations (0.25 % v/v, 0.5 % v/v and 1% v/v). The suspension turns from the characteristic brilliant green/yellow colour of the $CsPbBr_3$ perovskite to a transparent suspension, clear sign of dissolution of the perovskite induced by the additives. Knowing the low stability of the perovskite in polar environments, a non-polar agent Diiodomethane (DI) was added to the perovskite suspension in toluene. The modifications however were found to be not effective in fact, also in this case, the dissolution of the $CsPbBr_3$ and the discoloration of the ink were clearly visible.

It is worth mentioning that there is no clear consensus in literature around the value of Oh needed for a successful ink-jet printing. This is in fact considered more as a rule of thumb than a real exact constrained. For this reason, a printing attempt was done with the toluene suspension based on a suitable value of surface tension. The ink was therefore printed on the FTO glass. In order to be effective, other than the suspension characteristics, the technique requires an optimization of the process parameters, in particular the pulse voltage, the pulse length and the frequency of the pulse. In Table 3.12 were reported the different conditions tried, in order to achieve a performant printing. The best conditions for this ink were found to be 210 V as pulse voltage, 75 µs as pulse length and 116 Hz as frequency.

Table 3.12: trials of ink-jet printing conditions

N	Voltage (V)	Pulse length (µs)	Frequency (Hz)
1	201	129	499
2	201	129	998
3	201	100	499
4	201	85	499
5	210	129	499
6	210	135	1036
7	230	85	1036
8	230	75	1036
9	210	75	116

Some preliminary tests printing just a line on the substrate were carried out before choosing the more performant sample to use afterwards. During the printing the FTO substrate as put on a heated sample holder kept at 50 °C. Considering the boiling point of toluene, a trial was done also at higher temperature (T = 75 °C). The sample printed at T = 75 °C was considered better in term of drying and homogeneity however one

deposition was not enough to adequately cover the substrate. The rest of the samples were obtained depositing 5 or 10 layers.

Fig 3.30: Preliminary printings of 5 deposition at a) 50 °C and b) 75 °C.

At the final objective is a full printed area of 1 cm^2. A specific serpentine pattern was designed, the distance between each line correspond to 550 µm. Unfortunately, with the sample holder at 75 °C the film for a complete deposition lead to a progressive warm up of the nozzle at T > 19 °C leading to its partial clogging. In order to avoid that, a cooling down step was introduced between each deposition and the holder temperature was decreased to 62.5 °C. Nevertheless, the samples obtained with the holder at 75 °C and subsequent deposition was considered the best condition. This sample was therefore analyzed in term of microstructures and thickness using optical digital microscope, SEM and non-contact profilometer.

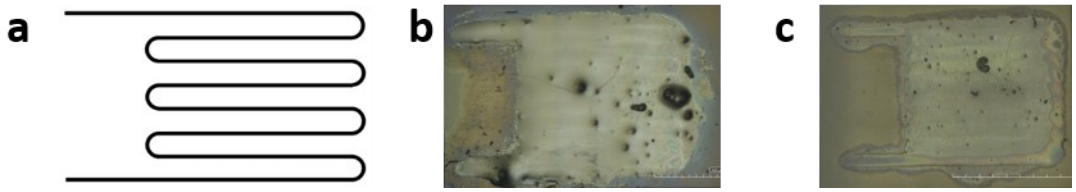

Fig 3.31: a) pathway scheme of the deposition, b) 10 layers at 62.5 °C, and c) 10 layers at 75 °C

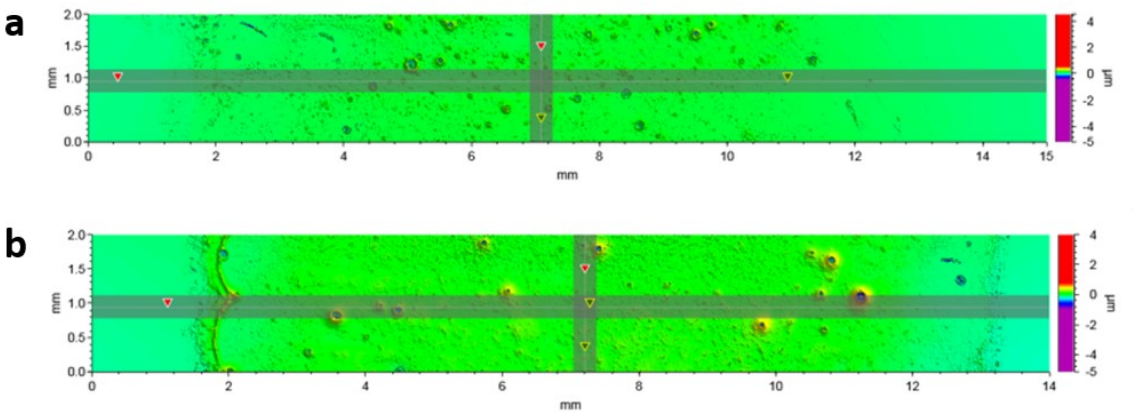

Fig 3.32: Profilometer profiles of the deposition at 75 °C: a) 5 depositions, and b) 10 depositions.

The thickness of the sample with 10 layers (234 nm) was found to be double than the one with 5 layers (98.7 nm); the technique is therefore additive and the number of the layers can be used for a controlled deposition and to know, the thickness of the film.
The printing parameters were able to give a fully covered surface, even if some cracks and imperfection can be seen on the surface of both films. These are mainly due to particle of dust deposited during the process that deeply affects the subsequent drying process.

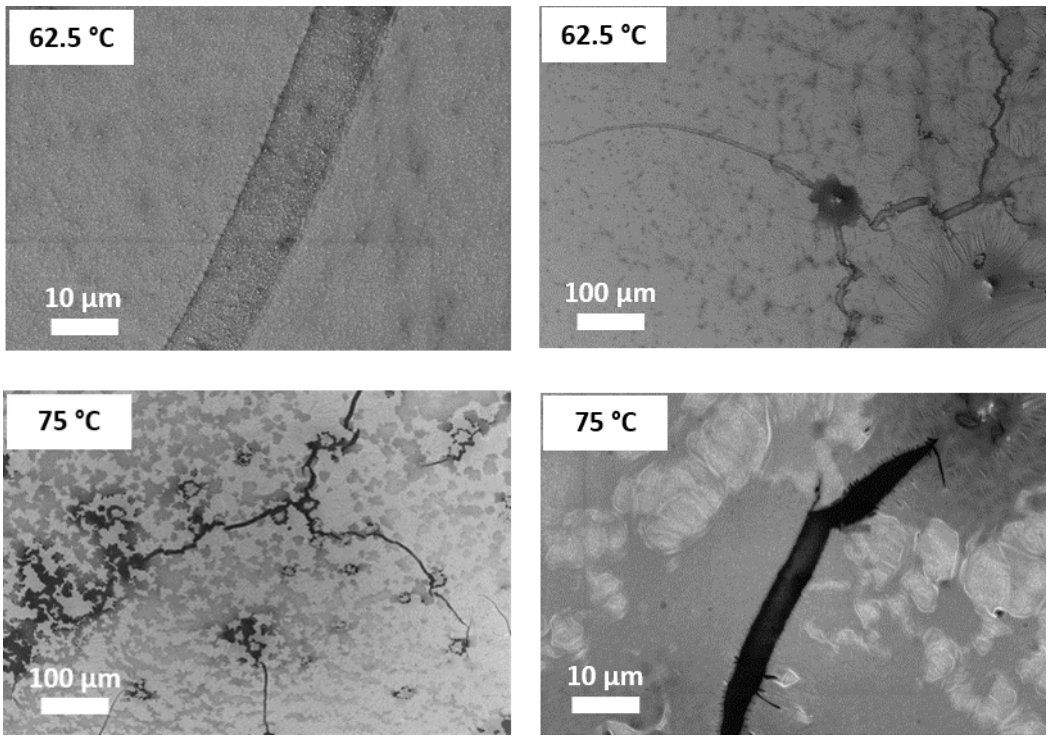

Fig 3.33: SEM details of the imperfections present in the films.

3.2.4. Flash evaporation deposition

In order to assessing the role of microstructure, a film produced by flash evaporation at IMEM-CNR, was considered[119]. The flash evaporation deposition consists in the single thermal ablation of the $CsPbBr_3$ solution precursors ($PbBr_2$ and CsBr dissolved in DMSO). The as deposited film is formed in different stoichiometries ($CsPb_2Br_5$, Cs_4PbBr_6 and $CsPbBr_3$) but after a bland thermal treatment, the system is converted spontaneously in $CsPbBr_3$. In this case the film is formed by a monoclinic phase (PDF#18-0364), the same obtained for the CPB-oleate as confirmed by XRD (Fig 3.34).

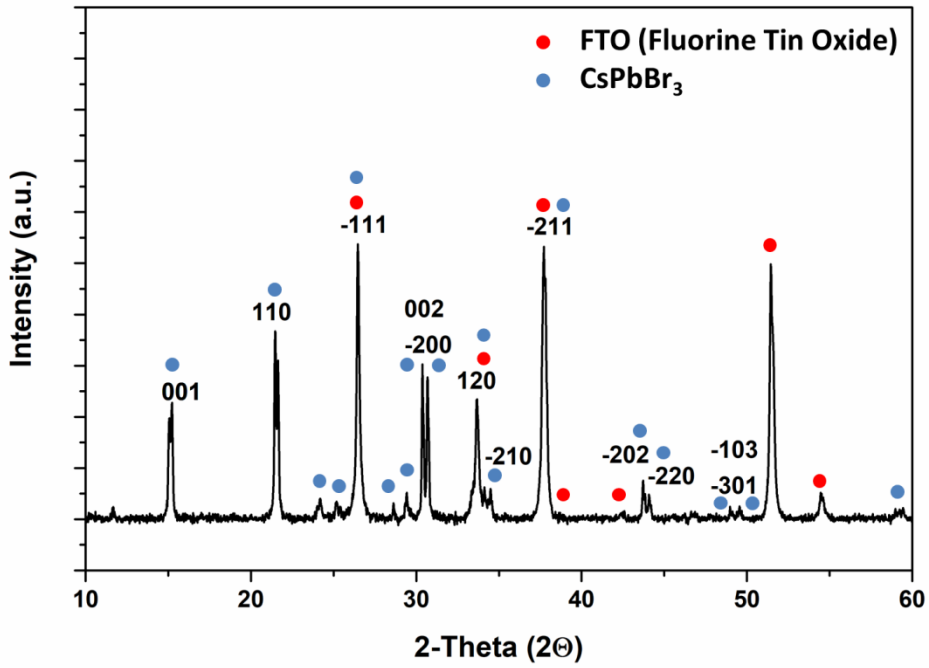

Fig 3.34: XRD of $CsPbBr_3$ dense film deposited by flash evaporation.

Columnar and dense microstructure visible from the fracture in Fig 3.35, where the FTO layer is discernable from the $CsPbBr_3$ layer on the surface. The surface of the $CsPbBr_3$ deposited by flash evaporation results completely homogeneous and compact. The grains are rounded and of homogeneous dimension.

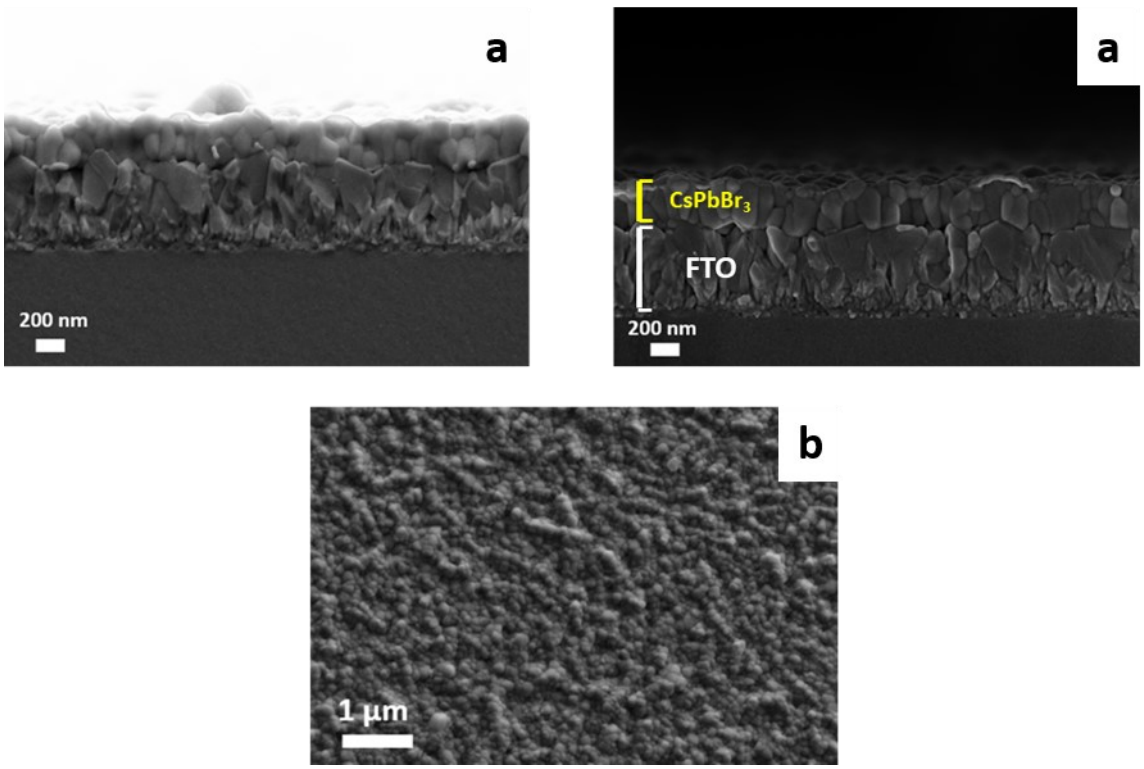

Fig 3.35: SEM images of $CsPbBr_3$ deposited by Flash evaporation. a) section of the $CsPbBr_3$ film, b) surface of the $CsPbBr_3$ film.

The transmission spectrum (Fig 3.36) shows a sharply absorption of $CsPbBr_3$ at 530 nm that corresponds to bandgap value of 2.35 eV consistent with value calculated for the other films.

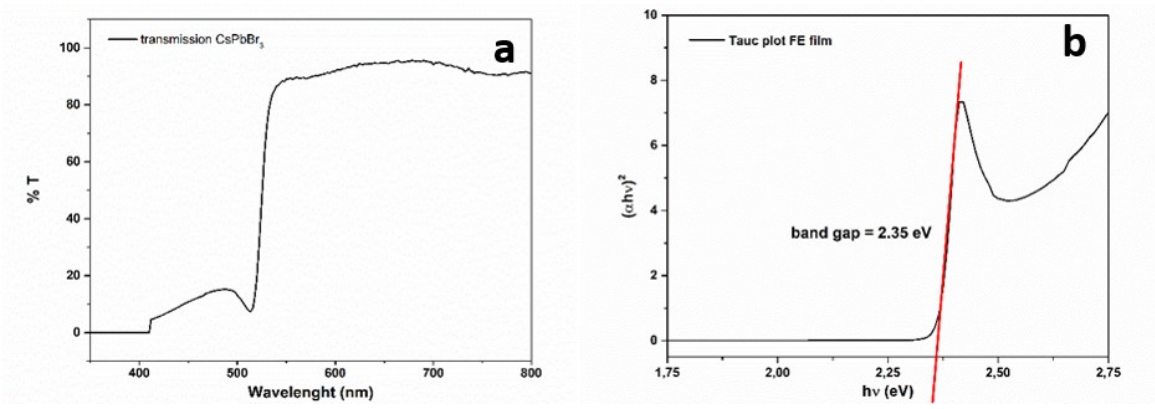

Fig 3.36: Optical analysis of $CsPbBr_3$ film deposited by flash evaporation a) absorbance in the visible region, and b) Tauc plot and extrapolation of the band gap value.

3.3. Aqueous stabilization of $CsPbBr_3$

As shown by the electrochemical analysis of section 3.4, the stability in water is a challenge for the CPB-oleate system. After the characterization, the film of CPB-oleate deposited resulted ruined and in certain cases partially dissolved. To better analyze this phenomenon, the photo-electrodes were analyzed considering optical properties, morphologies and electrochemical properties after the LSV tests in water. In literature is reported that $CsPbBr_3$ in aqueous environment is instable and tend to dissolve just after few minutes[120,121]. The optical analysis reported in Figure 3.37 clearly shows the presence of two absorption bands: the first one (more intense) at 530 nm is related to the $CsPbBr_3$ while the less intense one around 300 nm can be referred to Cs_4PbBr_6 formed by decomposition of the main phase during the analyses in water[108,111,122].

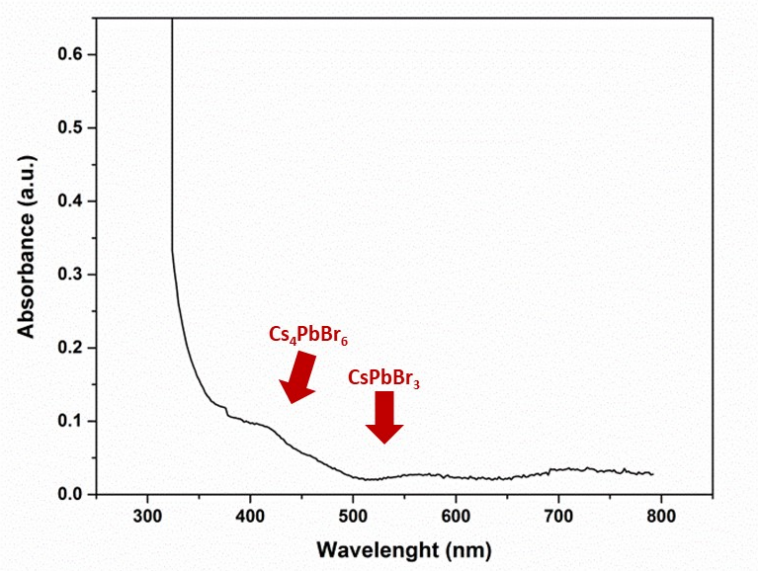

Fig 3.37: Absorption spectra of $CsPbBr_3$ film after LSV test.

Regarding the morphology, in respect to the as prepared one, the film after test (Fig 3.38) is characterized by more defined cubes of larger dimension, with clear signs of the leaching effect of water on the surface.

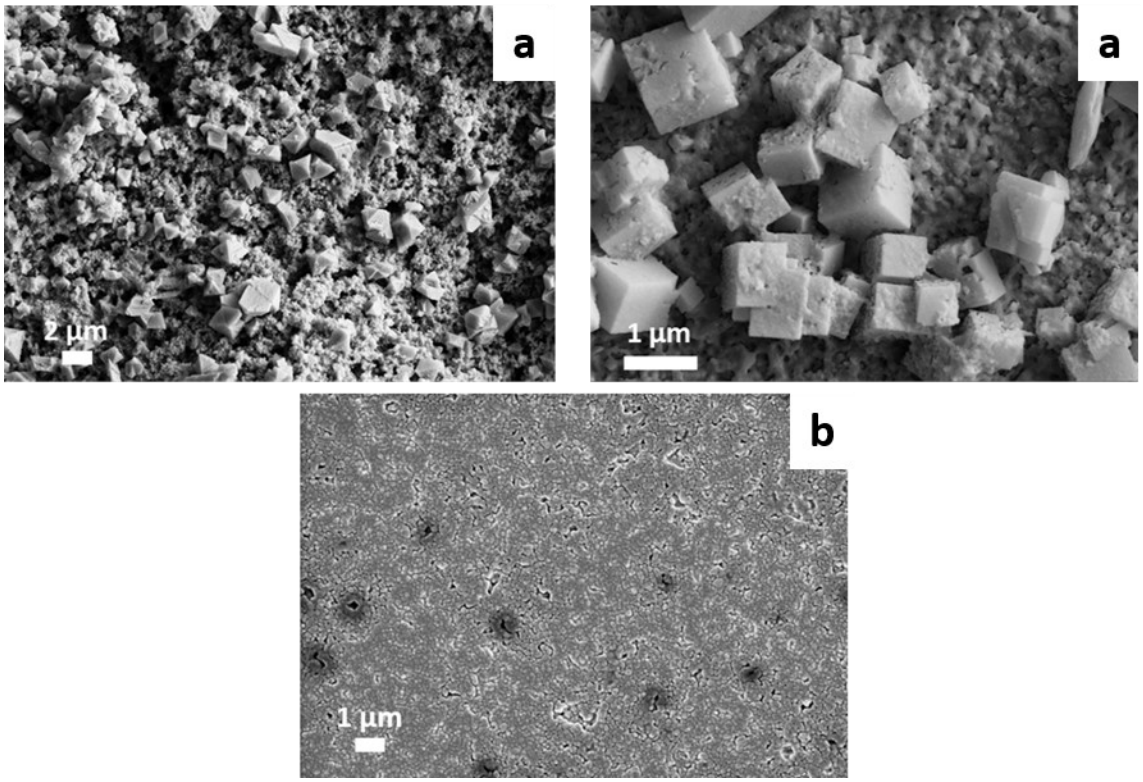

Fig 3.38: SEM micrographs of the film a) after LSV in water, and b) the as prepared one.

The electrochemical properties of the post mortem film were evaluated by cyclic voltammetry using $[Fe(CN)_6]^{3-}$ as electrolyte (Figure 3.39a). Bare FTO electrode and $CsPbBr_3$ as-deposited film were measured for comparison (Figure 3.39b). Figure 3.39a shows a low redox activity of $CsPbBr_3$ NCs thin film on $[FeCN_6]^{3-}$ electrolyte, especially at reduction potentials. The oxidative peak was found at 0.35V vs SCE while reduction peak was not detectable: confirming the presence of the less active mixture $CsPbBr_3/Cs_4PbBr_6$. This result confirms that the synthesis conditions chosen, partially help the preservation of $CsPbBr_3$ even if they are not able to completely protect the system.

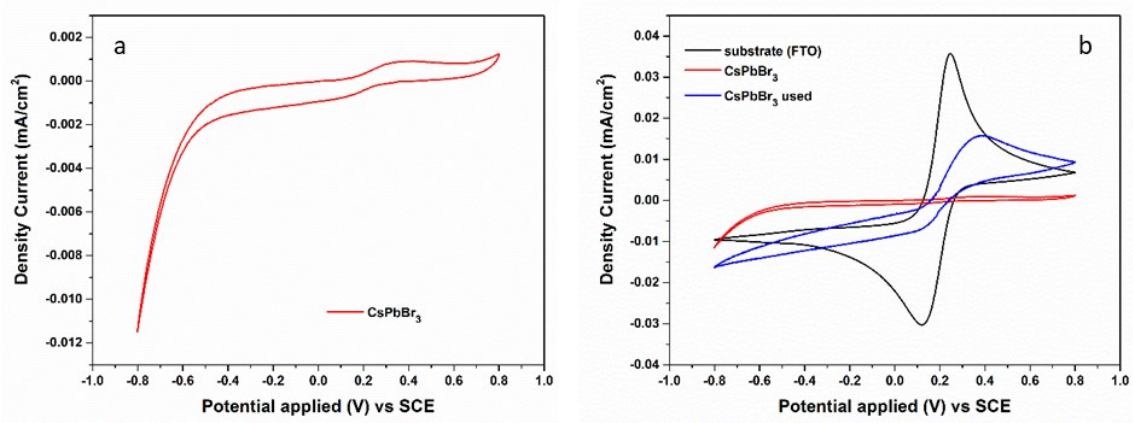

Fig 3.39: Cyclic Voltammograms of a) $CsPbBr_3$ as prepared film b) $CsPbBr_3$ as prepared film, after contact with water and bare FTO substrate.

It is interesting to note moreover that the electrode was still giving a signal even if partially decomposed. D.Y Jung *et al.*[123] reported the electrochemical properties and the capability of a Cs_4PbBr_6 single crystal to produce photocurrent. Also in our case, even if with reduced efficiency, the couple $CsPbBr_3/Cs_4PbBr_6$ was still able to work as material for PEC applications.

In order to solve the problem of the low stability of $CsPbBr_3$ in aqueous environments, two possibilities were taken into account, trying to stabilize the powder before the film processing or protect the already deposited film.

3.3.1. Powder protection

Different approaches were tested in order to protect the powder from water dissolution. In the following they are described in detail.

3.3.1.1. Powder passivation with capping ligands

In literature a lot of solutions as encapsulation with inorganic shells, or surface passivation using organic molecules are reported. In our work this route was considered for the powders produce using the MW synthesis. The powder was treated with the same organic species used during the synthesis (OLA and OA) in ratio 1:1 in order to passivate its surface. The $CsPbBr_3$ was stirred with the OLA and OA for 20 minutes, and

then centrifuged to separate the organic part from the passivated perovskite. The powder was then washed with hexane to remove the excessive organic part, and thermally treated in oven at 100 °C under vacuum and overnight to dry out. The powder treated with organics, even if is not utterly dried, was immersed in water under stirring for 2 hours, to evaluate its stability. Even if, no change in colour was noticed a change in structure related to the same stoichiometry was assessed: from monoclinic PDF#54-0751 to a monoclinic PDF#18-0364 (Fig 3.40). This is linked to a progressively increase in the crystallite dimensions due to aging. The powder retained however a good stoichiometric stability in water.

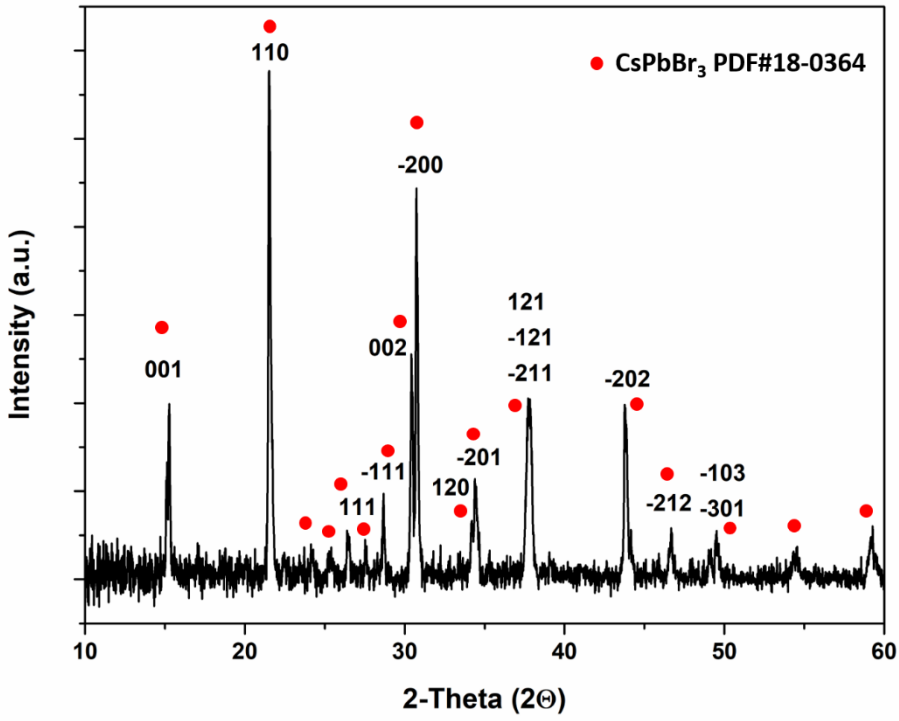

Fig 3.40: XRD of treated MW-$CsPbBr_3$ with OA and OLA and after 2 hours in water.

The photocatalytic activity of this powder is showed in Fig 3.41 where the degradation effect on a Rhodamine B solution is reported.

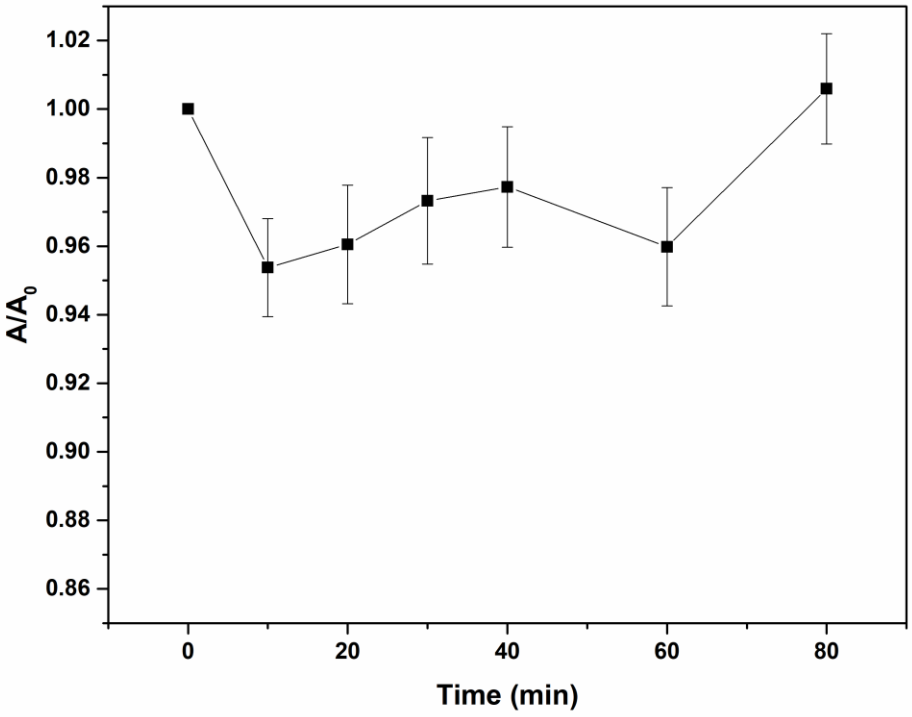

Fig 3.41: Photocatalytic behaviour of MW-$CsPbBr_3$ with OA and OLA.

The treated $CsPbBr_3$, shows no sign of photocatalytic activity during the 80 minutes of irradiation. This behaviour is thought to be due to the absorbed molecules. The organic species used for the passivation, oleic acid and oleylamine, are long chain compounds and in particular both have 18 carbon atoms.

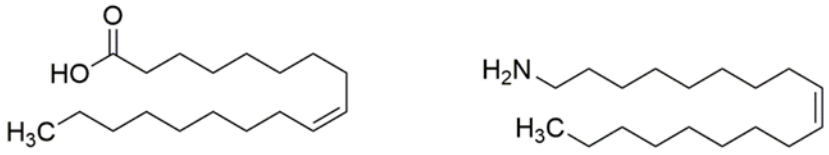

Oleic acid (OA) Oleylamine (OLA)

Fig 3.42: Chemical structures of organic species oleic acid and oleylamine.

The length of the carbon chain probably does not allow the charge transfer during the photocatalytic test, blocking the photodegradation activity. Seen the last results, the passivation of the $CsPbBr_3$ was not considered a viable method to increase the stability of the system in H_2O as it is strongly affected the photocatalytic properties.

3.3.1.2. $CsPbBr_3$ and black phosphorus (bP) or graphene oxide (GO) hybrids

Another way to increase the stability in water of the perovskite particles, is the creation of hybrids materials in situ. In order to do so, two different hybrids were produced: one with black phosphorus (bP) and the other with graphene oxide (GO). The synthesis condition for the $CsPbBr_3$/bP hybrid were found in literature[93,124,125], and the main information were used for the synthesis of the hybrids. In particular, 1 mg of bP was loaded together with $PbBr_2$, Cs_2CO_3, 1-octadecene, oleic acid and oleylamine. The flask was heated on a hot plate at 110 °C for 20 minutes under inert gas (N_2). At the end of the reaction the suspension was centrifuged to separate the solvents and the precipitate was dispersed in acetone to be washed. The acetone was discarding, and a further wash was carried out with hexane. The product was a black precipitate that was characterized by UV-visible spectrophotometry.

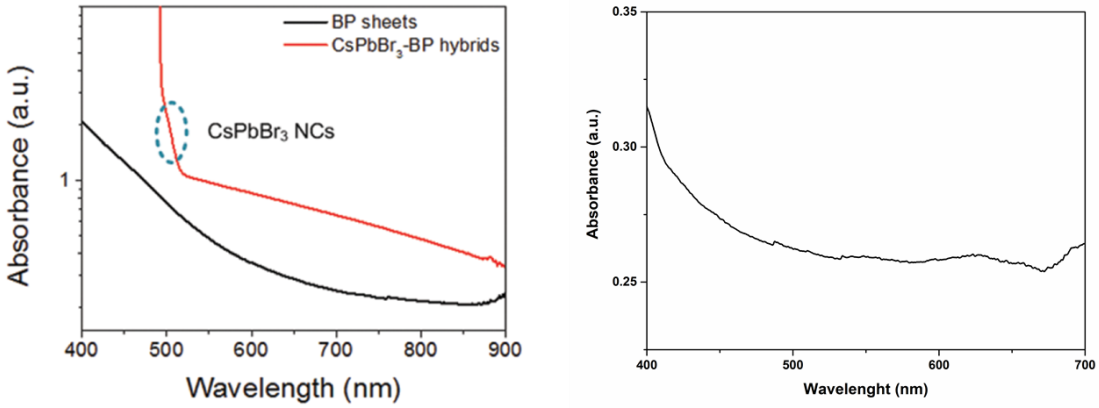

Fig 3.43: Comparison of the absorption of the hybrid synthesized in literature[93] and the synthesis replicated in our laboratory

Fig 3.43 shows the absorbance of the black phosphorus but not the one of $CsPbBr_3$, clear indication that the perovskite was not synthesized correctly. For this reason, another synthesis was carried out, considering three steps. The first considers producing the precursors oleate starting from Cs_2CO_3 and PbO with oleic acid, dissolving the salts at 160 °C, once dissolved the precursors, the solution was diluted with chloroform. In a second beaker, the Br precursor was prepared dissolving tetrabutylammonium bromide (TBABr) with oleic acid and chloroform, at the same time the bP was suspended in

chloroform (1 mg mL^{-1}). The bP suspension was stirred with the oleate precursors and then the Br precursor was rapidly injected in the oleate and bP system. The colour turns immediately into the green-yellowish typical of the $CsPbBr_3$ perovskite. The product was washed with acetone via centrifugation and the precipitate was further characterized.
The same procedure was carried out using 1 mg mL^{-1} suspension of graphene oxide (GO) instead of bP. The hybrid compounds are confirmed with XRD characterization, SEM and TEM images.

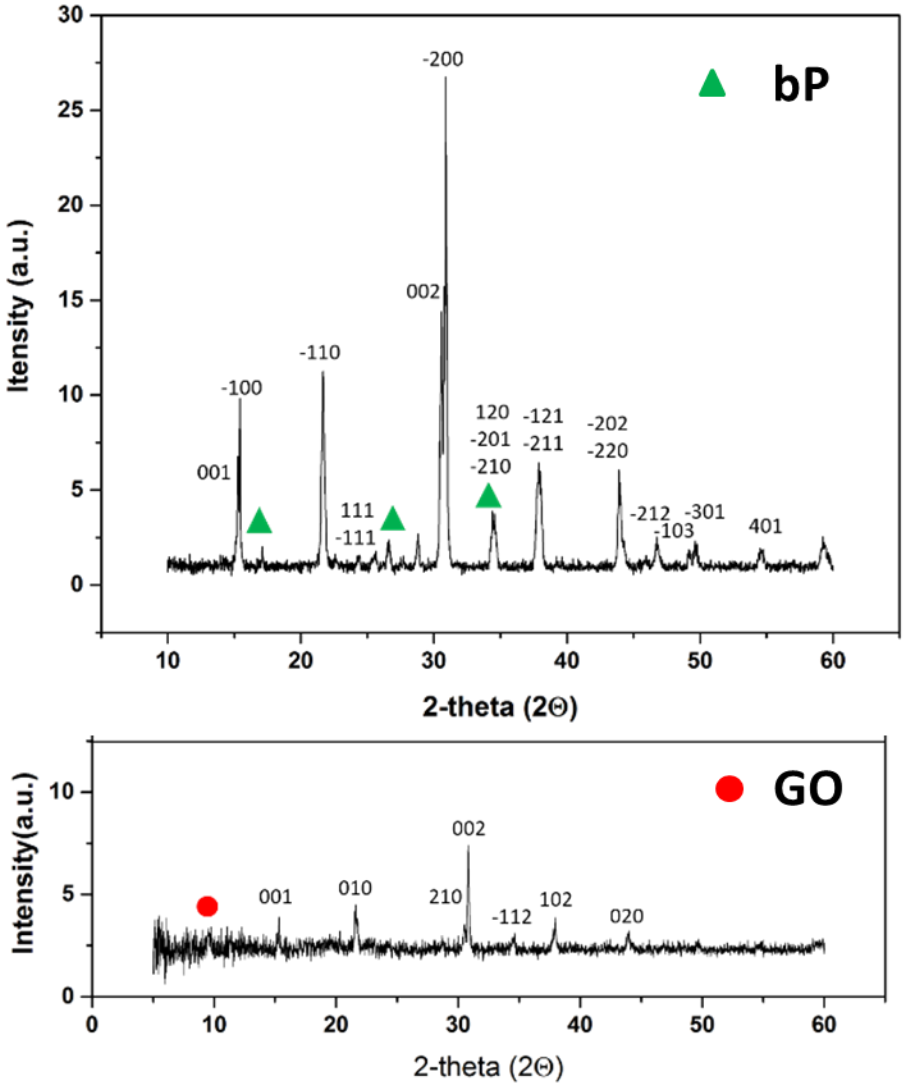

Fig 3.44: XRD of the hybrids $CsPbBr_3$/bP and $CsPbBr_3$/GO.

The XRD diffractograms showed the $CsPbBr_3$ signals (visible from the miller index in Fig 3.44) and the peaks related to the 2D materials (bP and GO). The SEM micrographs and in particular the ones related to the $CsPbBr_3$/bP show clearly the bP sheet with on top

the crystals of $CsPbBr_3$; in the micrograph of the GO hybrid the crystals of the perovskite were visible, the presence of the graphene oxide was confirmed by the typical crumpled paper effect of this morphology.

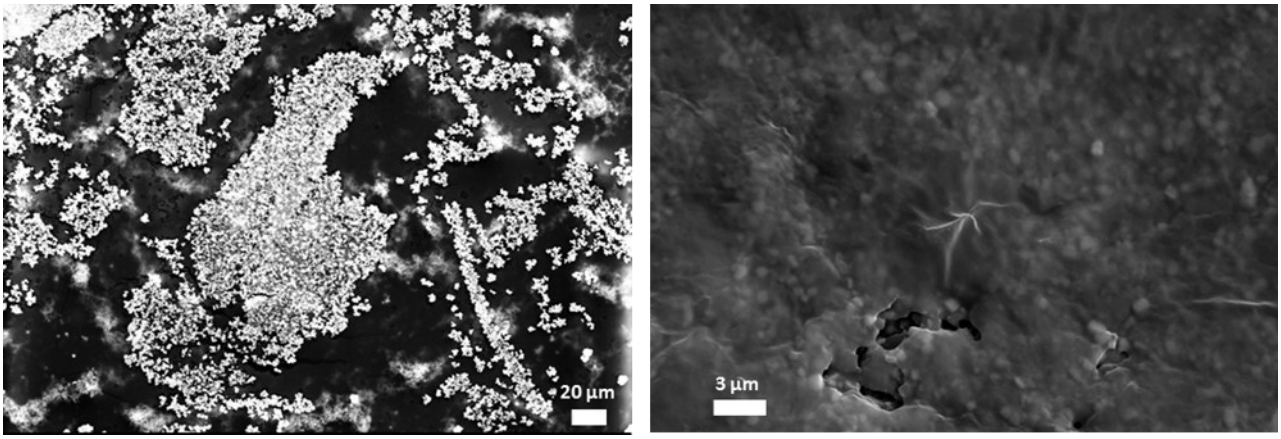

Fig 3.45: SEM micrograph of hybrids $CsPbBr_3$/bP and $CsPbBr_3$/GO.

The TEM micrographs (Fig 3.46) clearly showed the $CsPbBr_3$ crystals on the surface of the bP and GO sheets in the $CsPbBr_3$/bP hybrid, the perovskite crystals were of the same dimension and a higher number of crystals were present on the bP in comparison with the hybrid with GO. Furthermore, the crystals in this case was not so homogeneous from a dimension point of view, but the hybrids were synthesized successfully.

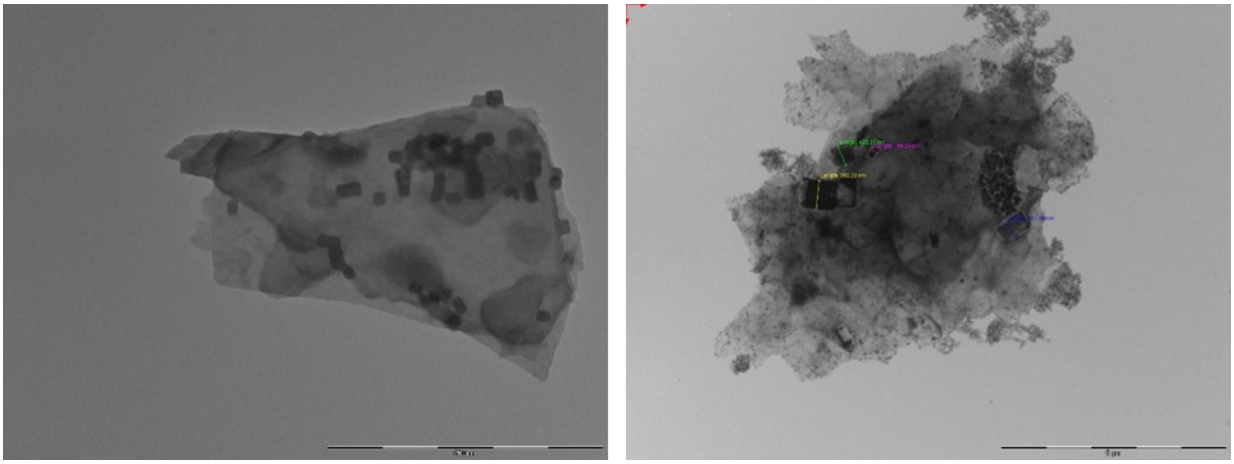

Fig 3.46: TEM images of hybrids $CsPbBr_3$/bP and $CsPbBr_3$/GO.

In order to appreciate the properties of the new materials, they were tested in photocatalytic degradation of RhodB, and the results were compared with ones derived using the single materials synthesized in the same conditions.

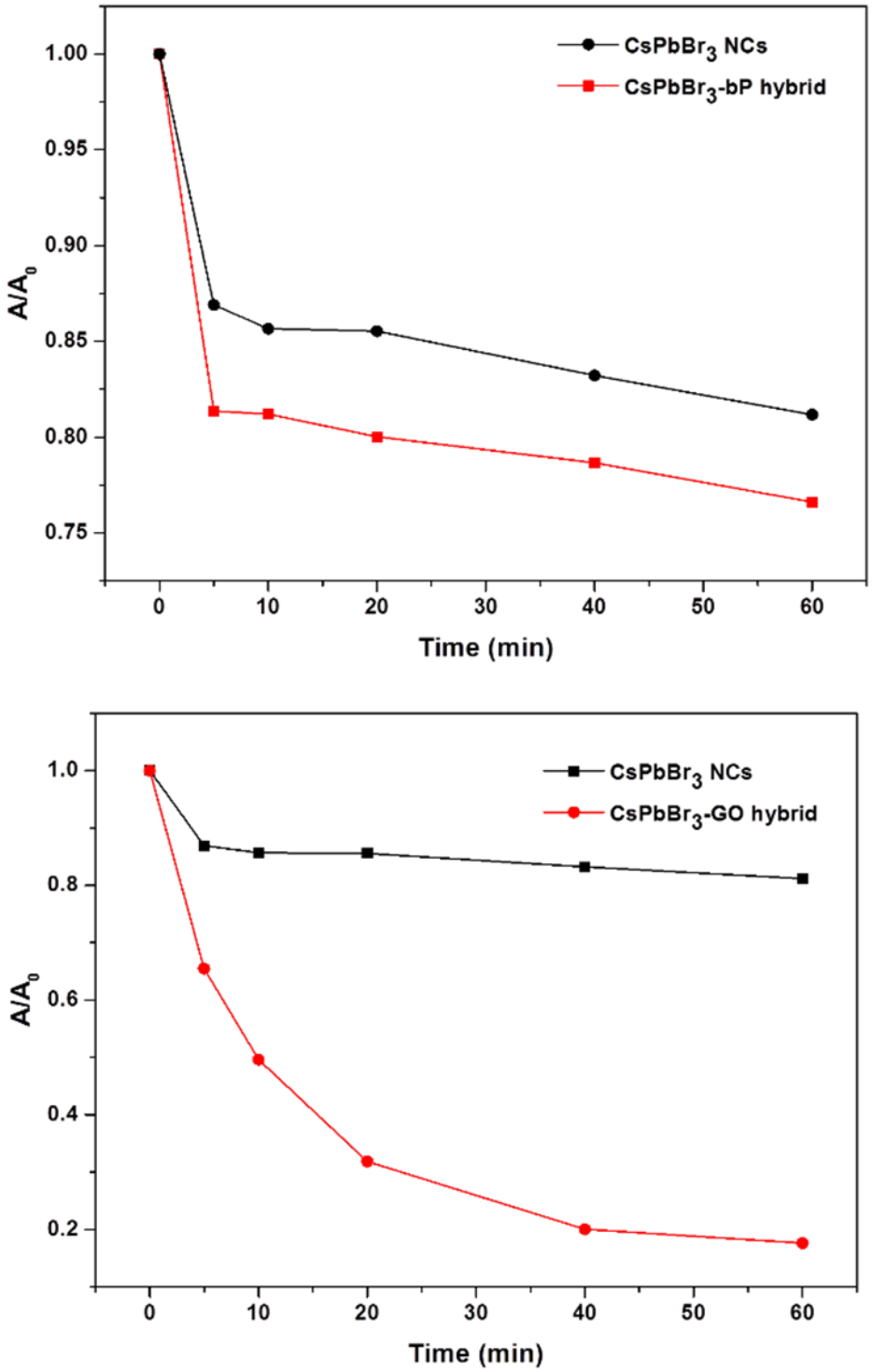

Fig 3.47: Photodegradation tests of hybrids $CsPbBr_3$/bP and $CsPbBr_3$/GO in RhodB.

At first sight the hybrids work better than the single perovskite crystals in photocatalysis, especially in the case of the hybrid with GO. The graphene oxide is a very active material in catalysis and the combination with the perovskite which was active from the

photochemical point of view allow to reach these successfully results. Also for the bP hybrid the combination of the materials bring to a better performance in the photodegradation of RhodB even if of a lesser extent. This is probably due to a synergic effect: the properties of two or more single materials, putting together showed a better result than the sum of each single contributes. Moreover, hybrids reach a higher stabilization in water environment, with no problems of dissolutions or of phase changing. The formation of these hybrids therefore not only improved the catalytic properties but, as expected, enhanced the stability of the perovskite towards the water dissolution.

3.3.2. Film protection

Other than protecting the powder through the formation of hybrids, another way is directly protecting the film after deposition. Two different protective layers were chosen: platinum (Pt) and graphite (C). These materials were considered for their role in catalysis:[126–128] carbon materials are widely used for the heterogeneous catalysis and they have interesting properties such as a chemical inertness, high porosity and large surface area, while platinum is widely used in hydrogen evolution reaction (HER) even if the costs of this noble metal is high. The coating was carried out through flash evaporation in the case of the graphite while platinum was sputtered on the perovskite film. In Figure 3.48 are reported the images of the electrodes before and after coating with graphite and platinum.

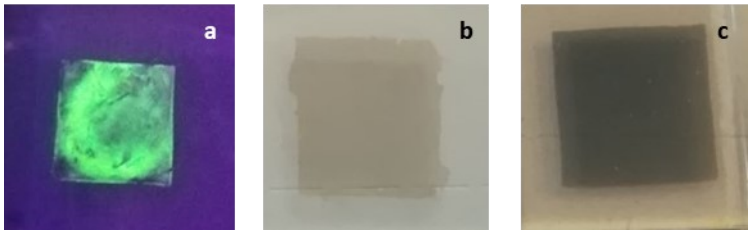

Fig 3.48: a) CPB-oleate film deposited by spin coating and irradiated with UV lamp, b) $CsPbBr_3$ film covered with 10 nm of graphite, c) $CsPbBr_3$ film covered by 10 nm of platinum.

The first analyses considered were the optical one, conducted on films of CPB-oleate deposited with spin coating. In order to photogenerate current for the redox reaction

into a PEC cell, the coating should not hinder the absorption of light by the perovskite. Being the electrodes composed by FTO with a layer of $CsPbBr_3$ and a further layer of Pt or C (Fig 3.49), the optical properties were assessed both when the light hit the electrodes from the substrate side as well as when light hit the electrodes from the coating side.

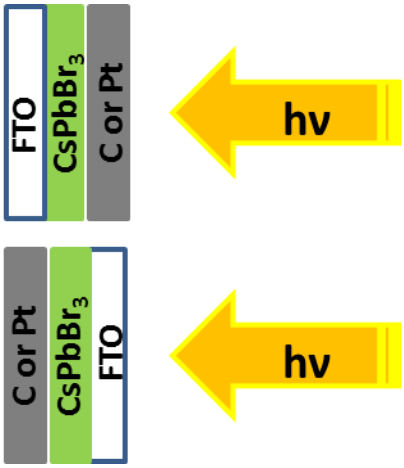

Fig 3.49: scheme of the electrode irradiation during the optical analyses.

The results showed in all cases an absorption peak ascribed to the $CsPbBr_3$ at 530 nm demonstrating that the coatings did not block the light. Besides that, it was possible to see an higher transmission when the photons arrived from the coated side of the electrode; i.e. a lower absorption. The coating did not block completely the absorption of the perovskite, but they limited it in small amount. The visible differences between $CsPbBr_3$/Pt and $CsPbBr_3$/C in Fig 3.50 were due to the coating properties of the layers, platinum in fact is less transparent than graphite.

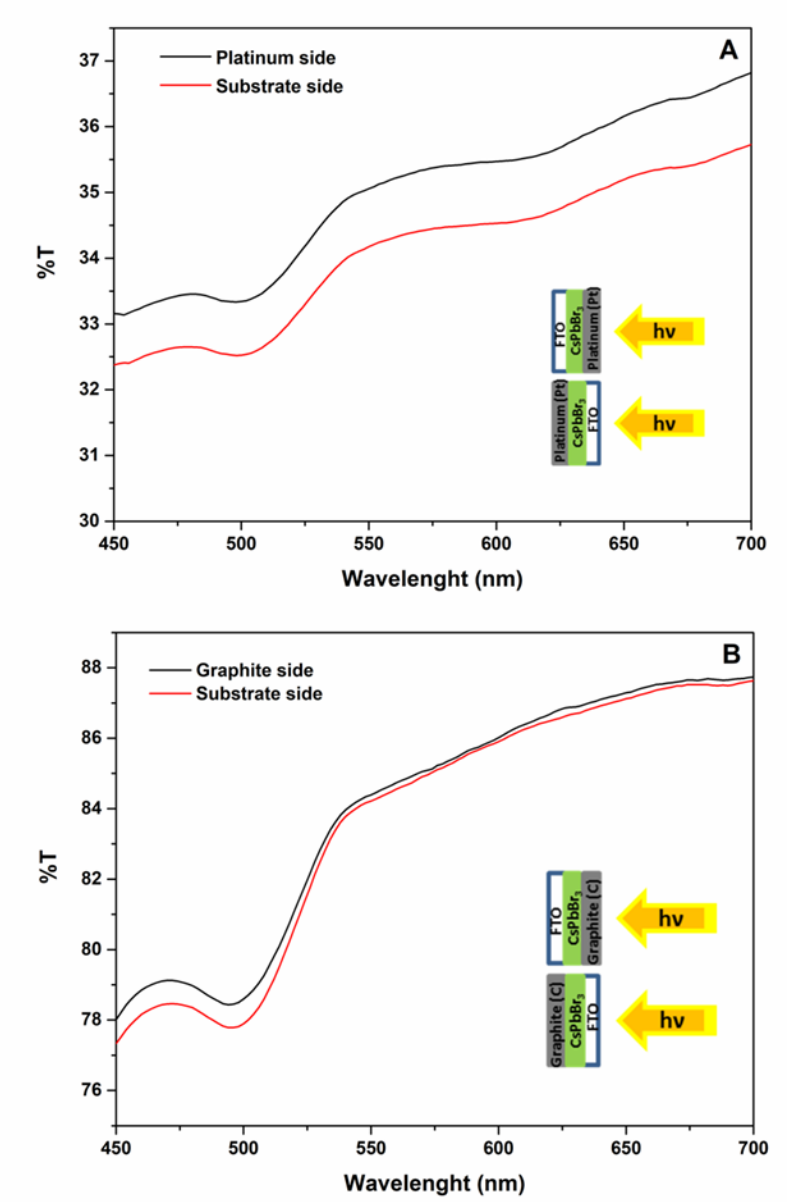

Fig 3.50: Optical analyses on CPB-oleate films coated with a) platinum and b) graphite.

The SEM micrographs of Fig 3.51 show a good homogeneity of the deposition. In the bare $CsPbBr_3$ film are clearly visible the round particles obtained after synthesis that homogeneously cover the FTO substrate. The morphology is obviously changed when an additional layer is deposited on top of the bare $CsPbBr_3$ (Fig 3.51 B and C). In both cases the coatings were anyway homogeneous, and all the surface were well covered.

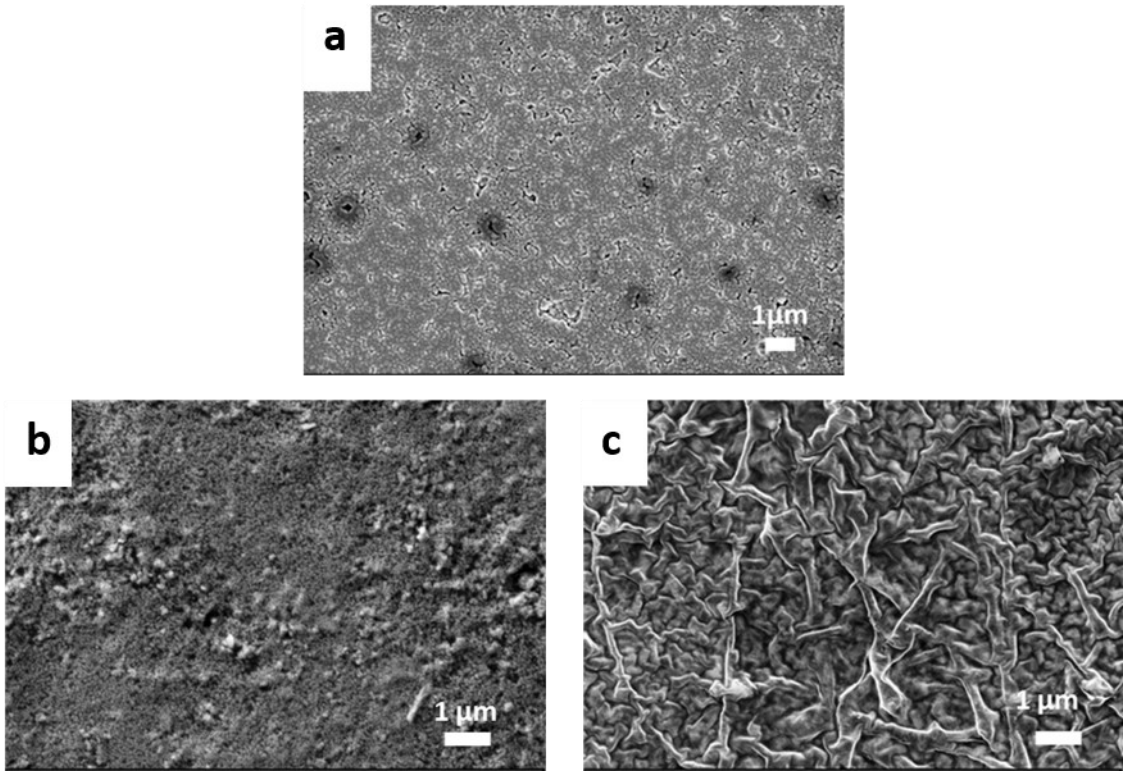

Fig 3.51: SEM micrograph of a) CPB-oleate, b) $CsPbBr_3$/C, and c) $CsPbBr_3$/Pt.

The surface of the coating was also analyzed by XPS. The analyses did not show any peaks relative to the $CsPbBr_3$ in the coated film indicating a good covering of the surface (Fig 3.52).

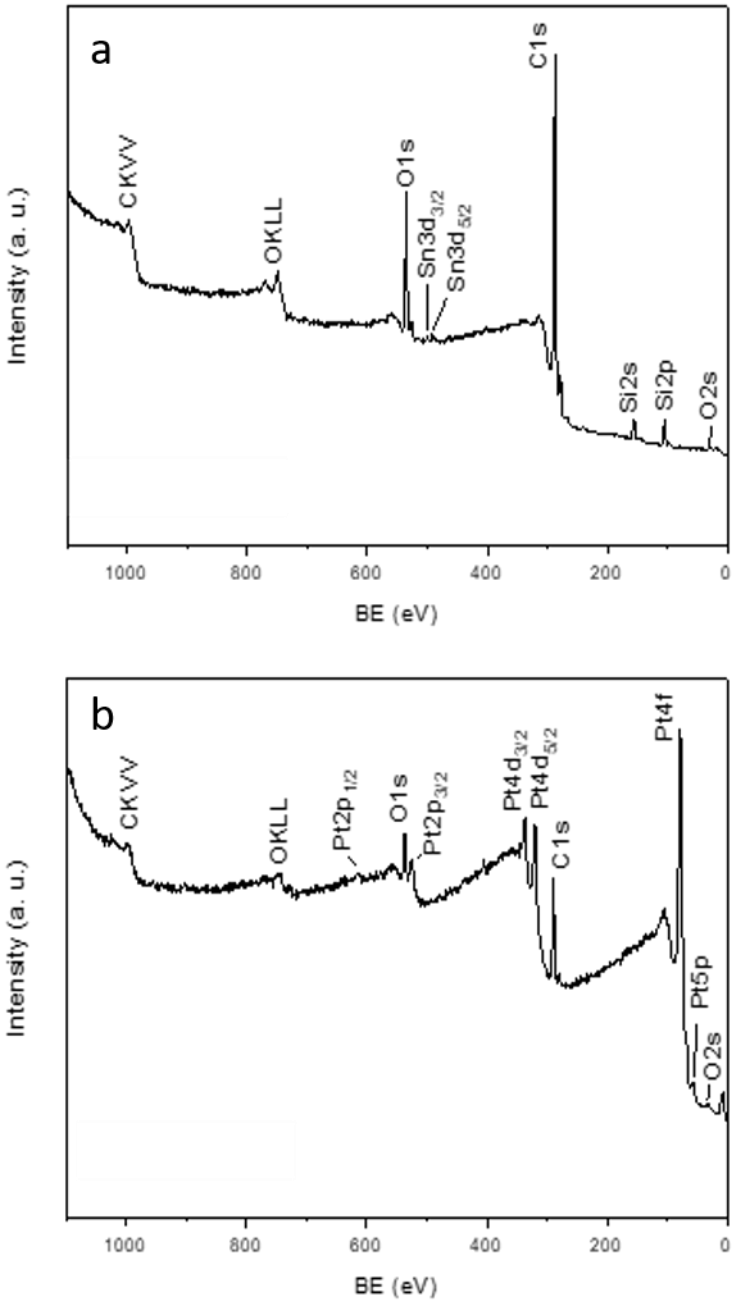

Fig 3.52: XPS analyses of a) oleate-$CsPbBr_3$/C, b) oleate-$CsPbBr_3$/Pt and.

3.4. Electrochemical characterizations

The deposited film of $CsPbBr_3$ were electrochemically characterized in an electrochemical cell to assess the stability of the film during the analyses and to investigate the electrochemical and photoelectrochemical properties of the electrodes.

In deeper, the cyclic and linear voltammetry were carried out to establish the photocurrent produced by the electrode and its water stability thanks to the coatings, while the Mott-Schottky analysis were performed to calculate the flat band potential and to collocate the conduction band and the valence band in the energy diagram. Furthermore, electrochemical impedance spectroscopy (EIS) allowed the study of the interfaces within the electrode layers. All the analyses were performed both on the bare CPB-oleate film and on the protected CPB-oleate as well as on the $CsPbBr_3$/C-MW films and CPB-FE/C, all deposited via spin coating. The more detail discussion will be reported in the following sections of the chapter.

3.4.1. Film as deposited

The electrochemical properties of $CsPbBr_3$ film were determined using Cyclic voltammetry (CV), Mott-Schottky analyses (MS), Electrical Impedance Spectroscopy (EIS) and Linear Scan Voltammetry (LSV). CVs test were carried out at different scans rate (10, 20, 50 and 100 mV s^{-1}) and repeated 6 times. The electrolytes chosen were $K_3Fe(CN)_6$ 1 mM and $Ru(NH_3)_6Cl_3$ 1 mM, both dissolved in a KCl 0.1 M solution. The two species were chosen as they are able to exchange different electrical charges: electrons in the case of $K_3Fe(CN)_6$ and holes with $Ru(NH_3)_6Cl_3$; as shown by their dissociated formula in aqueous solution:

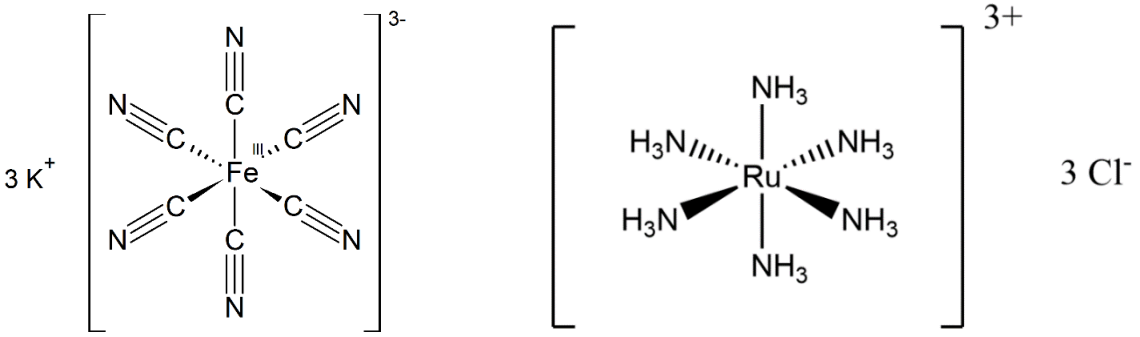

Fig 3.53: Structures of the electrolytes used in CV.

The active couples in solution were therefore Fe(II/III) and Ru(II/III), respectively. The voltammetry graphs reported in Fig 3.54 were recorded at one single scan rate (100 mV s^{-1}).

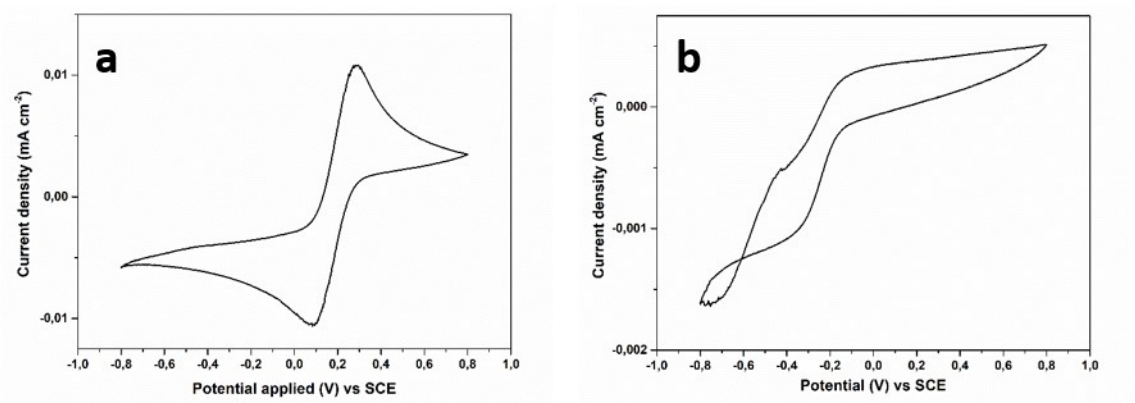

Fig 3.54: CV scans of $CsPbBr_3$ film in a) $K_3Fe(CN)_6$ and b) $Ru(NH_3)_6Cl_3$.

In the analyses carried out in $K_3Fe(CN)_6$ the exchange of the electrons was significant, as showed by the intense cathodic and anodic peaks in reduction and oxidation, while in $Ru(NH_3)_6Cl_3$ only a less defined cathodic peak was detectable. Beside this, the working electrode at the end of the analysis was completely ruined. The time of the CV analyses was too long and lead to the complete solubility of the film. The voltammograms are in fact equal to the spectra of a CV carried out on an FTO substrate indicating the dissolution of the perovskite at the end of the analyses. No electrochemical consideration could be done with these analyses, thus MS, EIS and LSV were considered. From EIS spectroscopy, important information about the electrical nature of $CsPbBr_3$ were achieved, using the same two different electrolytes of the CV analyses. Nyquist plots of Fig 3.55 reported in fact, significant difference in the resistance of the $CsPbBr_3$ if assessed in a negative ($K_3Fe(CN)_6$) or positive ($Ru(NH_3)_6Cl_3$) environment.

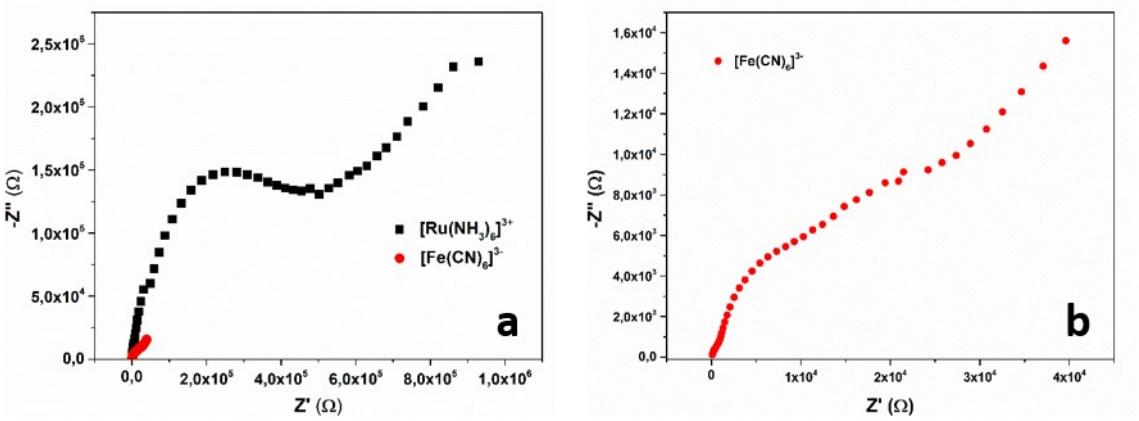

Fig 3.55: a) Nyquist analysis of $CsPbBr_3$ recorded in $Ru(NH_3)_6Cl_3$ and $K_3Fe(CN)_6$ electrolyte and b) zoom of the Nyquist plot recorded in $K_3Fe(CN)_6$.

The charge resistance, represented by the wider semicircle, is clearly smaller for $[Fe(CN)_6]^{3-}$ then for $[Ru(NH_3)_6]^{3+}$. The transfer of e^- at the interface between the perovskite and the electrolyte is therefore easier with Fe than with Ru. The MS analysis was compared with the one of FTO as reference (Fig 3.56a). Both electrodes show a curve with a positive slope indicating that either $CsPbBr_3$ and FTO are n-type semiconductors. In these conditions, the V_{FB} value is close to the minimum of the conduction band of $CsPbBr_3$ and was found to be -1.14 V vs SCE (corresponding to -0,81 V vs NHE), therefore, compatible with the characteristics needed for a photo-electrode in a PEC cell. Moreover, the bandgap value of $CsPbBr_3$ film is suitable for CO_2 reduction since the difference between the valence and the conduction bands includes the potentials of the main CO_2 reduction products (V_{HCOOH}=-0.70 V vs NHE, V_{CO}=-0.62 V vs NHE, V_{CH4} = -0.34 V vs NHE).

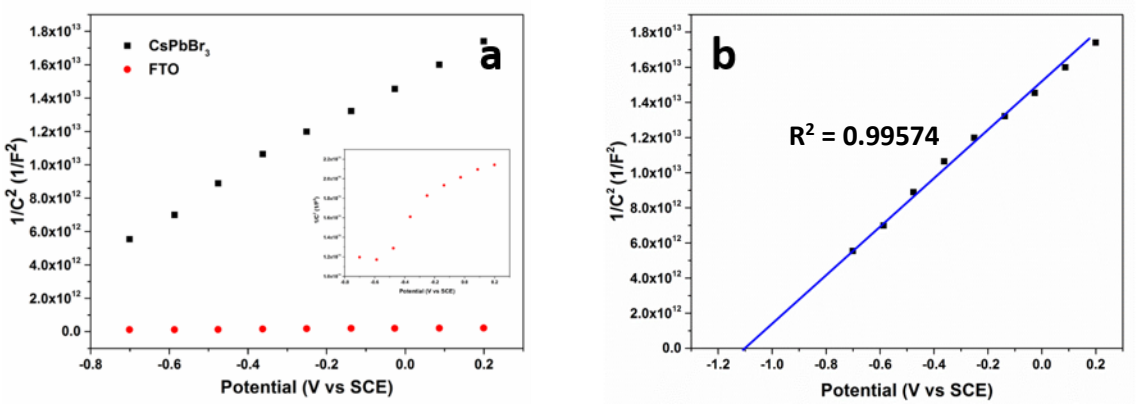

Fig 3.56: a) Mott-Schottky plots (500 Hz) of $CsPbBr_3$ thin film (black line) and of FTO glass (red line), b) plots of the $CsPbBr_3$ thin film and V_{FB} position.

Finally, the film was tested as photo-electrode in photo-electrochemical cell (PEC), using LSV in oxidation and reduction conditions; the curves are reported in Figure 3.57.

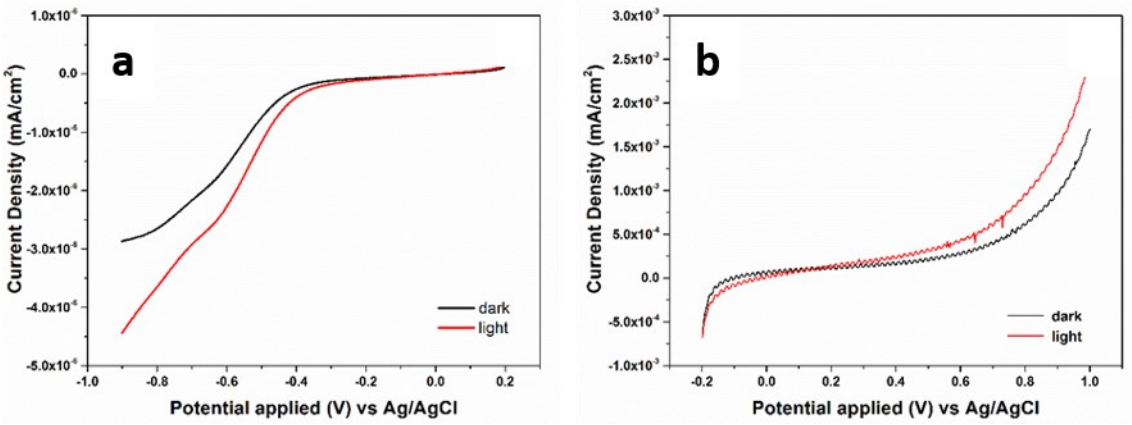

Fig 3.57: LSV curves in the dark and under illumination 1000 W/m^2 conditions in a) reduction and b) oxidation windows.

Even if $CsPbBr_3$ can work as electrode in dark conditions, i.e. as electrochemical material, under illumination the photocurrent produced in both oxidation and reduction conditions is higher. Moreover, the photocurrent started at lower potential under illumination, probably thanks to the low overpotential required to drive the photo-electrochemical reactions. In particular, the differences between current densities produced in dark and during illumination were found to be equal to 4.08 µA cm^{-2} in reduction and 0.55 µA cm^{-2} in oxidation. The highest photocurrent (11.5 µA cm^{-2}) was obtained during reduction while during oxidation 2.25 µA cm^{-2} were produced. These high values of photocurrent are mainly due to the interface where the carriers are photo-generated and the ability to drive reduction and oxidation reactions[92]. The light reaches the $CsPbBr_3$ thin film from the glass side and therefore the electrons and holes are created on the film/FTO interface. In these conditions, when an oxidizing potential is applied to the substrate, recombination processes become predominant and a smaller number of electrons are available. Furthermore, considering the n-type nature of $CsPbBr_3$ film, the holes transfer at the interface $CsPbBr_3$/electrolyte is prevented and therefore the photocurrent produced for oxidation reaction is lower. On the other hand, when a negative potential is applied on the electrode (reducing conditions) more photogenerated electrons are available to drive the reduction reaction and thanks to the n-type conductivity they are able to migrate and react on the $CsPbBr_3$/electrolyte interface. In conclusion, thin film based on CPB-oleate possess suitable optical and electrochemical properties to be applied as photo-electrode for PEC applications, but

show very low stability in aqueous environment, for this reason the further electrochemical characterizations are carried out on protected film of $CsPbBr_3$.

3.4.2. Film with protective layer

The spin coated samples were tested electrochemically to assess the electrical behavior at the interface between the film and the aqueous electrolyte but also between the perovskite and the coatings (graphite and platinum layers). The protected samples were used as working electrodes in a three electrodes cell for the CV, MS, EIS and LSV curves. The electrochemical characterizations are particularly important to study the different role played by the Pt and the C coatings on the properties of $CsPbBr_3$. A platinum foil was considered as counter electrode and saturated calomel electrode (SCE) as reference.

Cyclic voltammetry was considered to study the charge transfer properties of the film, the ability to conduct redox reaction and the stability of the films when in contact with the electrolyte (water-based). The $CsPbBr_3$/C and $CsPbBr_3$/Pt samples were compared with bare $CsPbBr_3$ as working electrodes during 30 scans of CV. Looking at the differences between the first and the last scans, it is possible to determine the level of integrity of the film. Firstly, two common peaks were present in all the samples, i.e. the anodic and cathodic peaks at +0.2 V and +0.15 V (A_0 and C_0) corresponding to the redox processes of the Fe(II)/Fe(III) couple present in the electrolyte. In $CsPbBr_3$/Pt the second cathodic peak at -0.3 V (C_1) can be attributed to the charge transfer between the Pt present both as covering layers and as the counter electrode, and the crystals of $CsPbBr_3$ composing the film[129]. In the first scan of the bare $CsPbBr_3$ the two anodic peaks (A_1 at +0.6 V and A_2 at -0.4 V) correspond to the irreversible processes of oxidation that lead to the formation of $[CsPbBr_3]^+$ and $[CsPbBr_3]^{2+}$. While the cathodic peak at around -0.7 V (C_2) was related to the reduced species $[CsPbBr_3]^{2-}$ [130]. The voltammogram clearly shows the instability of the bare $CsPbBr_3$: after 30 cycles the diagram is in fact the one typical of FTO. In the CV curves related to the $CsPbBr_3$/Pt and $CsPbBr_3$/C hybrid films (Figure 3.58-a and 3.58-b) the same two peaks A_0 and C_0 related to Fe(II)/Fe(III) were observed as indication of an high efficient electrons exchange on the electrode surfaces with the

redox species into the electrolyte. Moreover, the interface created between the perovskite layer and the platinum or graphite one possesses the right electrical properties to allow the electron flow inside the electrode hybrid material. The highest exchanged current density was obtained for the $CsPbBr_3$/Pt electrode (0.1 mA/cm^2) due to the highest conductivity and catalytic activity produced by platinum. Finally, in the $CsPbBr_3$/Pt electrode, a second cathodic peak around -0.3 V (C_1) can be attributed to hydrogen atoms adsorption[131] on the electrode surface. Both the hybrid electrodes with platinum and graphite after 30 cycles maintain the electrochemical properties of the first cycle as indication of an highly improved water stability.

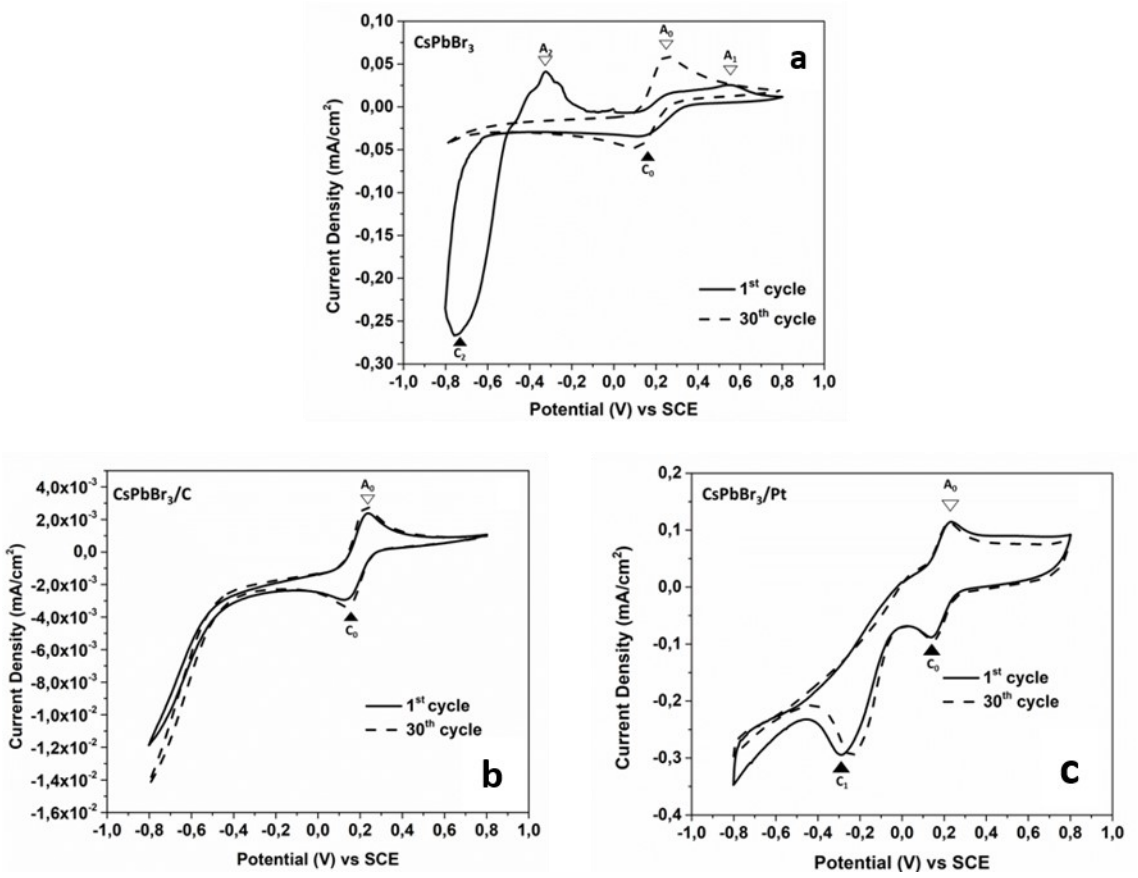

Fig 3.58: Cyclic voltammetry of a) $CsPbBr_3$, b) $CsPbBr_3$/C, and c) $CsPbBr_3$/Pt.

Protected samples were further investigated from the electrochemical point of view through linear sweep voltammetry (LSV), electrochemical impedance spectroscopy (EIS) and Mott-Schottky (MS) analysis. These analyses were performed on the bare $CsPbBr_3$ as discussed in section 3.4.1. Due to its instability in water, the system partially dissolves during the tests and/or changes its stoichiometry. On the other hand, for the coated

films, the electrochemical characterizations were useful to reveal the principal differences between the two coating layers. In Fig 3.59, the LSV reported show small differences between the curves recorded in dark and under illumination, probably the addition of platinum and graphite could well catalyse the reduction also in dark. The main difference between the two coatings relies on the amount of current produced: 10^{-9} mA cm^{-2} for $CsPbBr_3$/C and 10^{-6} mA cm^{-2} for $CsPbBr_3$/Pt. At highest magnification the curves reveal the bigger current produced at -1.5 V vs SCE in light conditions compared to the dark one confirming the effective photoactive role of $CsPbBr_3$. Furthermore, the difference in photocurrent obtained in dark and under illumination, is bigger for the system with Pt (0.32 mA/cm^2) than the one with graphite (0.26 mA/cm^2). Another significant difference is between the potential value where the reduction starts. In $CsPbBr_3$/C the reduction starts at very low potential (-1.3 V vs SCE), while $CsPbBr_3$/Pt needs less external voltage to start the production of current in reduction (-0.7 V vs SCE).

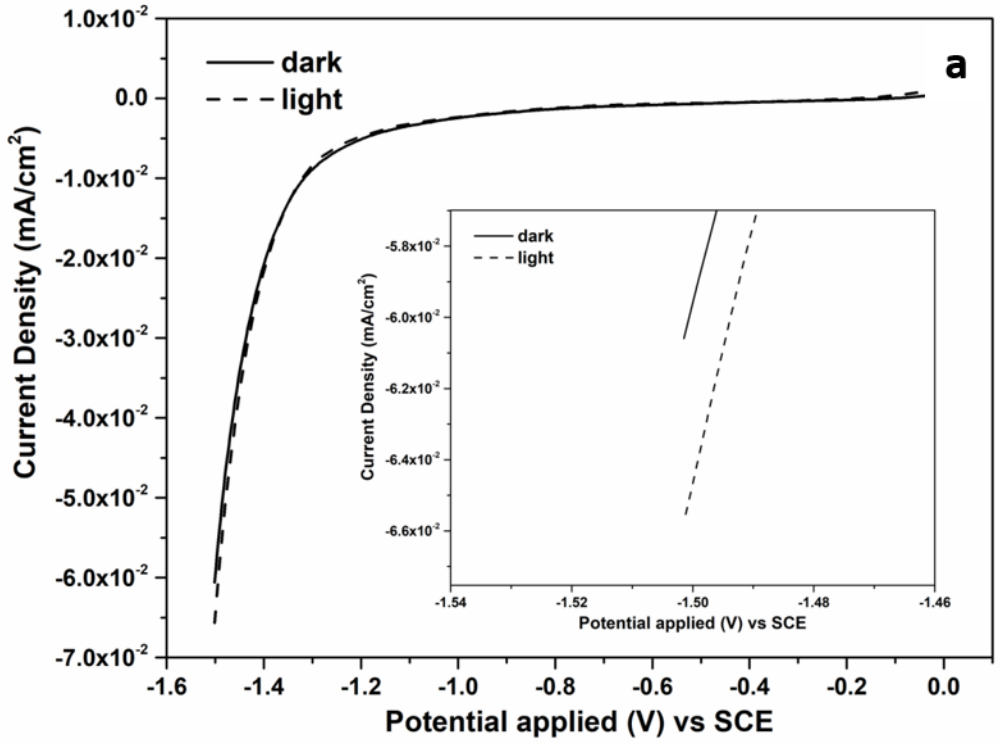

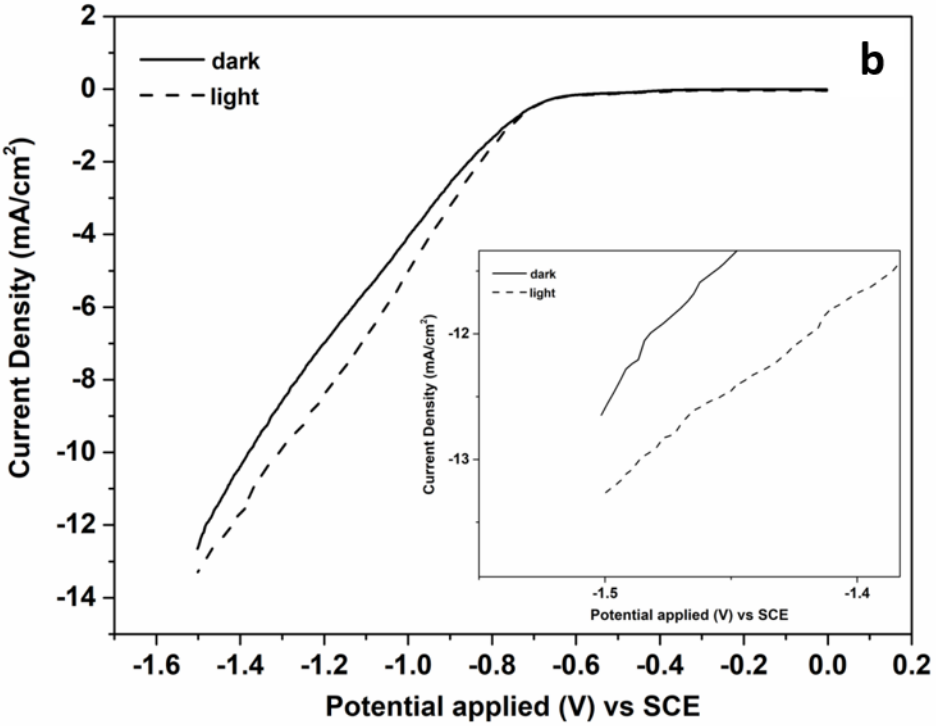

Fig 3.59: LSV of a) $CsPbBr_3$/C and b) $CsPbBr_3$/Pt.

To investigate the recombination and the interface charge behaviour, the different samples were tested using impedance spectroscopy (Fig 3.60a) and analysed using the equivalent circuit presented in Fig 3.60b. The $CsPbBr_3$/C Nyquist plot is characterized by two semi-circles, a small one in the high frequency range and a bigger one in the low frequency range. In the equivalent circuits used to model the film behaviour, R1 describes the overall electrical resistance of the substrate (FTO) and of the deposited film, R2 and CPE1 describe the charge transfer resistance and capacitance (describe as Constant Phase Element) of the interface between $CsPbBr_3$ and platinum or graphite layer, and finally R3 and CPE2 describe the charge transfer resistance and capacitance of the interface between the hybrid electrodes and electrolyte[132]. In addition, in the $CsPbBr_3$/C sample, a diffusive element described as CPE3 was introduced to simulate the straight line at low frequency and was referred to mass transfer and ionic diffusion phenomena to the electrolyte due to the microstructure of this coating. The obtained values of resistance and charge transfer resistance are reported in Table 3.13. A lower R1 value (70 Ω) was achieved for the $CsPbBr_3$/Pt hybrid electrode than the one based on $CsPbBr_3$/C (78 Ω) as indication of the better electrical conductivity induced by the platinum layer. The same results were found for R3 values ($1.6x10^4$ Ω and $13.2 x10^4$ Ω

for $CsPbBr_3$/Pt and $CsPbBr_3$/C respectively) as indication of the better electrical conductivity of platinum and enhanced electrons transfer to the electrolyte. Graphite is in fact more resistive than platinum. On the other hand, the results on charge transfer resistance at the interface between perovskite and platinum or graphite (R2) followed a different trend. In fact, R2 is lower for $CsPbBr_3$/C electrode (2.4 x10^4 Ω) than for $CsPbBr_3$/Pt (7.1 x10^4 Ω) as indication of better electrons transfer at the interface between $CsPbBr_3$ and graphite probably due to a more chemical compatibility between these materials that increase the perovskite and graphite layers adhesion.

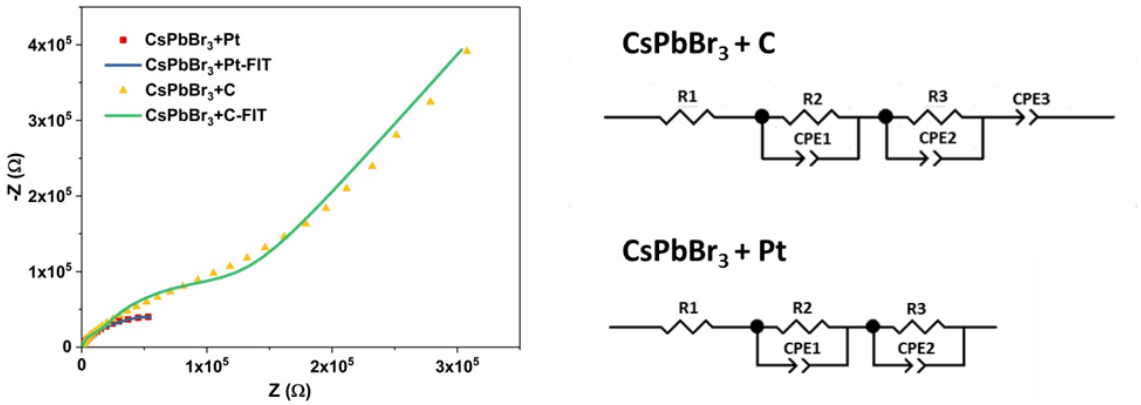

Fig 3.60: Fitting of EIS spectra and relative circuits of only $CsPbBr_3$, $CsPbBr_3$+C and $CsPbBr_3$+Pt.

Table 3.13: Value of electrical resistances for oleate-$CsPbBr_3$/Pt and oleate-$CsPbBr_3$/C.

Sample	R1 (Ω)	R2 (x10^4 Ω)	R3 (x10^4 Ω)
$CsPbBr_3$/C	78	2.4	13.2
$CsPbBr_3$/Pt	70	7.1	1.6

In order to determine the electronic properties of the hybrid electrodes such as conduction type, flat-band potential and number of donors, Mott-Schottky (MS) analyses were carried out. This method measures the capacitance of the layer as a function of an applied potential. The MS plots ($1/C^2$ vs. E) for the $CsPbBr_3$/Pt and $CsPbBr_3$/C electrodes are reported in Figure 3.61a. The positive slope in Figure 3.61a confirms the n-type conductivity of the tested hybrid electrodes. The V_{fb} values were calculated considering the equation:

$$\alpha h\nu = A\,(h\nu - E_g)^n \qquad (3.3)$$

and through the interpolation of the fitting of the experimental points and the X axis and are equal to -1.1 V and -1.7 V vs SCE for $CsPbBr_3$/Pt and $CsPbBr_3$/C electrodes respectively. The data show a clear influence of the interface created between platinum and graphite with $CsPbBr_3$ layer. In fact, the V_{fb} of the $CsPbBr_3$/C electrodes was more negative than the one obtained for $CsPbBr_3$/Pt as indication of less recombination processes at the interface and more electrical charge available to drive photo-electrochemical reactions. For n-type semiconductors, the V_{fb} is generally close to the minimum edge of the conduction band (mV_B); this can be calculated adding the E_g value to the maximum edge of valence band (MV_c)[133,134]. The measured V_{fb} vs SCE were converted to the normal hydrogen electrode (NHE) scale according to the Nernst equation:

$$E_{NHE} = E_{SCE} + 0.059\, pH + E°_{SCE} \qquad (3.4)$$

Where E_{NHE} is the converted potential vs NHE, $E°_{SCE}$ = 0.241 V at 25°C and E_{SCE} is the experimentally measured V_{fb}. The V_{fb} are then equal to -0.49 V and -1.09 V vs NHE for $CsPbBr_3$/Pt and $CsPbBr_3$/C respectively. With these values and the E_g ones, the energy levels of the related hybrid electrodes were determined and reported in Figure 3.61b. The typical E values for water splitting and carbon dioxide reduction are reported in the energy diagram as well.

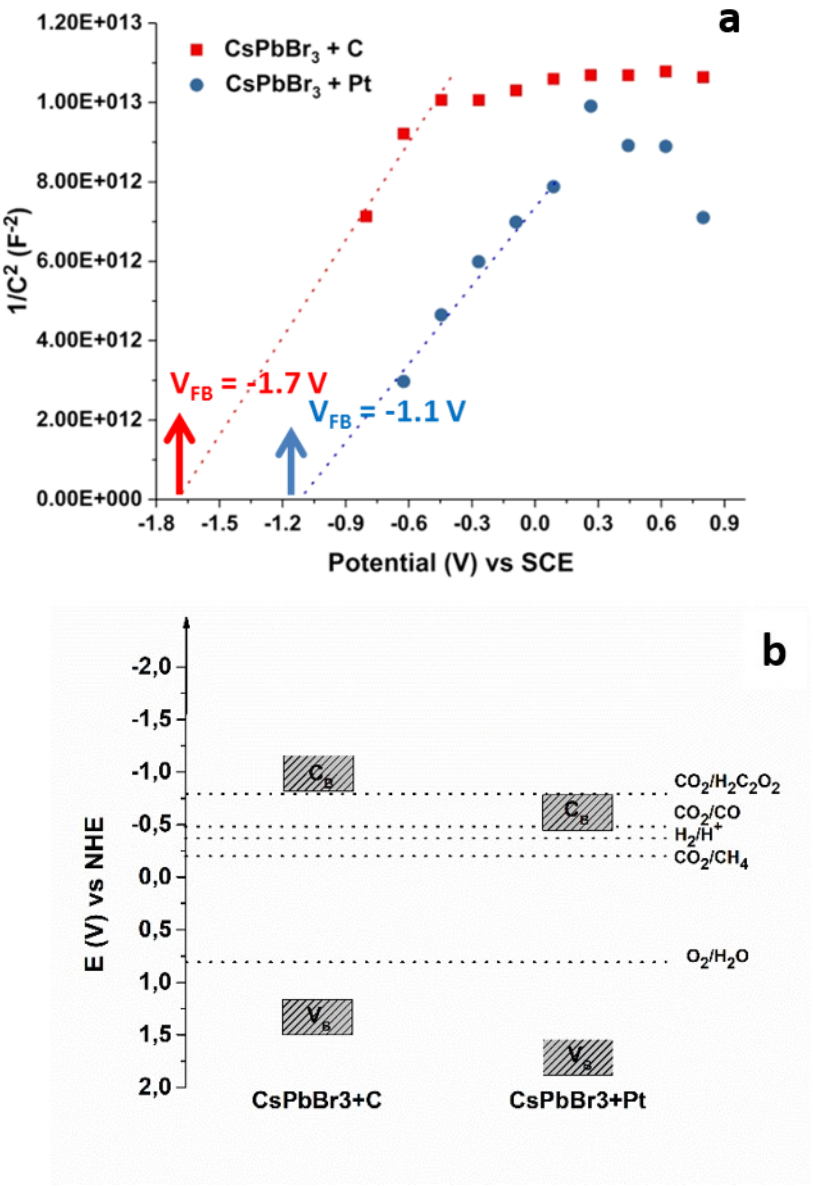

Fig 3.61: a) MS fitting, results and flat band potential values b) energy diagram of $CsPbBr_3$ coated with C and Pt.

Looking at the energy diagram, it is clear that the reduction of CO_2 to chemicals is thermodynamically possible with both $CsPbBr_3$/C and $CsPbBr_3$/Pt. The standard potential of all the reactions are inside the band edges of the V_B and C_B of $CsPbBr_3$. The $CsPbBr_3$/C has more negative band values than the $CsPbBr_3$/Pt, for the latter one, some of the potentials of the main reactions are closer or corresponded to its conduction band. However, this does not impede the possibility of the CO_2 reduction.

The same electrochemical characterizations were conducted on the film prepared by spin coating but with microwave synthesis. In this case, the samples were covered only with graphite ($CsPbBr_3$/C-MW) avoiding Pt coating for the better efficiency reported in

the PEC cell test (chapter 3.5) using C coating in CPB-oleate. The stability of the $CsPbBr_3$/C-MW in aqueous solution was assessed by cyclic voltammetry (Fig 3.62), as reported before, considering 30 scans and then comparing the first and the last scans.

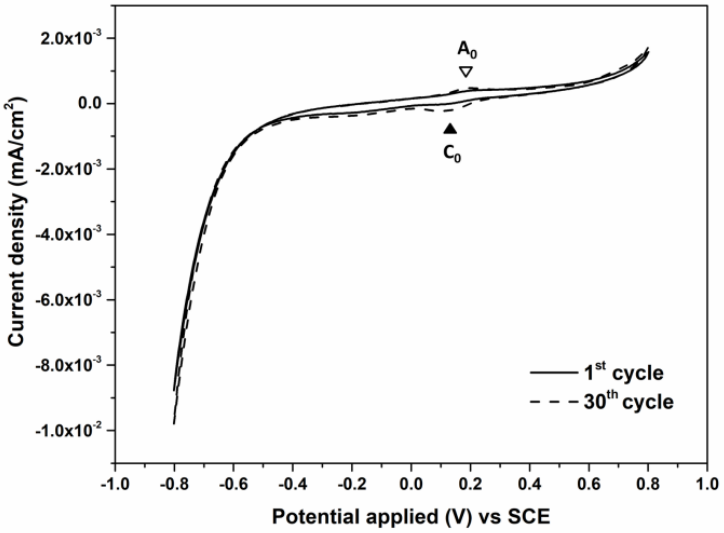

Fig 3.62: CV of $CsPbBr_3$/C-MW.

The two scans are only slightly different meaning the good stability of the protective layer. The two peaks relatives to the Fe(II)/(III) couple are present at ≈ +0.2 V and ≈ +0.13 V. The photoactivity of the electrode was tested with the LSV recorded in dark and irradiating the electrode of $CsPbBr_3$/C-MW (Fig 3.63). As expected, the current produced in dark is lower than the current produced under irradiation, the difference between the two values correspond to the photocurrent produced by the electrode. The current at -1.5 V during the analysis in dark is found to be -0.145 mA cm^{-2}, while under irradiation -0.169 mA cm^{-2}, the photocurrent produced was then 0.024 mA cm^{-2}. The value is lower than the one produced with the oleate synthesis (0.26 mA cm^{-2}) and was thought to be due to the smaller amount of $CsPbBr_3$ deposited on the FTO during the spin coating process as verified by surface analyses (Fig 3.63b).

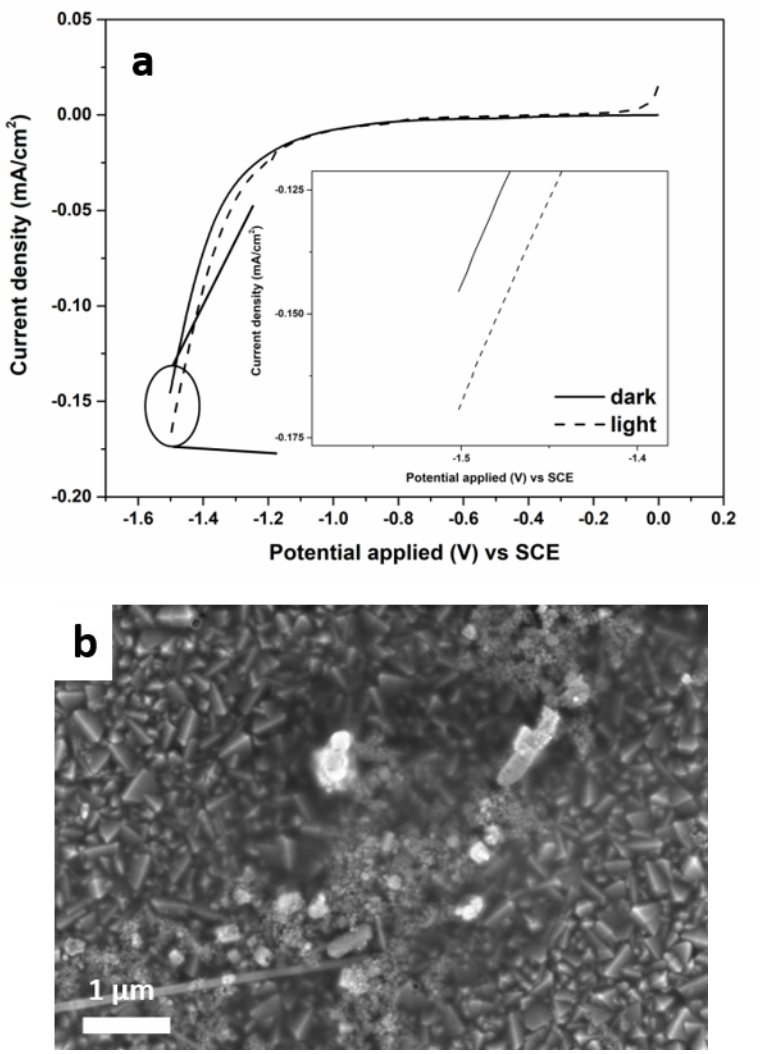

Fig 3.63: a) LSV in dark and under irradiation of $CsPbBr_3$/C-MW and b) SEM micrograph of the $CsPbBr_3$/C-MW spin coating deposition.

Less active material is present on the surface of the FTO lower will be the photocurrent produced. Many differences were found also in MS analysis (and therefore on of the energy diagram), and for the EIS curve used to investigate the behaviours at the interfaces of the electrode. The flat band potential interpolated was found to be Vfb = -0.79 V vs SHE, hence Vfb = -0.17 V vs NHE, as before the energy diagram is build adding to the Vfb the band gap value. The edges of the energies band for the electrode prepared with microwave synthesis and covered with graphite suggest that many reaction of CO_2 conversion are not thermodynamic feasible: the potentials of these reaction are in fact, very close to the conduction potential of $CsPbBr_3$/C-MW electrode but not in between the two energies bands.

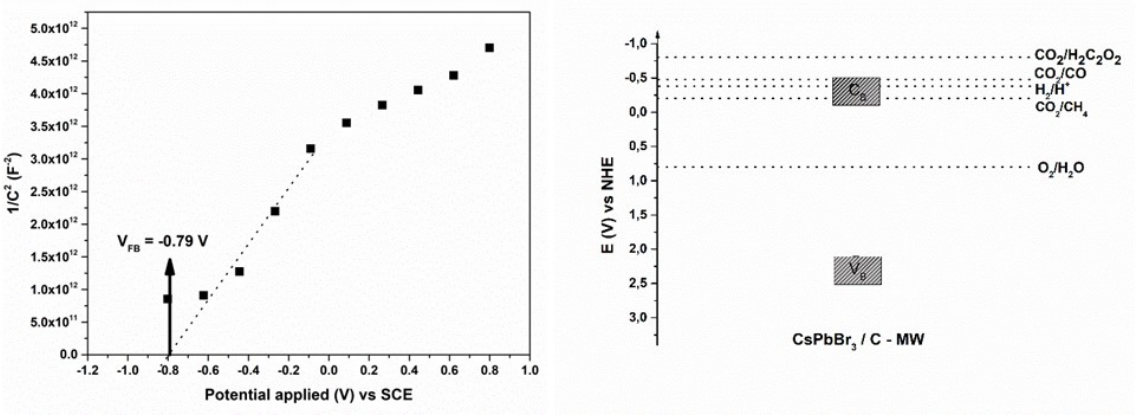

Fig 3.64: Interpolation of the MS diagram to calculate the flat band potential Vfb of $CsPbBr_3$/C-MW and Energy diagram of $CsPbBr_3$/C-MW.

The fitting of the EIS curves reflected the trend seen for the oleate synthesis, but with higher value of resistance at the interfaces. The fitting was done using the equivalent circuit in Fig 3.65 and the resistance value are reported in Table 3.14.

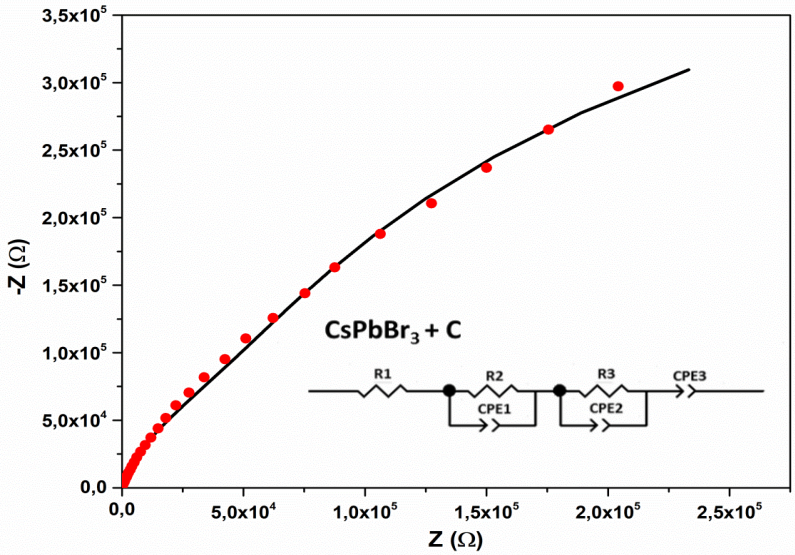

Fig 3.65: Fitting of the EIS curves of $CsPbBr_3$/C-MW.

The $CsPbBr_3$/C-MW sample present lower R2 value (4.38 $x10^4$ Ω) indicating a good electronic transfer between the $CsPbBr_3$ layer and the graphite layer, but R2 in this case is higher than the R2 of the oleate synthesis but lower than the coating with platinum as reported in Table 3.13. The difference between the two electrodes obtained with different synthesis but both coated with graphite is due to the amount of material deposited as reported above.

Table 3. 14: Resistance value of the interfaces between the $CsPbBr_3$-MW and C layers and between the electrolyte and the working electrode ($CsPbBr_3$/C-MW).

Sample	R1 (Ω)	R2 (x10^4 Ω)	R3 (x10^5 Ω)
$CsPbBr_3$/C-MW	37	4.38	8.6

The differences found between the photoelectrode protected with C and build using powders obtained using different synthesis are thought to be due to different amount of material deposited in the two cases. More work is ongoing to obtain film comparable in this sense to verify this assumption.

At the end the electrochemical characterizations were started also on the electrodes deposited by flash evaporation and provided to us from IMEM-CNR. Besides the higher homogeneity and the lack of defects on the surface of the film, the instability of the all-inorganic perovskite in aqueous environment, remains, as confirmed by cyclic voltammetry (Fig 3.66).

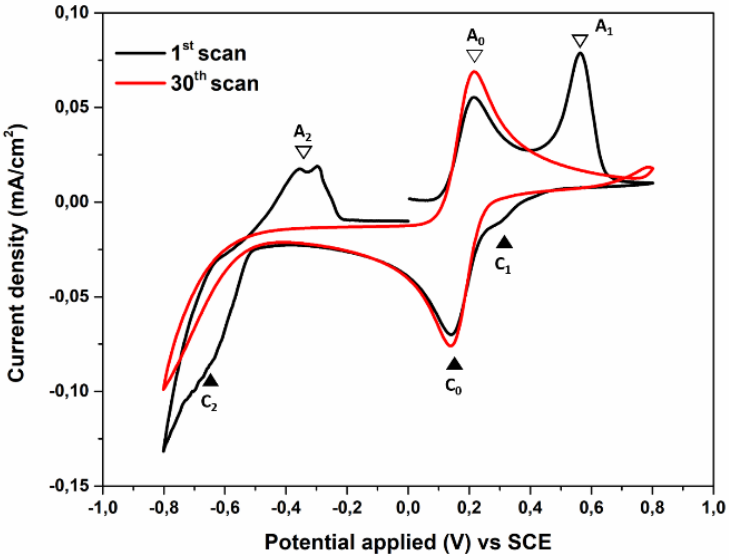

Fig 3.66: Cyclic voltammetry of $CsPbBr_3$ of the first and last analysis's scan.

The first and the last curves were clearly different and confirm the visible degradation of the film in contact with the aqueous electrolyte ($K_3Fe(CN)_6$). Besides that, they have two peaks in common C_0 and A_0 referred to the reversible red-ox processes of the couple Fe(II)/ Fe(III), while the others intense anodic peaks (A_1 and A_2) and less intense cathodic

peaks (C_1 and C_2) present only in the black curve and so in the first scan. The anodic peaks A_1 (0.5 V) and A_2 (-0.5 V and -0.4 V) represent irreversible processes where the $CsPbBr_3$ is oxidized to $[CsPbBr_3]^+$ and $[CsPbBr_3]^{2+}$. On the other hand, the cathodic peaks C_1 between 0.3 V and 0.4 V, and C_2 between -0.6 V and -0.7 V, are due to the reduction of the perovskite to $[CsPbBr_3]^-$ and $[CsPbBr_3]^{2-}$.[130] Also in this case, the perovskite was coated with graphite (CPB-FE/C) and the other electrochemical analyses were carried out starting from the EIS analysis. The Nyquist plot was fitted with the same equivalent circuit of both CPB-oleate/C and $CsPbBr_3$-MW/C electrodes. The values of the resistances R1, R2 and R3 were reported in Table 3.15. R1 is considerable higher in comparison with the one related to the MW and oleate system, indicating the low adherence of the film to the substrate due to the deposition method. In addition, R2 and R3 were significantly lower than the ones of the other systems. This indicates the good charge mobility on the surface of the electrode and their good transfer to the electrolyte. This behaviour is also confirmed by the photocurrent produced of 1.5 mA cm^{-2} and measured by the differences of the LSV curves recorded in dark and under illumination.

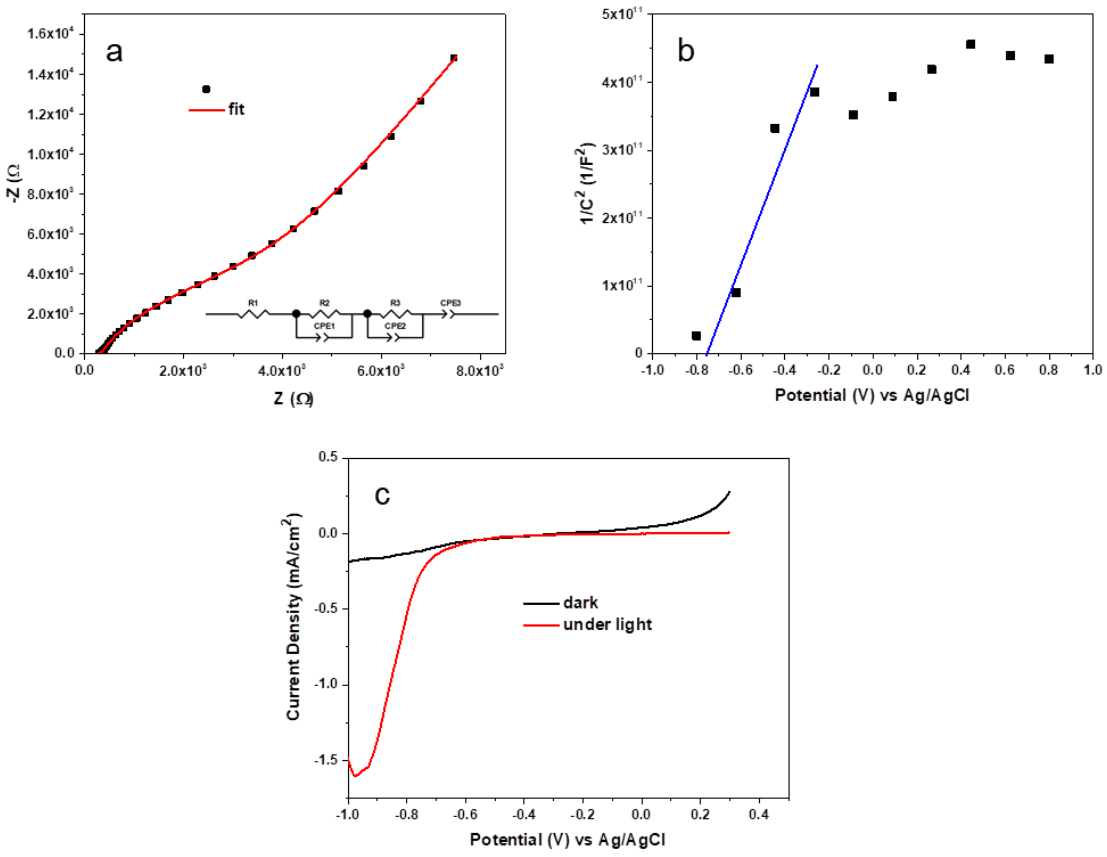

Fig 3.67: a) Nyquist plot and relative equivalent circuit, b) MS graph and c) LSV recorded in dark and under illumination of CPB-FE/C electrode.

Table 3. 15: Resistance value of the interfaces between the CPB-FE and C layers and between the electrolyte and the working electrode (CPB-FE/C).

Sample	R1 (Ω)	R2 (Ω)	R3 (Ω)
CPB-FE/C	276	63	2619

Fig 3.67b reported the MS analysis which shows the n-type nature of the semiconductor and the flat band potential of the CPB-FE/C electrode resulting of -0.734 V vs Ag/AgCl. The value of flat band is converted in V vs NHE in order to obtain a number comparable with the ones obtained for the CPB-oleate and $CsPbBr_3$-MW both coating with graphite. In fact, the flat band potential, close to the conduction band, result to be -0.13 V vs NHE. From the energy diagram it is possible to see the less negative value of the conduction band in comparison with the ones of CPB-oleate, indicating the difficulties of the CPB-FE/C to carry out the CO_2 reduction reaction. On the other hand, in this case the energy diagram was found to be similar to the one obtained with the $CsPbBr_3$-MW/C.

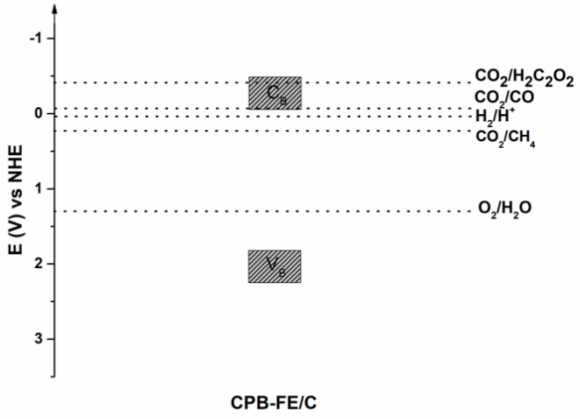

Fig 3.68: Energy diagram of the CPB-FE/C electrode.

CPB-FE/C films were not considered for the PEC tests yet. In addition, further analyses would be carried out to enhance the adhesion of the film on the substrate.

3.5. Photoelectrochemical tests

With a clear picture of the electrochemical properties, the systems were tested for the photoelectrochemical activity on the CO_2 reduction. The products of reaction were determined by high performance liquid chromatography (HPLC). Before testing the $CsPbBr_3$ systems, some injections were made to standardize the methods needs to identify organic acid, aldehydes and ketones. The columns were chosen to detect these three types of molecules because they are the more probable liquid products achievable through CO_2 reduction. The calibration was obtained using two different chromatographic columns: Supelcogel C-610H 30CMx7.8MM and Supelcosil LC-18 5um 25cmx4.6mm, Sigma Aldrich, Germany. For organic acids, a solution of phosphoric acid 0.1 % was considered as mobile phase with a flux rate of 0.5 mL min^{-1} and 30 minutes the time of analysis. The injected volume of the sample was set by the loop i.e. as 20 µL. A mixture of two solutions of formic acid and acetic acid with known concentration (10, 25 and 50 ppm) were used as calibration media. Acetic acid and formic acid were well separated; formic acid had retention time of 19 min while acetic acid of 21 min. The calibrations curve for each organic acid was obtained extrapolating the area's value of the peaks at the relative concentration.

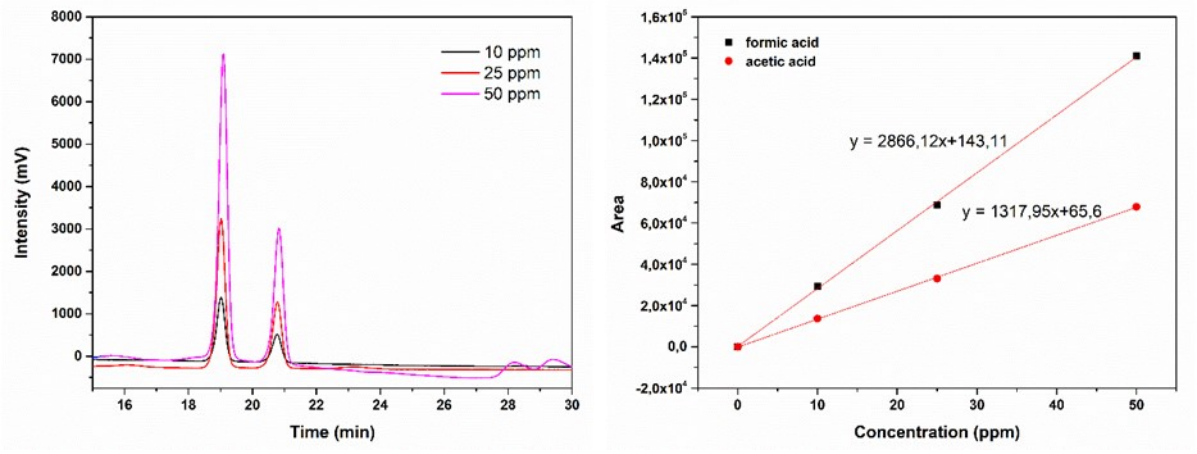

Fig 3.69: Chromatogram and calibration curves of the organic acid standard.

For the carbonyl compounds, it was necessary to derivatized with 2,4-dinitrophenylhydrizine (DNPH) the sample before injection. The process was necessary to make the ketones and aldehydes visible to the HPLC detector (UV-Vis SPD-20A). The

derivatisation consists in a simple reaction (Fig 3.70) where the carbonyl molecules react with DNPH obtaining a derivate molecule, that can be detected by the instrument.

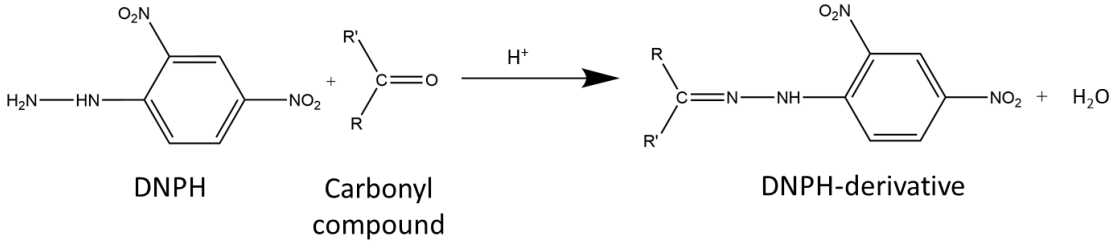

Fig 3.70: Scheme of the derivatisation reaction.

The method for the carbonyl compounds was optimized injecting a mixture of known standards (formaldehyde, acetaldehyde and acetone) and using 100% acetonitrile as mobile phase with a flow of 1.5 mL min^{-1}. The results of Fig 71a show the three peaks relatives at the carbonyl species with retention time of 3.95 min for formaldehyde, 4.06 min for acetaldehyde and 4.20 min for acetone. To better separate the peaks, the pure acetonitrile mobile phase was replaced with a mixture (80:20) of acetonitrile and water. With this modification the 3 species were well separated with retention times of 5.28 min for formaldehyde, 6.24 min for acetaldehyde and 7.68 min for acetone (Fig 3.71b).

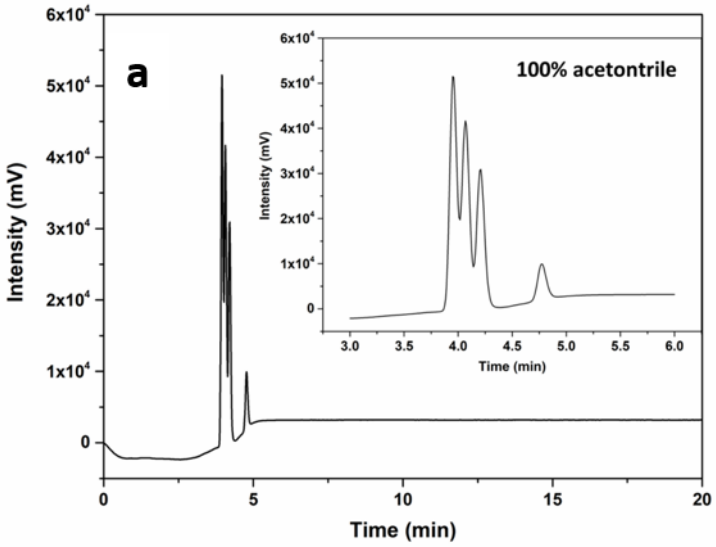

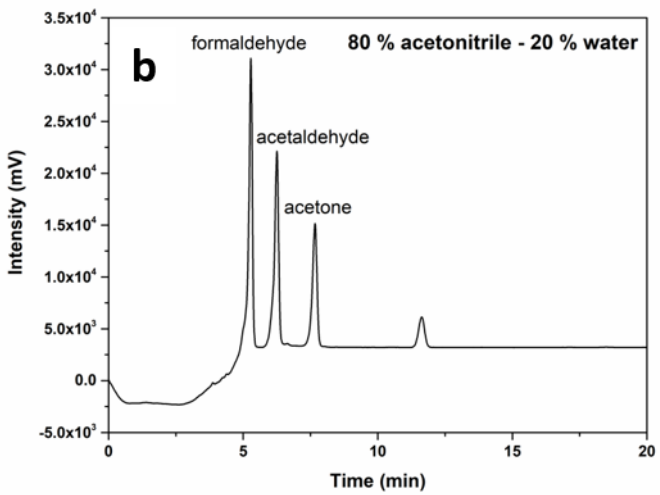

Fig 3.71: Chromatograms of the carbonyl compounds standards using as a) 100% acetonitrile and b) 80:20 acetonitrile:H_2O as mobile phases.

The new mobile phase was used to build the calibration curve, using a flux of 1.5 mL min^{-1} and a time analysis of 15 minutes and three solutions containing formaldehyde, acetaldehyde and acetone at 0.0825 ppm, 0.165 ppm and 0.33 ppm (Fig 3.72).

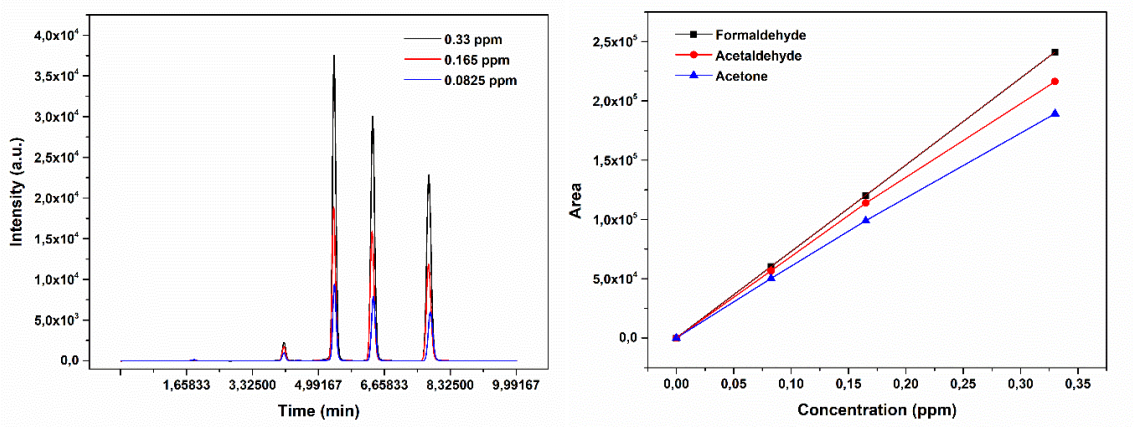

Fig 3.72: Chromatograms of the formaldehyde, acetaldehyde and acetone standard and relative calibration curves.

The methods developed with the calibration curves were used to analyse the products obtained by photoreducing CO_2 with $CsPbBr_3$. $CsPbBr_3$/C and $CsPbBr_3$/Pt were used as working electrodes in a PEC cell, that was used in chronoamperometry tests at two potentials (-0.8 V and -0.5 V) for 3 hours. PEC cell used is composed by two compartments, one anodic and one cathodic; $CsPbBr_3$ as photoelectrode for CO_2 reduction was used as working electrode in the cathodic part where also the reference electrode (Ag/AgCl) was positioned. The counter electrode (Pt foil) was instead insert in the anodic compartment. The cathodic compartment was filled with $KHCO_3$ 0.1 M

electrolyte solution saturated by gaseous CO_2 while for the anodic part with H_2SO_4 0.1 M used as electrolyte. The two parts are divided by a Nafion membrane which avoid the mixing of the two electrolytes but at the same time allows the protons migration from the cathode to the anode sides to close the circuit. The working electrode was irradiated for 3 hours using 1000 W m^{-2} irradiance of the solar simulator. At the end of the reaction, the liquid present in the cathodic compartment of the cell had more or less a volume of 5 mL. 3 mL of the total were put in a becker adding citrate buffer and a solution of DNPH in phosphoric acid for 1 hour, for the derivatisation of the potential ketones or aldehydes presents in the solutions. On the other hand, the remaining 2 mL were used for the injection in the column for the detection of possible organic acids. For both the working electrodes and the potential applied, the chromatograms of the carbonyl compounds, did not reveal the presence of any ketones or aldehyde, while in the chromatograms of the organic acids two peaks were identified at 8.17 min and 9.85 min attributed to oxalic acid. As the previous methods were developed just for formic and acetic acid, three new solutions of oxalic acid (2.5, 5 and 10 ppm) were injected to obtain a calibration curve for this analyte (Fig 3.73).

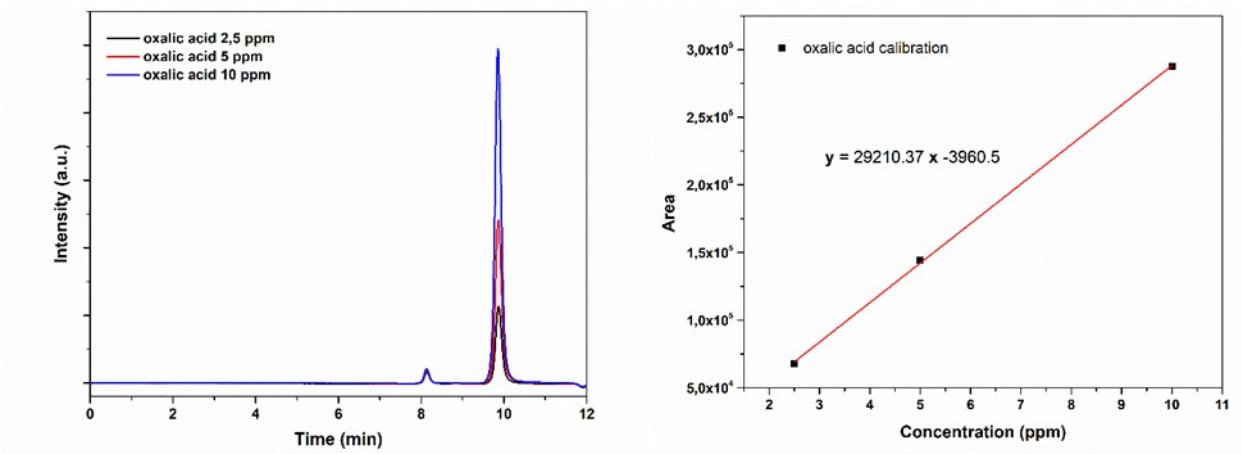

Fig 3.73: Oxalic acid chromatograms and its calibration curve.

The chromatograms of the products are reported in Fig 3.74. The chromatograms related to the $CsPbBr_3$/Pt, were perfectly coincident with the ones of the oxalic acid standards, while for $CsPbBr_3$/C the second peak was shifted at 11.4 min.

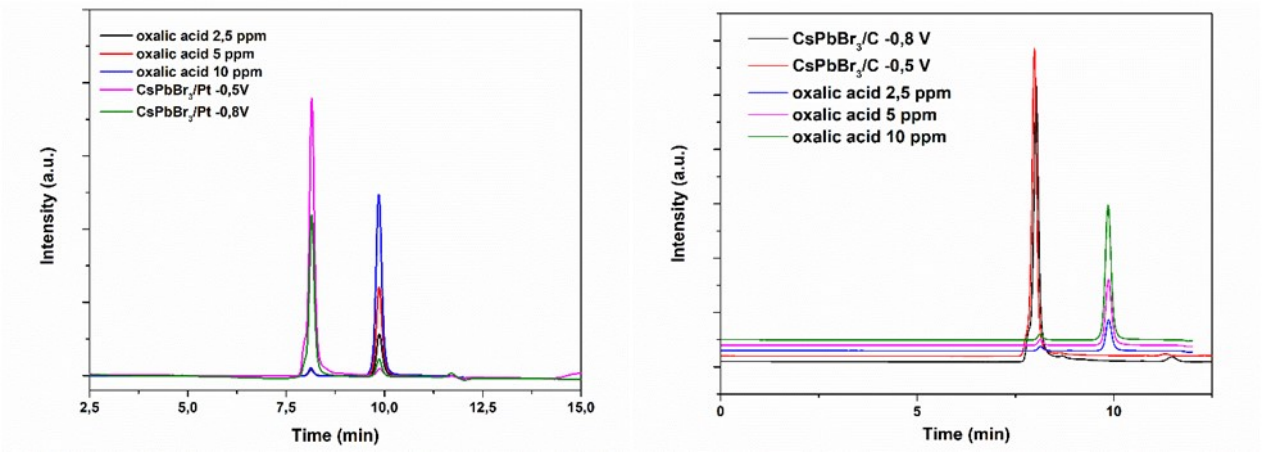

Fig 3.74: Chromatograms of oxalic acid standard and of the reaction products obtaining from the PEC reactions.

The value of the area of the oxalic acid peaks were used with the equation of the calibration curve to obtain the concentration of oxalic acid produced during the reaction. In Table 3.16 are reported the concentration and the faradic efficiencies production of oxalic acid calculated through the equation:

$$FE(\%) = \frac{n_i * C_i * F}{Q} * 100$$

where n_i corresponds to the electrons exchange during the CO_2 reduction, C_i is the concentration (mmol) of the molecules produced, F is the Faradic constant and Q is the electric charge expressed in Coulomb (C). With equal amount of mmol of oxalic acid produced there was more charge (Q) generated with $CsPbBr_3$/Pt than with $CsPbBr_3$/C, giving an higher faradic efficiency for the oxalic acid production for the latter. The performance of $CsPbBr_3$/Pt are thought to be affected by hydrogen production reaction for which Pt is a well-known catalyst. These results were confirmed by the GC analyses on the gaseous products.

Table 3.16: Concentration and faradic efficiency (FE%) of oxalic acid formed from the CO_2 reduction.

sample	mmoli Oxalic Acid	FE (%)
$CsPbBr_3$/C (-0.8 V)	3.44E-05	44
$CsPbBr_3$/C (-0.5 V)	1.88E-05	20
$CsPbBr_3$/Pt (-0.8 V)	5.99E-05	6
$CsPbBr_3$/Pt (-0.5 V)	2.66E-05	5

Although the only CO_2 conversion product is oxalic acid, from the GC chromatograms, is possible observe a significant decrease of the CO_2 concentration during the conversion time. In Table 3.17 are reported the amount of CO_2 at the beginning and at the end of each experiment, the amount of carbon dioxide for all the experiment significant decrease during the three hours indicating an effective CO_2 conversion in favour of the product formation. In addiction for the $CsPbBr_3$ sample tested at V = -0.8 V, the formation of H_2 is observed, even if in very little quantity (n = 0.046 μmol).

Table 3.17: Starting and final CO_2 amount during the conversion reactions.

Sample	Potential applied (V vs SCE)	Starting CO_2 (μmol)	Final CO_2 (μmol)	CO_2 consumed (μmol)
$CsPbBr_3$/C	-0.8	33.22	4.80	28.42
$CsPbBr_3$/C	-0.5	34.11	1.44	32.67
$CsPbBr_3$/Pt	-0.8	31.45	0.68	30.77
$CsPbBr_3$/Pt	-0.5	41.42	2.97	38.45

The conversion of the CO_2 into the oxalic acid $H_2C_2O_4$ happens through the reaction:

$$2\ CO_2 + 2e^- + 2H^+ \rightarrow H_2C_2O_4$$

If the conversion is complete, the reacted CO_2 should be twice the oxalic acid produced. From Table 3.16 and 3.17 is clearly seen that all the CO_2 consumed was not converted into $H_2C_2O_4$. In fact, also hydrogen is produced in the electrode with Pt, and probably part of CO_2 was lost during the 3 hours reaction.

The same procedure was repeated on the electrodes of $CsPbBr_3$ synthetized via microwave, deposited by spin coating and covered by graphite. The results of the test are reported in Table 3.18.

Table 3.18: Concentration and faradic efficiency (FE%) of oxalic acid formed from the CO_2 reduction.

sample	mmoli Oxalic Acid	FE (%)
$CsPbBr_3$/C-MW (-0.8 V)	2.07E-04	0.76
$CsPbBr_3$/C-MW (-0.5 V)	1.17E-05	2.7

The faradic efficiencies confirm the low performance of the $CsPbBr_3$/C-MW electrode. The concentration of the oxalic acid is higher than the moles produced with CPB-oleate samples, but the electric charge produced during the reaction was higher. Being this at the denominator of the faradic efficiency equation, the results reveal that the efficiency was lower for the $CsPbBr_3$/C-MW than the CPB/C-oleate.

In conclusion both the sets of samples can be employed as photoelectrode for the CO_2 reduction in a photoelectrochemical cell and for the oxalic acid production even if with significant difference in faradic efficiency. Further studies about the microwave assisted synthesis and its relative electrode will be carried out in order to achieve higher faradic efficiency and to understand the reason of the differences between the two types of synthesis in the building of the electrode.

3.6. References

67. Liu, W. *et al.* General Strategy for Rapid Production of Low-Dimensional All-Inorganic CsPbBr3 Perovskite Nanocrystals with Controlled Dimensionalities and Sizes. *Inorg. Chem.* **57**, 1598–1603 (2018).

93. Huang, H. *et al.* In situ growth of all-inorganic perovskite nanocrystals on black phosphorus nanosheets. *Chem. Commun.* **54**, 2365–2368 (2018).

96. Gao, G. *et al.* Novel inorganic perovskite quantum dots for photocatalysis. *Nanoscale* **9**, 12032–12038 (2017).

97. Leijtens, T. *et al.* Stability of metal halide perovskite solar cells. *Adv. Energy Mater.* **5**, 1–23 (2015).

101. Zhang, M. *et al.* Growth and characterization of all-inorganic lead halide perovskite semiconductor CsPbBr3 single crystals. *CrystEngComm* **19**, 6797–6803 (2017).

102. Su, X., Zhang, J. & Bai, G. Facile synthesis and characterization of $$\hbox {CsPbBr}_{3}$$ CsPbBr 3 and $$\hbox {CsPb}_{2}\hbox {Br}_{5}$$ CsPb 2 Br 5 powders. *Bull. Mater. Sci.* **41**, 5–10 (2018).

103. Chen, T., Zheng, Y., Lin, J. M. & Chen, G. Study on the Photocatalytic Degradation of Methyl Orange in Water Using Ag/ZnO as Catalyst by Liquid Chromatography Electrospray Ionization Ion-Trap Mass Spectrometry. *J. Am. Soc. Mass Spectrom.* **19**, 997–1003 (2008).

104. Lu, L., Shan, R., Shi, Y., Wang, S. & Yuan, H. A novel TiO2/biochar composite catalysts for photocatalytic degradation of methyl orange. *Chemosphere* **222**, 391–398 (2019).

105. Sha, Y. *et al.* Rapid degradation of azo dye methyl orange using hollow cobalt nanoparticles. *Chemosphere* **144**, 1530–1535 (2016).

106. Jana, A., Mittal, M., Singla, A. & Sapra, S. Solvent-free, mechanochemical syntheses of bulk trihalide perovskites and their nanoparticles. *Chem. Commun.* **53**, 3046–3049 (2017).

107. Du, X. *et al.* High-quality CsPbBr3 perovskite nanocrystals for quantum dot light-emitting diodes. *RSC Adv.* **7**, 10391–10396 (2017).

108. Akkerman, Q. A. *et al.* Nearly Monodisperse Insulator Cs4PbX6 (X = Cl, Br, I) Nanocrystals, Their Mixed Halide Compositions, and Their Transformation into CsPbX3 Nanocrystals. *Nano Lett.* **17**, 1924–1930 (2017).
109. Singh, M., Goyal, M. & Devlal, K. Size and shape effects on the band gap of semiconductor compound nanomaterials. *J. Taibah Univ. Sci.* **12**, 470–475 (2018).
110. Cho, J. & Banerjee, S. Ligand-Directed Stabilization of Ternary Phases: Synthetic Control of Structural Dimensionality in Solution-Grown Cesium Lead Bromide Nanocrystals. *Chem. Mater.* **30**, 6144–6155 (2018).
111. Liu, Z. *et al.* Ligand Mediated Transformation of Cesium Lead Bromide Perovskite Nanocrystals to Lead Depleted Cs4PbBr6 Nanocrystals. *J. Am. Chem. Soc.* **139**, 5309–5312 (2017).
112. De Roo, J. *et al.* Highly Dynamic Ligand Binding and Light Absorption Coefficient of Cesium Lead Bromide Perovskite Nanocrystals. *ACS Nano* **10**, 2071–2081 (2016).
113. Rodríguez, A. M. *et al.* Influence of Polarity and Activation Energy in Microwave-Assisted Organic Synthesis (MAOS). *ChemistryOpen* **4**, 308–317 (2015).
114. Leadbeater, N. E. & Torenius, H. M. A study of the ionic liquid mediated microwave heating of organic solvents. *J. Org. Chem.* **67**, 3145–3148 (2002).
115. Li, Y., Huang, H., Xiong, Y., Kershaw, S. V. & Rogach, A. L. Revealing the Formation Mechanism of CsPbBr3 Perovskite Nanocrystals Produced via a Slowed-Down Microwave-Assisted Synthesis. *Angew. Chemie - Int. Ed.* **57**, 5833–5837 (2018).
116. Cai, Y. *et al.* Improved stability of CsPbBr3 perovskite quantum dots achieved by suppressing interligand proton transfer and applying a polystyrene coating. *Nanoscale* **10**, 21441–21450 (2018).
117. Hoffman, J. B., Zaiats, G., Wappes, I. & Kamat, P. V. CsPbBr3 Solar Cells: Controlled Film Growth through Layer-by-Layer Quantum Dot Deposition. *Chem. Mater.* **29**, 9767–9774 (2017).
118. Tyona, M. D. A theoritical study on spin coating technique. *Adv. Mater. Res.* **2**, 195–208 (2013).
119. Nasi, L. *et al.* All-Inorganic CsPbBr3 Perovskite Films Prepared by Single Source Thermal Ablation. *Front. Chem.* **8**, 1–10 (2020).
120. Zhao, J. *et al.* Investigation of the hydrolysis of perovskite organometallic halide CH3NH3PbI3 in humidity environment. *Sci. Rep.* **6**, 1–6 (2016).

121. Qiao, B. *et al.* Water-resistant, monodispersed and stably luminescent CsPbBr3/CsPb2Br5 core-shell-like structure lead halide perovskite nanocrystals. *Nanotechnology* **28**, 445602 (2017).

122. Wu, L. *et al.* From Nonluminescent Cs4PbX6 (X = Cl, Br, I) Nanocrystals to Highly Luminescent CsPbX3 Nanocrystals: Water-Triggered Transformation through a CsX-Stripping Mechanism. *Nano Lett.* **17**, 5799–5804 (2017).

123. Cha, J. H. *et al.* Photoresponse of CsPbBr3 and Cs4PbBr6 Perovskite Single Crystals. *J. Phys. Chem. Lett.* **8**, 565–570 (2017).

124. Muduli, S. *et al.* Photoluminescence Quenching in Self-Assembled CsPbBr3 Quantum Dots on Few-Layer Black Phosphorus Sheets. *Angew. Chemie - Int. Ed.* **57**, 7682–7686 (2018).

125. Chen, K. *et al.* In situ preparation of a CsPbBr3/black phosphorus heterostructure with an optimized interface and photodetector application. *Nanoscale* **11**, 16852–16859 (2019).

126. Li, W., Han, C., Liu, W., Zhang, M. & Tao, K. Expanded graphite applied in the catalytic process as a catalyst support. *Catal. Today* **125**, 278–281 (2007).

127. McKone, J. R. *et al.* Evaluation of Pt, Ni, and Ni-Mo electrocatalysts for hydrogen evolution on crystalline Si electrodes. *Energy Environ. Sci.* **4**, 3573–3583 (2011).

128. Li, Y. *et al.* Under-Water Superaerophobic Pine-Shaped Pt Nanoarray Electrode for Ultrahigh-Performance Hydrogen Evolution. *Adv. Funct. Mater.* **25**, 1737–1744 (2015).

129. Cardenas-Morcoso, D. *et al.* Photocatalytic and Photoelectrochemical Degradation of Organic Compounds with All-Inorganic Metal Halide Perovskite Quantum Dots. *J. Phys. Chem. Lett.* **10**, 630–636 (2019).

130. Huang, Y., Fang, M., Zou, G., Zhang, B. & Wang, H. Monochromatic and electrochemically switchable electrochemiluminescence of perovskite CsPbBr3 nanocrystals. *Nanoscale* **8**, 18734–18739 (2016).

131. Daubinger, P., Kieninger, J., Unmüssig, T. & Urban, G. A. Electrochemical characteristics of nanostructured platinum electrodes-A cyclic voltammetry study. *Phys. Chem. Chem. Phys.* **16**, 8392–8399 (2014).

132. Sacco, A. Electrochemical impedance spectroscopy: Fundamentals and application in dye-sensitized solar cells. *Renew. Sustain. Energy Rev.* **79**, 814–829 (2017).

133. Hagfeldt, A. *et al. Dye-Sensitized Photoelectrochemical Cells*. *Solar Cells* (Elsevier Ltd, 2013). doi:10.1016/B978-0-12-386964-7.00013-5

134. Shao, Q., Lin, H. & Shao, M. Determining Locations of Conduction Bands and Valence Bands of Semiconductor Nanoparticles Based on Their Band Gaps. *ACS Omega* **5**, 10297–10300 (2020).

Chapter 4

Conclusions and future prospective

Renewable solar energy was successfully exploited in this PhD work to reduce CO_2 in a photoelectrochemical cell using for the first time $CsPbBr_3$ as photoelectrochemical material. The perovskite has been successfully synthetized through different methods, from the simple co-precipitation method, passing from the oleate-synthesis and ending with the more complex microwave assisted one. The co-precipitation synthesis gave an orange brilliant powder, while with oleate and microwave synthesis, the $CsPbBr_3$ was obtained in form of submicronic particles suspended in a non-polar solvent (hexane or toluene). The use of microwave assisted heating, allows to decrease the reaction time needed to produce pure monoclinic $CsPbBr_3$.

With all the synthesis studied, the perovskite was obtained in single monoclinic phase and shows bandgap suitable to absorb light in the visible part of the electromagnetic spectra. The photocatalytic activity in water was studied only for the material synthetized by oleate-synthesis; the organic chains remained absorbed on the particles after synthesis (oleic acid and oleylamine) protected the $CsPbBr_3$ from the water-induced dissolution. For the other systems the photocatalytic tests were carried out in organic solvent (ethyl acetate), confirming the significant photocatalytic activity of the material in this medium. The materials were then deposited on an FTO (Fluorine Tin Oxide) substrate to produce the photoelectrode. Three different techniques of increasing complexity were considered and optimized for this purpose: drop by drop, spin coating deposition and ink-jet printing. In the drop by drop technique, just few parameters can be adjusted, while spin coating gives different way to improve the film homogeneity (speed of rotation, number and the duration of the deposition cycles or the backing temperature) while ink-jet printing is the most flexible and reproducible technique that can be also easily industrialized. With the drop by drop deposition, a non-homogeneous film with coffee stain defects was obtained. The film quality was enhanced using the spin coating method, through a careful choice of the solvent deposition (hexane and toluene). The better properties were obtained with toluene suspension as a consequence of its higher boiling point, higher density and viscosity. The electrochemical characterization of $CsPbBr_3$ and the photoelectrochemical cell test were performed on the film deposited via spin coating. Different set of parameters and ink compositions were considered for the deposition with inkjet. Even if some good results

have been obtained, this deposition still requires some work to eliminate the defects clearly visible on the surface.

The film obtained by spin coating was coated to increase its stability in water environment with two different layers, one of graphite (C) and one of platinum (Pt). The two materials were chosen for their conductivity and well-known catalytic role. Thanks to the coatings the perovskite was effectively stabilized in water as assessed by cyclic voltammetry. Having achieved a good stabilization, the electrochemical characteristics of $CsPbBr_3$ was analyzed in a three-electrode cell by electrochemical impedance spectroscopy (EIS), Mott-Schottky analysis (MS) and linear sweep voltammetry (LSV). The analyses allow to build the energy diagrams of the two systems ($CsPbBr_3$/C and $CsPbBr_3$/Pt) and understand the behavior at the interfaces between the layer composing the film and between the film and the aqueous electrolyte. $CsPbBr_3$/Pt presented lower resistance at the charge transfer and lower charge recombination than the $CsPbBr_3$/C as expected as a consequence of the metallic nature of platinum, more conductive than the carbon-based materials.

The CO_2 reduction in a photoelectrochemical cell gave however oxalic acid as main product with significantly higher faradic efficiency for the $CsPbBr_3$/C sample probably for the competitive Hydrogen Evolution Reaction (HER) catalyzed by Pt.

$CsPbBr_3$ were stabilized also before the deposition, trying two approaches, the passivation of the surface $CsPbBr_3$ particles with organic compounds or the synthesis in situ of hybrids compounds between the $CsPbBr_3$ and 2D materials (black phosphorus, bP and graphene oxide, GO). The first approach was not successful: the material was in fact protected but the long organic chains imped the movement of the charges blocking its catalytic activity. On the other hand, hybrid compounds were successfully synthetized with the same synthesis route used for the pure perovskite. TEM images clearly showed the submicronic $CsPbBr_3$ particles on the 2D material sheets. The photocatalytic analyses showed an increased activity of the hybrids systems compared to the bare $CsPbBr_3$.

$CsPbBr_3$ was found to be a very promising material for photoelectrochemical reduction of carbon dioxide. More work will be devoted to the microwave assisted synthesis to study the influence of different morphologies on the reduction reaction. The different morphologies could be reached changing the capping ligands (oleic acid and oleylamine) or changing their ratio to tune the facet of the powder to be used in the reaction.

The first studies on the hybrids with the 2D material bP and GO are very promising either in term of stabilization of the system and improved properties. Future work will be devoted to assessing all the range of electrochemical properties of the systems and to deposit them in order to study their photoelectrochemical ability to reduce carbon dioxide.

Finally, the ink-jet printing of $CsPbBr_3$ will be further investigated, trying to reach a well-defined deposition and trying to avoid the main defects on the $CsPbBr_3$ surface. The microwave synthesis of colloidal suspensions of perovskite will be considered as basis for the ink-jet ink.

Acknowledgments

I would like to thank Dr.ssa Anna Tampieri for having given me the opportunity to carry out the activity at ISTEC-CNR, I would also like to thank Prof. Enrico Dal Canale for having let me attend the PhD program.

The greatest gratitude goes to my research group, thank to Dr.ssa Alessandra Sanson who give me always her support especially in the last period, and to have helping me to overcome my difficulties. Thanks to the other girls of the group, Angela and Elisa for their help in and outside the laboratory. Thanks to Nicola, Alex, Simo and Andrea for share with me the open space, the jokes and for their patience when I freaked out with my PC. A great thank also to Paola, for all the boogie dances and for her direct sincerity. Thanks also to all the ISTEC-CNR staff, in particular to Ciccio, Jan, Andreana, Monica and Silvia, they are always nice with me.

Thanks to Dr.ssa Maria Caporali, Dr.ssa Manuela Melucci, Dr. Gregorio Bottaro, Dr. Marzio Rancan and Dr. Roberto Mosca for their collaboration and for their contribute in my PhD work.

I would like to thank the young part of ISTEC, in particular Massi, Chiara, Fra S, Lara, Lore, Franco, Simo (C.), Ema (even if you leave us to escape in Milan) and all the guys with whom I have share all the breaks, the lunches, the cleaning after lunches, the “aperitivi” after work, the sushi dinners and so on… I hope we will continue having fun together with or without the mask.

To Ila for all the chitchat and the laughter, to Fra for all the dinners before the volley match and for our not so feminine ways, to Samu, even if you’re far from us, you remain one of the main person known here! Thank you for having been my run mate, and my friend. To Betta who give me her friendship from the beginning, inviting me always also with her friends and for all the nights spent to make the Christmas decorations and having a lot of fun. To Marghe, my partner in crime! A wonderful surprise and person,

thank you for our crazy things, starting from the seaside escapes and ending with our long chats.

Thanks to my lifelong friends Ila, Ila and Giudi, even if now our roads are very different, we grew up together starting from that classroom and we continue to do it. We are supporting each other in our decisions of work, study, love and friendship, always.

Thanks to my Gavello's friends Davide, Mattia, Alba, Chiara, Enrico, Bonfi, Chris, Giulia, Valtu, Giulio O., Aury and the little Bianca and Beatrice. For our barbeques, and our wonderful carefree days.

The further words would be the last but the more important for me, to my family. My mum and dad (mammina e papino) for their support, for always believe in me, for listen to me, also when I'm not so nice with them, for help me in all life decisions. I love you so much! To my sisters Francesca and Daniela, they are my guide, my example and I am grateful to have them always by my side. Thanks to my crazy nephews Massimiliano and Samuele, whom give me the joy every time I see them.

To Giulio, you always been with me, you always support me, before as a friend, then as a boyfriend and now as my life partner and in future...who knows! I have no words to say to you..only that I love you!